FILM COOLING IN FUEL RICH ENVIRONMENTS

THESIS

Jacob J. Robertson, Second Lieutenant, USAF

AFIT-ENY-13-M-27

DEPARTMENT OF THE AIR FORCE
AIR UNIVERSITY

AIR FORCE INSTITUTE OF TECHNOLOGY

Wright-Patterson Air Force Base, Ohio

The views expressed in this thesis are those of the author and do not reflect the official policy or position of the United States Air Force, the Department of Defense, or the United States Government.

AFIT-ENY-13-M-27

FILM COOLING IN FUEL RICH ENVIRONMENTS

THESIS

Presented to the Faculty

Department of Aeronautics and Astronautics

Graduate School of Engineering and Management

Air Force Institute of Technology

Air University

Air Education and Training Command

in Partial Fulfillment of the Requirements for the

Degree of Master of Science in Aeronautical Engineering

Jacob J. Robertson, B.S.

Second Lieutenant, USAF

March 2013

AFIT-ENY-13-M-27

FILM COOLING IN FUEL RICH ENVIRONMENTS

Jacob J. Robertson, B.S.
Second Lieutenant, USAF

Approved:

Dr. Marc D. Polanka, (Chairman)	Date
Dr. Jeremy Agte, (Member)	Date
Dr. James Rutledge, (Member)	Date

AFIT-ENY-13-M-27

Abstract

The ultra compact combustor is a high performance gas turbine design concept that portends reduced weight for future weapons platforms. A natural outcome of the design is the continual presence of fuel-rich air in the turbine component of the engine. Because modern cooling schemes for hot section turbine blades involve injecting cool, oxygen-rich air adjacent to the surface, the potential arises for reaction with the unconsumed radicals in the mainstream flow and augmented heat transfer to the blade. This outcome is contrary to the purpose of film cooling, and can lead to early life-cycle turbine failure. This study examined the effects of multiple cooling hole geometries on downstream heat transfer. It demonstrated schemes that allow reactions to take place at a standoff distance from the wall being cooled and provide effective downstream cooling. Additionally, the research characterized the time scales involved in the reactions through temperature measurements and imaging.

Acknowledgments

”Whatever you do, work at it with all your heart, as working for the Lord, not for men” -Colossians 3:23 My thanks go to God first, for the strength and perserverence to complete this thesis. Thanks to my loving wife, who always supported me through the long days and nights of work. Thank you to my advisor, Dr. Polanka, who was always there with feedback and advice. Thank you Nate, for sitting in the lab with me for all those months, providing stimulating conversation and lots of insight into school and life in general. Thanks to Major Rutledge, whose patience and intellect were kindly lent to me time and again. Finally, thanks to Mike, for having a fix to every problem we could come up with! My time working on this research has been tough, but I am very thankful to have had the opportunity to know all of you.

Jacob J. Robertson

Table of Contents

Page

Page

List of Figures

List of Tables

List of Symbols

Symbol	Definition
Da	Damköhler number $\frac{\tau_{flow}}{\tau_{chem}}$
D	injection hole diameter (m)
M	blowing ratio, equation 2.7
P	pressure (Pa)
Re	Reynolds number
R	universal gas constant (8315 $\frac{J}{kmol-K}$)
T	temperature (K)
U	velocity $\frac{m}{s}$
h	convective heat transfer coefficient $\frac{W}{m^2K}$
k	conductive heat transfer coefficient $\frac{W}{mK}$
l	length (m)
m	mass ratio
q''	heat flux $\frac{W}{m^2}$
x	axial/streamwise coordinate (m)
y	depth into block (m)
z	spanwise coordinate (m), see section 3.8
α	absorptivity
ϵ	radiative emissivity
η	adiabatic effectiveness (see equation 2.6)
ρ	density ($\frac{kg}{m^3}$)
σ	heat flux augmentation or Stefann-Boltzmann constant in radiation context
ϕ	equivalence ratio, equation 2.9

Symbol	Definition
Subscripts	
FA	Fuel-to-Air
H	hydraulic (hydraulic diameter)
aw	adiabatic wall, indicating a condition of no heat transfer
c	coolant
eff	effective
f	film
g	gas
$stoich$	indicates a stoichiometric ratio of reactants
w	wall
∞	freestream

List of Acronyms

Acronym	Definition
AFRL	Air Force Research Laboratory
CEA	Chemical Equilibrium with Applications
CFD	Computational Fluid Dynamics
IR	Infrared
PLIF	Planar Laser Induced Fluorescence
UCC	Ultra Compact Combustor
WSR	Well Stirred Reactor

FILM COOLING IN FUEL RICH ENVIRONMENTS

I. Introduction

1.1 Thesis Objective

This thesis focused on several objectives, all of which centered on improving film cooling in fuel-rich environments. The primary objective of the research was to characterize the downstream effectiveness and heat transfer of various film cooling hole arrangements devised to protect the wall from additional heat release induced by secondary combustion. Another objective was to attempt to consume fuel and radicals at a standoff distance from the wall being cooled. Ultimately, the research aimed to create a film cooling scheme for use in a high fuel air environment in a turbine. Cooling schemes focused on the effects of closely spaced rows of injection holes, the effects of dilution schemes prior to attached cooling layers, and the integration of combustor liner techniques into turbine film cooling schemes. It was hypothesized that these arrangements would provide separation of the fuel-rich zone from the oxygen-rich zone and promote reactions away from the wall. This would allow film cooling schemes to remain effective in fuel-rich environments.

1.2 Research Hardware

The experiment utilized a new experimental rig, constructed in conjunction with the Air Force Research Laboratory (AFRL). The rig was supplied with hot, reacted, equivalence ratio controlled air-fuel mix by a well-stirred reactor (WSR). This flow passed down a 863 mm^2 rectangular section internal flow tube. Modular plenum/cooling hole and instrumentation blocks were inserted flush to the wall of this tube. The instrumentation block was wired with sixteen pairs of offset depth thermocouples,

allowing the measurement of temperatures and heat transfer. The overall design allowed for implementation of interchangeable cooling arrangements and evaluation of their downstream cooling effectiveness. Fused silica side windows and optical ports leave future researchers the option of performing optical flow diagnostics such as planar laser induced fluoresence (PLIF). Additionally, a sliding sapphire window was integrated into the wall opposite the cooling and instrumentation inserts to allow for infrared imaging of the device.

The design of the test rig took many lessons into account. Evans, DeLallo, and Bohan had all performed previous research with a similar device. Bohan found through PLIF measurements that most of the reactions in reactive film cooling were taking place less than 25 diameters downstream of injection [5]. Because the previous rig had only measured temperatures and heat flux at 25 and 95 diameters downstream, many crucial flow physics were being missed. The current rig measures heat flux at 7, 15, 20, and 27 diameters downstream. This design allows better characterization of downstream effectiveness, meeting a primary objective of the research. DeLallo attempted to test the effects of upstream radical consumption ("Dilution" cooling schemes) in his research, but was limited by the size and separation of his cooling plenum inserts. He hypothesized that closer-spaced rows of holes might be able to achieve a dilution effect [8]. As such, the current rig implements a much larger plenum than previously seen in the literature. This allows for testing of more varied cooling schemes, meeting another crucial objective of the research. DeLallo also found a need to be able to control the wall temperature for identical flow conditions [7]. As such, the current rig implemented extensive cold-side cooling loops able to accommodate multiple cooling methods, and a wide range of possible wall temperatures. The new design allows the current rig to aid the researcher in developing a deeper understanding of the physics of reactive film cooling, helping to fulfill all research objectives.

1.3 Film Cooling

Film cooling schemes are currently the primary means of preserving turbine blades in gas turbine engines. The current research is focused on updating these schemes for fuel-rich environments. Film cooling in modern engines typically injects relatively cool air adjacent to turbine blades. This provides a buffer layer and reduces heat transfer to the blade from the hot external flow. The coolant flow is typically conveyed to the surface via internal channels in the blade, convecting away additional heat. Combining these methods with thermal barrier coatings allows turbine blades to survive in environments at significantly higher temperatures than the melting points of their structural materials. While viscous losses are introduced to the cycle with this method, film cooling allows gas turbine engines to run higher equivalence ratios in their combustors, increasing thermal efficiency and allowing for greater specific thrust, while maintaining reasonable life cycles for their components. Historical trends for increasing turbine temperatures can be seen in Figure 1.1.

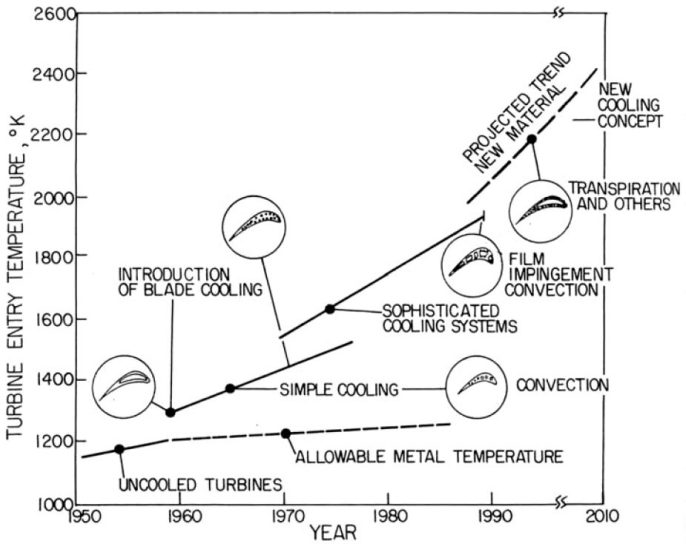

Figure 1.1: Turbine inlet temperature trends [14]

A typical modern turbine blade with holes for film cooling in its surface can be seen in Figure 1.2. Injection holes are arranged in rows and are angled to produce attached flow parallel to the blade surface. In the stagnation region at the front of the blade the holes inject more normally to the flow in an attempt to shield the leading edge from high heat transfer stagnation effects.

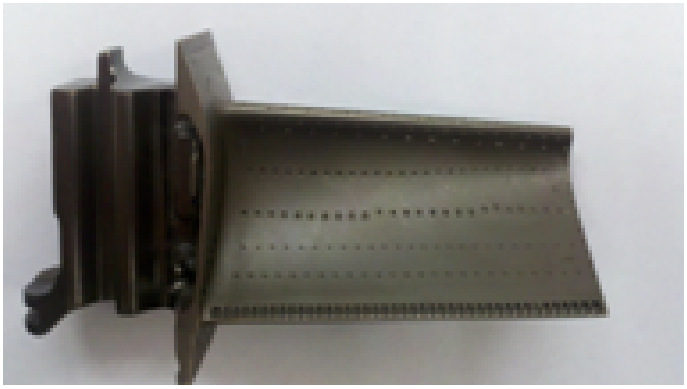

Figure 1.2: Typical Film Cooling Scheme [7]

A natural outcome of modern film cooling is the presence of a thin attached layer of oxygen-rich air. In the presence of a fuel-rich area, rapid diffusion, mixing, and burning can occur immediately adjacent to the wall as a consequence of this design methodology. New strategies are necessary in order to mitigate these effects.

1.4 Combustor Liner Design

The design of future turbine blade cooling schemes for fuel-rich environments has many parallels with current combustor liner design. Both processes maintain the goal of preserving material in reacting environments. While many differences exist, several broad-scope strategies of modern combustor liner design have application to the current problem.

Modern combustor cooling strategies include “cold” side convective cooling, slot injected film cooling, impingement cooling, and transpiration cooling [21][19]. “Cold”

side convection and impingement are already widely used in turbine blades. Transpiration cooling has a close analogy in the "showerhead" stagnation region design of turbine blades. However, greater differences are apparent in the two components' approach to film cooling. Combustor liners focus on injecting high mass flow through slots in order to provide a sufficiently thick layer that reactions occur away from the liner surface. When diffusion has decreased the downstream effectiveness of a slot to unacceptable levels, a new slot injects fresh coolant to renew the supply of cool air.

While high coolant mass flows are undesirable in a turbine due to overall cycle efficiency degradation, the slot approach of combustor liners can be applied on a smaller scale. This approach also suggests the potential efficacy of other methods that form a contiguous, "thick" coolant layer. As such, turbine film cooling in fuel-rich environments could bring about the desired wall protection by utilizing designs of this nature.

1.5 Applications

1.5.1 The Ultra-Compact Combustor.

The Ultra Compact Combustor (UCC) is a design for high performance gas turbine engines that can allow for shorter flow paths and lower weights, as shown in Figure 1.3. This design has the potential to reduce combustor lengths by up to 66% [27]. The design utilizes circumferential burning outside of the core, axial flow. The circumferential flow experiences high centripetal acceleration and load factors, enhancing the burn rate and stabilizing combustion. Heat and fuel is transferred to the core flow as it passes. The UCC burns at an equivalence ratio greater than one, leading to uncombusted products exiting the component. Therefore, a natural outcome of the design is the presence of fuel-rich air in the turbine. Modern gas turbines utilize film cooling schemes to protect the material of the turbine from the hot gases found at the combustor exit. This method involves injecting oxygen-rich air from the compressor out of the turbine blade, forming a protective sheath of relatively cool air. This allows gas turbines to combust at stagnation

temperatures nearly twice the melting point of the modern nickel alloys from which most turbines are constructed. Previous testing of experimental flat plate cooling rigs has shown that this oxygen-rich cooling air can quickly react with the fuel-rich air and increase heat transfer to the turbine blade above its uncooled value [16]. This reaction can lead to turbine failure and is a design issue that must be handled before practical implementation of the UCC can occur. This thesis attempts to provide a step towards solving this problem.

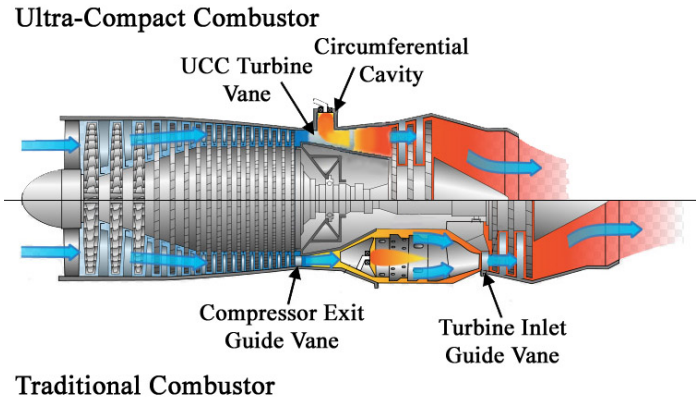

Figure 1.3: Ultra Compact v. Traditional Combustor [8]

1.5.2 Fuel-Rich Streaks in Conventional Combustors.

Conventional combustors rely on a combination of diffusion, swirl, and high-mass flow injection jets to create distinctive combustion zones with high residence time to allow full reaction completion. Occasionally, rogue fuel droplets or pockets of radicals can escape from these zones into the turbine section. These local fuel-rich pockets can react with film cooling in the turbine to increase heat transfer and degrade turbine blades. Accomplishment of the objectives of this research will provide strategies to mitigate these harmful effects.

II. Literature Review

The problem of secondary reactions forming in film coolant flows is a complex one. This chapter presents applications of the current research found in the UCC problem and the fuel-rich streak problem in order to provide a thorough understanding of the expected real-world conditions. The literature review also provides background in film cooling and combustion in order to provide a framework for the physics involved. Finally, the field of reactive film cooling, incorporating all of these disciplines and its own body of research is examined in depth. This thesis can thus build on past efforts and make the next stride towards real world application.

2.1 Applications

The problem of reactive film cooling already has applications in modern combustors. Additionally, future combustors such as the UCC are likely to exacerbate the issue as more performance is demanded of shorter, less massive combustor sections. An overview of these two applications is provided for context of the importance of the current research.

2.1.1 Fuel-Rich Streaks and Traditional Combustors.

Lukachko et. al. showed the potential of modern combustors to introduce unconsumed radicals to the turbine. In addition to the potential of fuel droplets to escape the highly-recirculated primary combustion zone, equilibrium chemistry provides a source of radicals independent of residence time, as shown in Figure 2.1. Modern gas turbine engines applying full power experience very high compression ratios, near-stoichiometric combustion, and extremely high temperatures. As a result, the potential for reaction and augmented heat flux arises whenever cool oxygen-rich air is injected and changes the equilibrium chemistry of the mixture.[16].

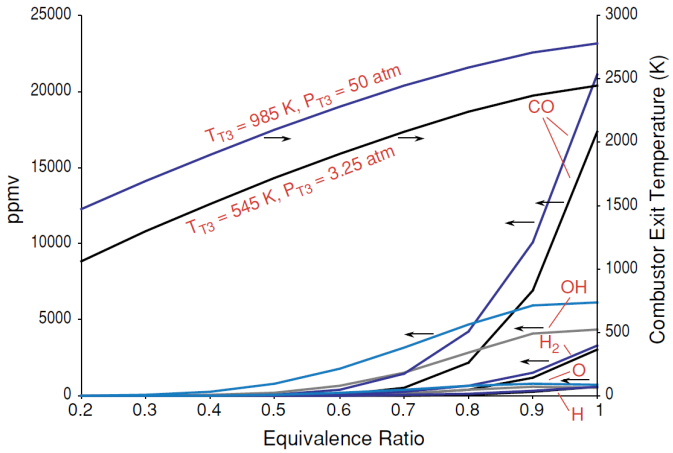

Figure 2.1: Increase in equilibrium radicals with pressure and ϕ rise [16]

2.1.2 The UCC.

The concept of the UCC was originally invented by Sirignano [25]. Experiments by Lewis in 1973 showed that centrifugal loading of a fuel-air mixture could drastically improve the flame speed [15]. Sirignano hypothesized that this effect could be used to drastically reduce combustor size. The basic layout of a typical UCC design is shown in Figure 2.2. It consists of a circumferential cavity wrapped around a traditional annular flow area in a gas turbine. Fuel and air injection occurs circumferentially in the cavity, creating a high-g anchored flame. Fuel products migrate inward radially as they break down and burn, resulting in heat transfer to the core, annular flow.

Expansionary work was done by Zelina et. al. in 2004 [27]. An experimental rig, shown in Figure 2.3, was used to quantify heat release, combustor operability, emissions, and efficiencies. All experiments were performed at one atm. The concept of the UCC was experimentally shown to be promising, although many design challenges lay ahead before practical implementation can occur [27].

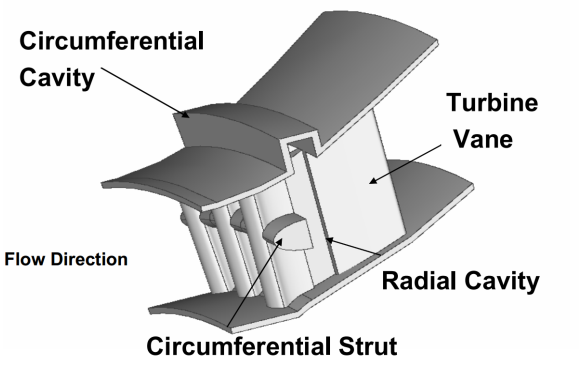

Figure 2.2: Typical UCC Configuration [27]

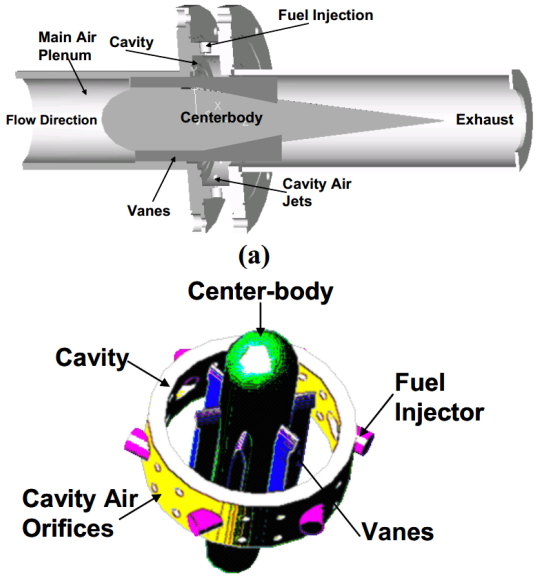

Figure 2.3: Zelina UCC Rig [27]

Many design issues are present with the UCC. Bohan showed the primary issue of relevance to the current research. His research described a UCC design in which the cavity runs at fuel-rich conditions, with ϕ as high as two [5]. Unconsumed radicals are intentionally entrained into the core axial flow where they diffuse toward the inner radius. Fuel-rich conditions are then present on and concentrated towards the outer radius of film-

cooled vanes [5]. This creates a reactive film cooling problem that fulfillment of the objectives of the current research can help to mitigate.

2.2 Traditional Film Cooling

Film cooling reduces the surface temperature and heat flux to a wall exposed to hot gases by injecting a coolant into the flow. The coolant forms a thin protective buffer layer of relatively cool temperature between the surface and the freestream. This lowers the temperature of the wall, T_w, and heat flux to the wall, q", from what it would experience without film cooling.

Deeper understanding of the phenomena associated with film coolng demands some knowledge of the physics of heat transfer. Heat transfer, or flux (used interchangeably in this thesis), is defined as the amount of energy in the form of heat moving through a medium normal to a differential area per unit area. The primary concern of this research is with the convective form of heat transfer, which can be described by Newton's law of cooling, seen in equation 2.1. For a given freestream velocity past a wall, the convective heat transfer coefficient, h, is typically considered to be a constant independent of the freestream and wall temperatures. In non-reactive cooling over small temperature ranges this is a relatively good assumption [3]. For the reactive case h becomes a strong function of freestream and wall temperature, leading to non-linearities that make theoretical analysis difficult.

$$q'' = h(T_\infty - T_w) \tag{2.1}$$

Conductive heat transfer occurs within a quiescent material. For steady, 1-dimensional cases, the convective heat transfer from the freestream to the wall is equal to the conductive heat transfer within the wall. Using Fourier's law of conduction, seen in equation 2.2, temperature measurements made at two locations within the wall can thus be used to quantify heat transfer and wall temperature, so long as the material's coefficient of conduction, k, is known [3] .

$$q'' = -k\frac{dT}{dx} \tag{2.2}$$

Radiative heat transfer occurs via electromagnetic emission as a result of temperature. For an opaque surface, net radiative heat transfer obeys equation 2.3, where ϵ is the emissivity of the surface, σ is the Stefan-Boltzmann constant, T_s is the surface temperature, α is the surface absorptivity, and G is net irradiation of the surface.

$$q''_{net} = \epsilon\sigma T_w^4 - \alpha G \tag{2.3}$$

These equations must be modified to reflect the physical realities of film cooling. The injected coolant forms a layer of cool air that progressively mixes with the freestream as it moves from its injection point. The coolant is initially at temperature T_c, The freestream is at temperature T_∞, and the wall is at temperature T_w. Following injection, the coolant begins mixing with freestream gases and forms a film of temperature T_f, which is intermediate between T_∞ and T_c and varies with distance downstream, x. For cooling configurations, T_f is specifically characterized as a function of x/D, where D is the hole diameter. Understanding of the driving flow temperature adjacent to the wall allows a modification to Newton's Law of Cooling for the case of film cooling as shown in equation 2.4, where h_f is the convective heat transfer coefficient of the film on the surface.

$$q'' = h_f(T_f - T_w) \tag{2.4}$$

For the current experiment, convection was generally assumed to be the only form of heat transfer into the hot side of the instrumentation block described in section 3.8. Radiation was undoubtedly contributing to this number, but no means of effectively measuring the net gas radiation was available. As such, all heat flux was assumed to be part of the effective convection. As such, Equation 2.4 is further modified to the form in

Equation 2.5, where h_{eff} is the effective heat transfer coefficient governing all heat transfer into the block.

$$q'' = h_{eff}(T_f - T_w) \tag{2.5}$$

The effectiveness of a cooling configuration is typically quantified via a non-dimensional term known as "adiabatic effectiveness", or 'η', the determination of which is shown in 2.6. The adiabatic wall temperature, 'T_{aw}', is the theoretical temperature which the wall would reach if there was no heat transfer to the surface. Many papers published in the extant literature use the previously described film temperature 'T_f' interchangeably with T_aw. If T_f is the driving temperature in the convective heat transfer process (ignoring the temperature gradient between T_f and the wall), this assumption should be valid. As the adiabatic effectiveness approaches unity, the adiabatic wall temperature approaches the coolant temperature indicating a more effective scheme.

$$\eta = \frac{T_\infty - T_{aw}}{T_\infty - T_c} \tag{2.6}$$

Many factors affect cooling effectiveness including hole geometry, freestream and wall temperatures, hole arrangement and spacing, injection angle, and the mass flux ratio. This ratio is denoted by 'M' and is known as "blowing ratio." It can be found by equation 2.7.

$$M = \frac{\rho_c U_c}{\rho_\infty U_\infty} \tag{2.7}$$

Blowing ratios in gas turbine cooling schemes typically range between 0.5 and 2. Higher blowing ratios can result in the film detaching from the surface, lessening or even negating its effect [4].

2.3 Hydrocarbon Combustion

Hydrocarbon combustion is a chemical reaction globally following equation 2.8 in air. The heat release from this reaction is harnessed to meet the vast majority of humanity's current energy needs.

$$C_xH_y + (x + \frac{y}{4})O_2 + 3.76(x + \frac{y}{4})N_2 \rightarrow xCO_2 + \frac{y}{2}H_2O + 3.76(x + \frac{y}{4})N_2 \tag{2.8}$$

Quantification of fuel-rich or fuel-lean conditions is typically indicated using the equivalence ratio, ϕ, shown in equation 2.9. This quantification takes a given mass ratio of fuel to air, m_{FA} and divides it by the stoichiometric mass ratio of fuel to air, $m_{FA,stoich}$. Thus, a ϕ greater than one indicates fuel-rich conditions and a ϕ less than one indicates fuel-lean conditions.

$$\phi = \frac{m_{FA}}{m_{FA,stoich}} \tag{2.9}$$

A region where fast combustion is occurring is known as a flame. Flames fall into four major categories. The primary distinction is whether they are premixed or diffusion flames. Premixed flames have well-distributed oxygen and fuel before encountering the flame front, whereas diffusion flames mix oxygen and fuel in and near the flame front. Both of these types of flames can occur in laminar or turbulent flow fields, leading to four overall categories. In gas turbine combustors and turbines, the flowfield is intentionally turbulent in order to enhance mixing, mass transport, and flame speeds. Modern combustors use some degree of premixing, but this thesis focused on the effects of injecting fuel-free air into fuel-rich regions already above the autoignition temperature. The resultant flames therefore will be exclusively turbulent diffusion flames for the applications of the current research. A parameter of key interest to characterizing these flames is the Damköhler number, which is the ratio of a characteristic flow time to a characteristic chemical time [26]. The characteristic chemical time for the flame is usually based on estimates of the

flame speed and thickness. The current research involves autoigniting flames, making the flame speed less of a useful parameter. Because of the unique characteristics of the flames found in the current research topic, obtaining informative scaling for the Damköhler number was a new challenge.

2.4 Combustor Liner Design

As turbine designs come to interact with reacting flows, key similarities to combustor liner designs arise. The ability of the structure to withstand high temperatures and mechanical loading under reactive flow conditions is present in both components. As such, an investigation into combustor liner design methodology has yielded insight into turbine cooling configuration design. A side view of a typical modern combustor can be seen in Figure 2.4.

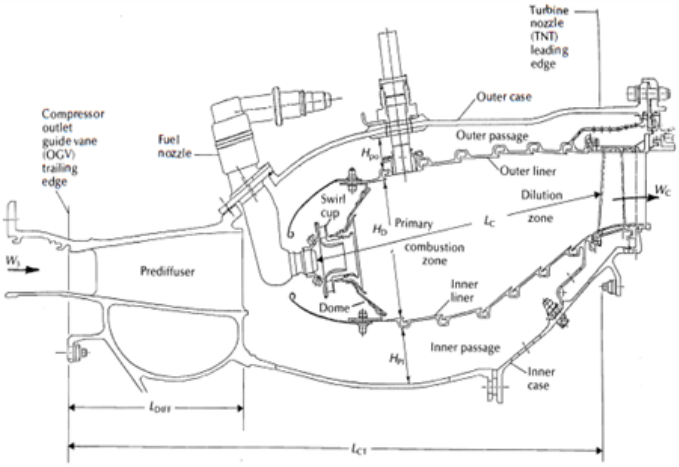

Figure 2.4: Typical Modern Combustor: GE CF6-80C [17]

Mongia gives an overview of the historical evolution of combustor design methodology in Reference [20]. His paper shows that until the 1970's, design was completely reliant on empirical correlation and extensive testing. As computational means became more available, they were employed to provide qualitative insight into flow dynamics. The

1980's saw the advent of hybrid modeling, wherein empirically determined correlations were applied numerically to produce more accurate predictions. In the 1990's, computational power and modeling became effective enough to analytically design combustors by means of Computational Fluid Dynamics (CFD). These methods were "anchored" by manipulating the models to match experimental data. The cost advantage of this anchored methodology came from having to do less testing. The paper, written in 2001, notes the need of further validation of pure CFD techniques in real-world application. In particular Mongia cites the need for much-improved accuracy in liner temperature calculations due to insufficient radiation models, near-wall turbulence modeling, and cooling effectiveness prediction [20].

Reference [17], a handbook on combustor design by Mellor et. al., provided much insight into the applicable physics for combustor liner cooling. As described in section 2.2, turbine film cooling aims to reduce convective heat transfer to the wall. Mellor et. al. show that the combustor liner must reduce the same type of convective heat transfer, and additionally must undergo radiative heating from the flame. A typical heat transfer model for combustor liners is illustrated in Figure 2.5.

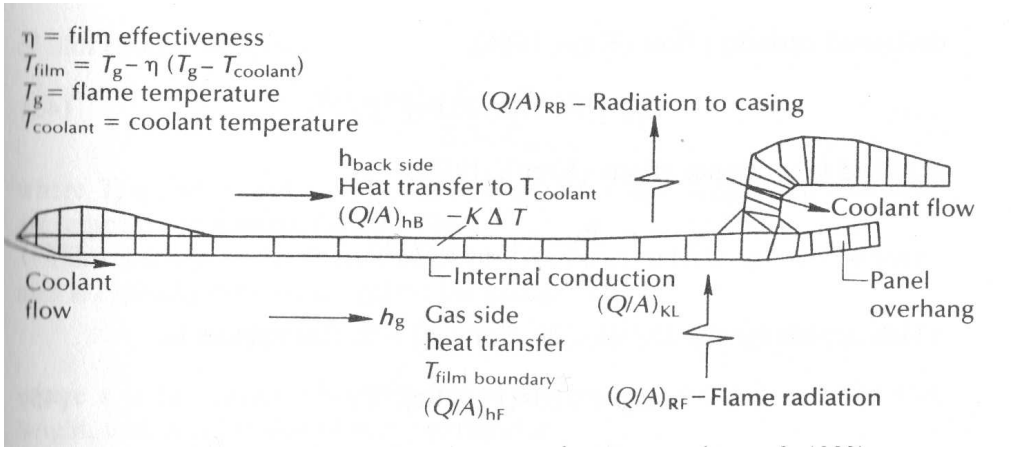

Figure 2.5: Typical 1-D Heat Transfer Model for a Combustor Liner [17]

As shown in the model, combustor liners benefit from cold-side radiative cooling to the engine case and cold side convective cooling. The cold side of a turbine blade will not experience radiative cooling because it faces an enclosed cavity. This lack of cold-side radiative cooling and presence of hot-side radiative heating compounds the cooling problem for turbine blades exposed to reacting flows. Mellor's book described an informative empirical correlation of flame-side radiation as follows: Treating the wall and flame as gray bodies, the radiation can be estimated by the correlations in equations 2.10 to 2.15.

$$R_H = \sigma(\frac{1+\epsilon_w}{2})(\epsilon_g T_g^4 - \alpha_g T_w^4) \tag{2.10}$$

$$\epsilon_g = 1 - e^{zL} \tag{2.11}$$

$$z = -0.286P(fl_b)^{0.5}T_g^{-1.5} \tag{2.12}$$

$$l_b = 3.4\frac{Volume}{SurfaceArea} \tag{2.13}$$

$$L = 0.0691(\frac{C}{H} - 1.82)^{2.71} \tag{2.14}$$

$$\alpha_g = \epsilon_g \frac{T_g}{T_w}^{1.5} \tag{2.15}$$

Mellor et. al. describe the 'L' parameter as a modifier to the gas emissivity, ϵ_g, that accounts for soot based on the carbon, C, vs. hydrogen, H, content of the chemical makeup of the fuel. propane produces L=1.0, reflecting a low-soot property of propane flames [17]. This thesis had to consider this effect, as it used propane as a fuel. Transition to a heavier, kerosene-based fuel for real-world application could result in more soot formation, and

a corresponding higher radiation flux to the wall, resulting in the current research under-predicting the heat transfer of reacting films.

Mellor et. al. conclude the treatise on cooling design with an preliminary design example. The outcome of the prediction shows that heat flux to the wall is purely a result of radiation. The film cooling is sufficiently effective, and is refreshed often enough to actively cool the wall, resulting in heat transfer from the hot side of the wall to the coolant. The book states that well-designed film cooling in combustors will accomplish this active cooling [17].

Reference [19] is Mongia's companion paper to his previously discussed effort, and was written in the same time period. It covered combustor liner wall temperature calculation in more detail. The focus of the research was primarily on computational prediction of film effectiveness (see equation 2.6). Although the paper noted the need for much more validation and improvement of its CFD models, it was able to predict liner wall temperatures of the GE90 turbofan combustor to within seven percent [19]. Mongia's results suggest that future application of computational methods to reactive film cooling may prove effective.

Mongia's paper also discusses several types of cooling used in combustor liners. The primary method discussed is film cooling by means of slot injection. The paper describes typical combustor liner construction, consisting of an axial stack of joined panels (this configuration is evident in figure 2.4). An offset exists at the end of each panel, where coolant is injected through a slot. It is typically impinged on the trailing edge of the previous panel to provide additional cooling. This impingement creates a stagnation point and a very high convective heat transfer coefficient, allowing the coolant to pull more energy out of the wall. Mongia illustrates this type of cooling in cross-section in figure 2.6.

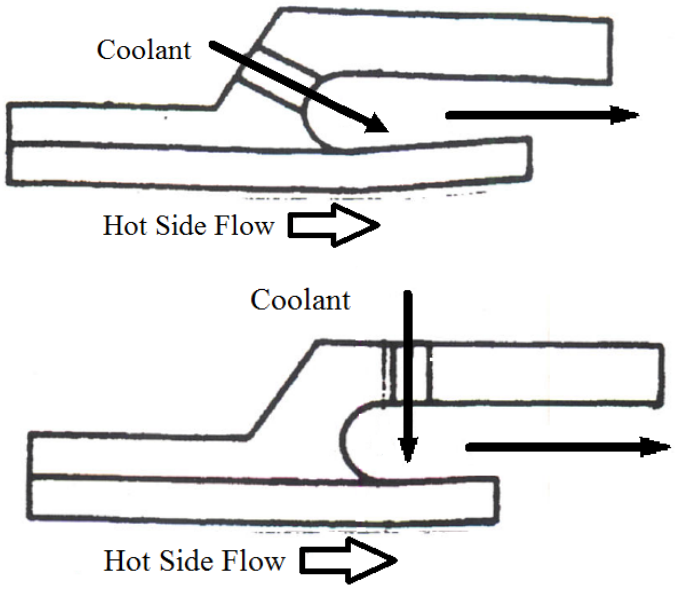

Figure 2.6: Two Impinging/Film Cooling Arrangements: Liner Cross-Section [19]

Slot cooling configurations are discussed in references [19] and [17]. To the author's knowledge slot cooling schemes are still ubiquitous in modern combustors. In recent years, however, combustor liner cooling research has been focused more on the concept of effusion cooling. A study by Kakade et. al. describes effusion cooling as a practical application of the concept of transpiration cooling [12]. The paper states that ideal transpiration cooling passes coolant through a porous wall (maximizing internal surface area exposure and heat transfer) before perfectly attaching a cool film on the hot side of the wall. However, no transpiration-type material has been discovered that can demonstrate adequate durability in a combustion environment. The compromise solution is effusion cooling, which injects coolant onto a hot wall via many manufactured holes. The holes provide internal surface area for the coolant to convect heat away from, and cause a coolant film to form on the hot-side wall. Larger amounts of smaller holes lead to more internal exposed surface area and more effective effusion as the ideal of transpiration is approached.

Practical limits on hole size are set by clogging considerations from air impurities [12]. The paper by Kakade et. al. focused on experimentally characterizing film effectiveness of an effusion scheme subjected to differing levels of freestream turbulence. Their research, conducted with 20° angled cylindrical holes, showed separation occuring above blowing ratios of 1.0. However, high freestream turbulence (22%) was found to slightly improve the film effectiveness as blowing ratio increased. The effect of increasing blowing ratio on cooling effectiveness in turbulence is shown graphically in Figure 2.7. The colormap shows a blowing ratio of 0.47 in the top row, and a blowing ratio of 0.7 in the bottom. The left column shows low turbulence levels and the right shows high.

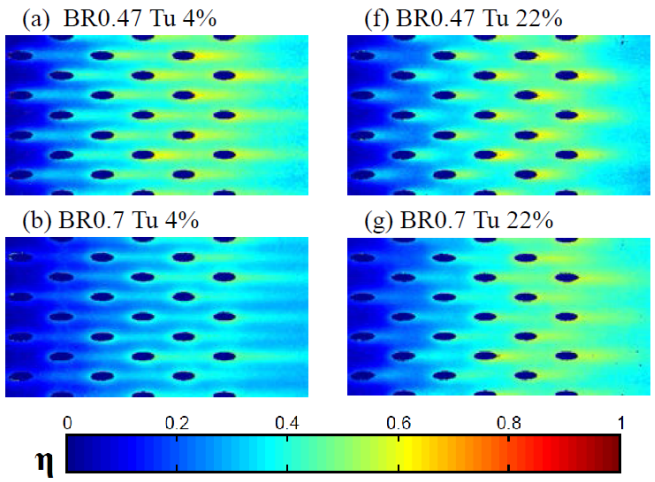

Figure 2.7: Kakade effusion adiabatic film effectiveness, m=0.47 and m=0.7 [12]

The authors of the paper conjectured that the turbulence convected separated coolant back to the wall [12]. Their finding has interesting implications for reactive turbine film cooling. Flow that is intentionally separated in order to consume radicals might also be convected back to the wall in high turbulence, reducing the cooling scheme's ability to provide separation between the flame and the protected surface.

Another paper on effusion cooling by Oguntade et. al. discussed the impact of varying injection angle on adiabatic film effectiveness for effusion cooling schemes [23]. The paper presents a CFD comparison of effusion injection at 30° , 90° , and 150° from the streamwise coordinate. The effect of angle variation on film effectiveness is shown in Figure 2.8. The upstream and normal holes are shown to have greater and more distributed adiabatic effectiveness than the co-flow injection holes, especially as higher blowing ratios and greater separation is achieved [23]. High blowing ratio cooling schemes that might have application in reactive film cooling situations may be able to take advantage of this increased effectiveness.

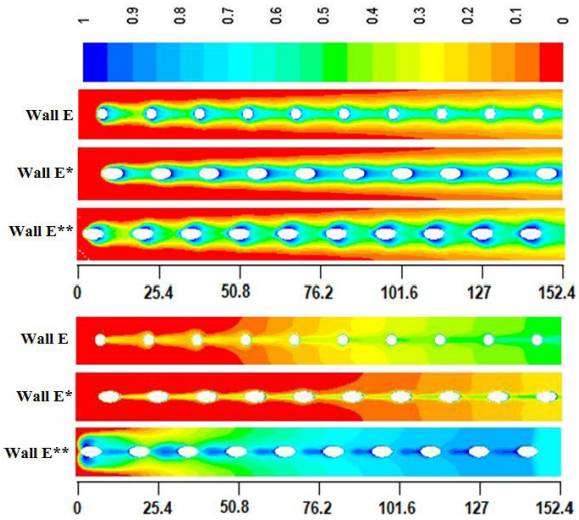

Figure 2.8: Oguntade adiabatic effectiveness, normal (E), co-flow (E*), and counter-flow (E**) injection, m=0.49 and m=2.47 [23]

Another finding of Oguntade et. al. of great relevance to reactive film cooling is the penetration and vortex structure of the upstream injection and normal injection holes, as demonstrated in Figure 2.9. These pictures show a cross-section of the flow at the 76.2 mm

location shown in Figure 2.8 for a blowing ratio of 2.47. This location has a developed flowfield and has experienced five successive rows of injection holes.

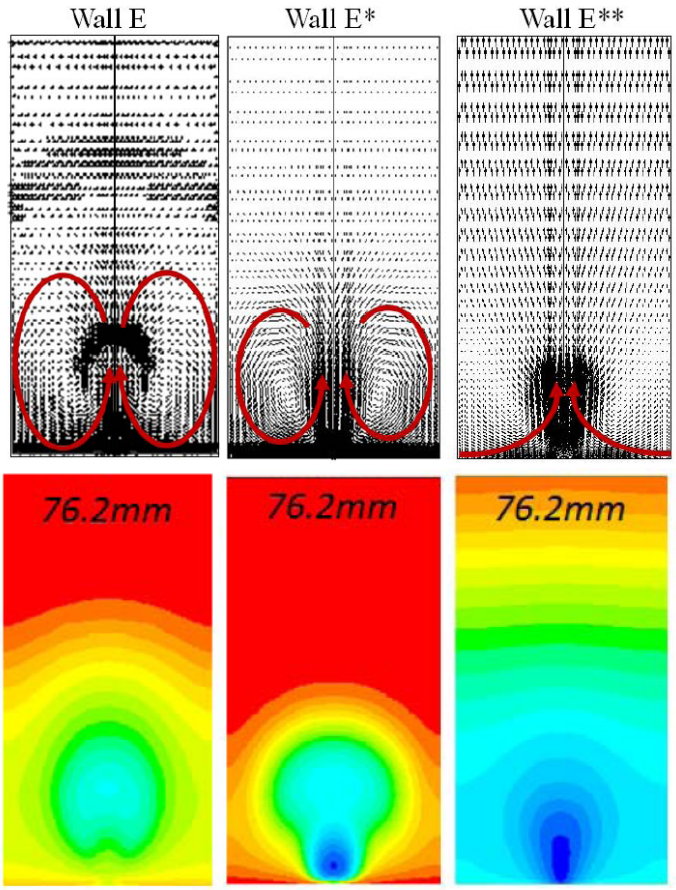

Figure 2.9: Oguntade downstream vortex structure and temperature penetration, normal (E), co-flow (E*), and counter-flow (E**) injection [23]

As shown in the figure, upstream injection leads to a high degree of flow penetration and mixing away from the wall. Normal injection also creates high mixing conditions, although not to the same extent as the counter flow scheme. The velocity gradients in the cross section shown indicate a high degree of vorticity induced by the injection in all cases. However, while the vortex structures appear to extend the entire height of the flow penetration for the normal and co-flow configurations (E and E* respectively), they do not

appear to do so for the counter-flow scheme. Instead the counter-flow vortices appear to be located farther from the wall. Both the normal and counter-flow injection schemes appear to be influencing the flow all the way to the height boundaries of the figure. [23]. The high vorticity of an upstream injection configuration could therefore translate to rapid mixing and radical consumption, helping to fulfill a major objective of this thesis. An interesting result visible in Figures 2.8 and 2.7 is that the film effectiveness profile begins appearing in a much more regular pattern after approximately five rows of coolant have been injected. This suggests that adding more rows of coolant in the immediate vicinity might have less impact on film effectiveness.

2.5 Reactive Film Cooling

Study of the effects of reactive film cooling began with Kirk et. al. in 2002 [13]. The research examined the effects of reactive film cooling with shock tube experiments, focusing effort on regions of CO recombination, which can be indicative of major heat release in hydrocarbon oxidation chains. The study identified the potential of film cooling to degrade turbines due to the presence of fuel radicals and began the current research chain. It also defined Damköhler number as the ratio of the time the freestream takes to pass ten hole diameters to the ignition time of the cooling hole flame. The flow time was selected to correspond to the experiment's measured peak heat release. The ignition time was assumed to be 10% of the time the flame took to reach 95% reaction completion [13].

A different paper on the same series of experiments by Lukachko et. al. [16] established more rigorous conventions for the definition of three additional Damköhler numbers for reacting films: The first defined a ratio of blade convection time to ignition time, such that $Da = \frac{\tau_{conv}}{\tau_{ign}}$. Blade convection time is defined as the bulk flow residence time on a turbine blade of interest, and the ignition time is defined as the time for the coolant to reach 5% of its potential flame temperature rise. $Da << 1$ would then indicate ignition after the coolant flow left the blade surface, minimizing the potential of coolant-augmented

heat transfer. A second *Da* was defined as the ratio of blade convection time to reaction time, $\frac{\tau_{conv}}{\tau_{react}}$. Reaction time is defined as the time for the coolant-induced flame to reach 95% of its potential temperature rise. This *Da* governs the distribution of the heat rise over the flow path. A final *Da* was proposed as the ratio of mixing time to reaction time, $\frac{\tau_{mix}}{\tau_{react}}$, characterizing the impact of the mixing characteristics of the configuration on the resulting reactions. The mixing time scale must be determined for a cooling configuration by experimentation or analysis [16]. These definitions are of great use in characterizing reacting films.

The first studies that attempted to mitigate the effects of reactive film cooling focused on the effect of hole shape on downstream cooling effectiveness. An initial experiment by Evans used a similar test setup to the one used in the current study [9]. It consisted of a 5.08 cm by 5.08 cm test section supplied by a well stirred reactor. A picture of the test rig is shown in Figure 2.10.

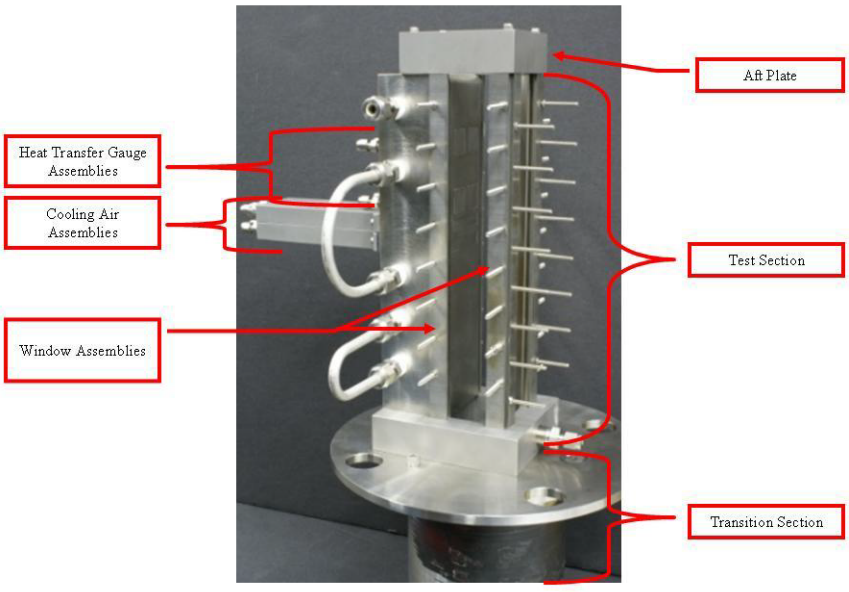

Figure 2.10: Evans Rig [9]

The major conclusion of Evans' work found that the fan-shaped geometry typically found in modern film cooling schemes resulted in greatly increased wall temperatures for reacting vs. non-reacting coolant. The geometry of this hole is shown in Figure 2.11.

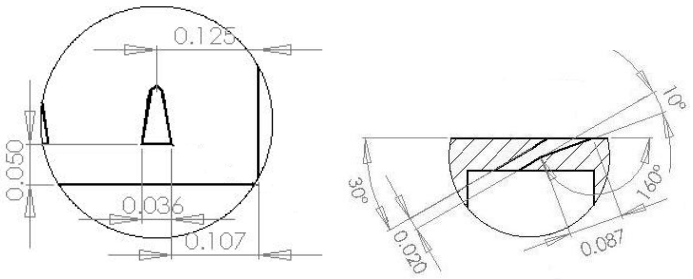

Figure 2.11: Evans' Fan Shaped Cooling Hole [9]

For comparison, he also tested cylindrical holes angled at the same 30° above the wall, and cylindrical holes injecting normally to the flow. These holes were the same 0.51 mm diameter as the basis of the fan-shaped injection holes, and injected at the same locations in the test rig. The overall performance of these configurations, denoted by an effective convective heat transfer coefficient, h_{eff} (calculated with equation 2.5), is shown in Figure 2.12.

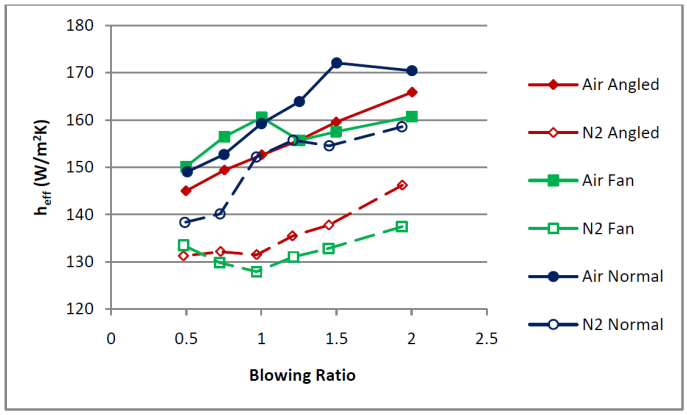

Figure 2.12: Evans' comparative convection for 3 configurations [9]

The fan shaped hole still provided marginally lower effective heat transfer coefficients at higher blowing ratios in fuel-rich environments. However, the cylindrical angled hole performed better overall at lower blowing ratios, and both cylindrical geometries were found to have much less degradation in effectiveness for reacting vs. non-reacting cases as shown in Figure 2.13. This finding pointed to the possibility of exploring non-traditional cooling hole geometries and configurations in order to improve the performance of reacting film cooling.

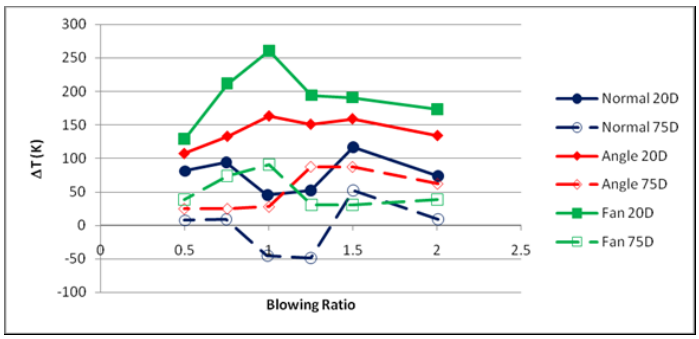

Figure 2.13: Evans' Wall Temperature Increase for Reacting vs. Non-Reacting Coolant [9]

Figure 2.14 shows a CFD simulation of injected flows performed by Kirk et. al in their preliminary study of reactive film cooling [13]. Cases 1a and 1b show an attached jet with reacting and non-reacting flow respectively. The high temperature reacting flow is located immediately adjacent to the wall following its reattachment after a separation bubble. This effect creates higher temperatures than are seen in the freestream flow, and would increase heat transfer to a wall. Cases 2a and 2b show the same contrast for a detached jet. The impact of reactions on heat release can be seen immediately downstream of the jet, where gas temperatures have increased above their freestream values faster than they did in the attached reacting jet [13]. The combination of the these simulations suggest a potential strategy moving forward. If a detached jet can be used to consume free radicals

immediately upstream of an attached jet, an overall greater film cooling effectiveness can be achieved in the presence of a reactive boundary layer.

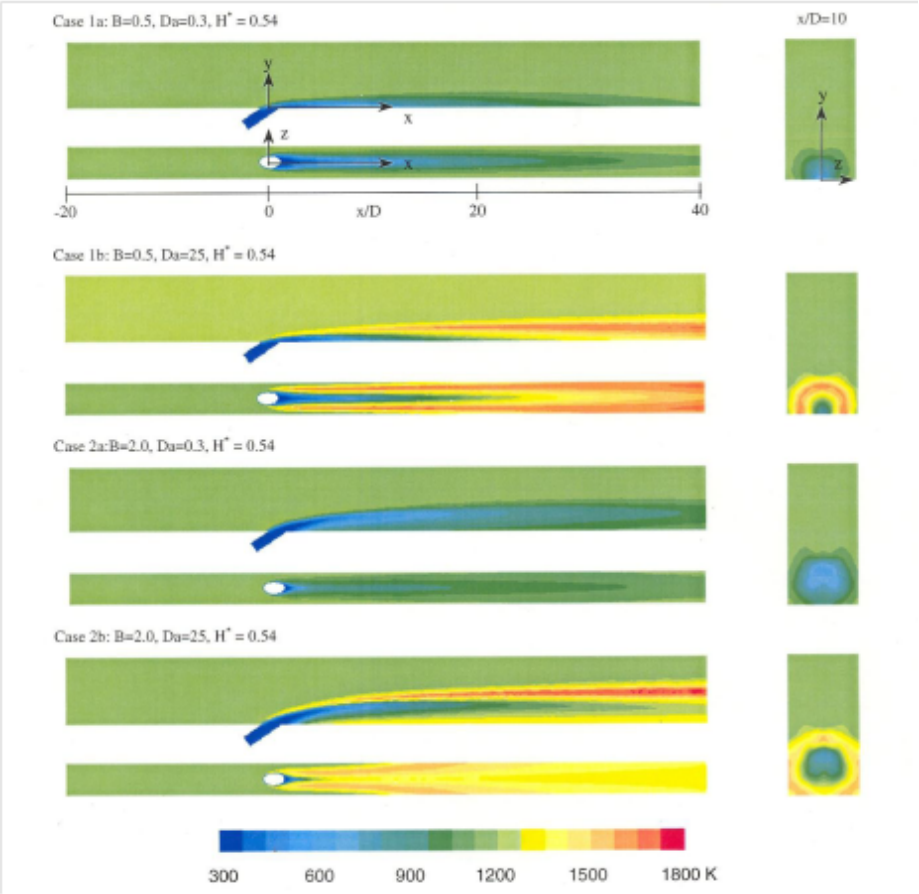

Figure 2.14: Numerical Computation of Temperature Profiles in Reacting and Non-Reacting Jets [13]

DeLallo demonstrated this effect with the addition of an upstream slot [8]. The slot cooling serves as a buffer between the fuel-rich freestream flow and the oxygen-rich fan shaped hole. An example of these results is shown in Figure 2.15. As the upstream slot's volumetric flow increases, the amount of radicals consumed also increases, thereby reducing downstream heat transfer to the wall on the order of 50%.

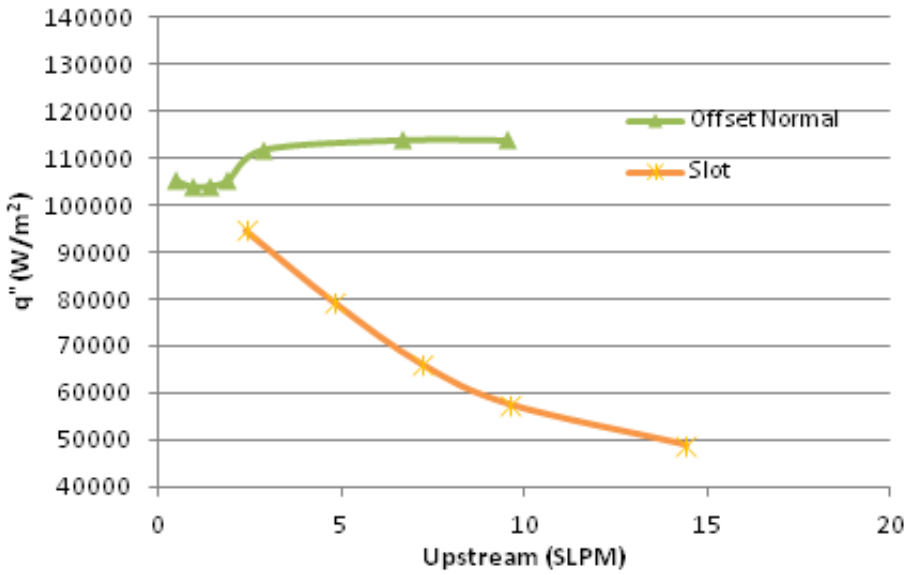

Figure 2.15: Heat Transfer to Wall With and Without Upstream Slot Implementation [8]

Both Evans' and DeLallo's experiments were conducted on a flat plate test rig. They only were able to take heat flux measurements at locations 25 diameters and 100 injection hole diameters downstream of the cooling injection. Measurements were later taken by Bohan et. al. with Planar Laser Induced Fluorescence (PLIF) to identify flow regions where reactions were concentrated [6]. The experimentation utilized the previously described Evans Fan geometry. Representative results from the experiment are shown in Figure 2.16.

The PLIF results revealed that the reactions were initiating closer to the holes and that concurrent heat release was occurring closer than 25 diameters downstream of injection [6]. This effect caused the initial experiments of Evans and DeLallo to miss some of the effects due to reacting flows immediately downstream of injection.

Establishment of a coolant layer before the arrival of freestream radicals may also have benefits. Johnson et. al. [11] performed an informative CFD analysis of cooling for a UCC configuration. Figure 2.17 shows gas temperature profiles around a cross-section of a vane. The left image is uncooled, while the right is cooled by two slots injecting

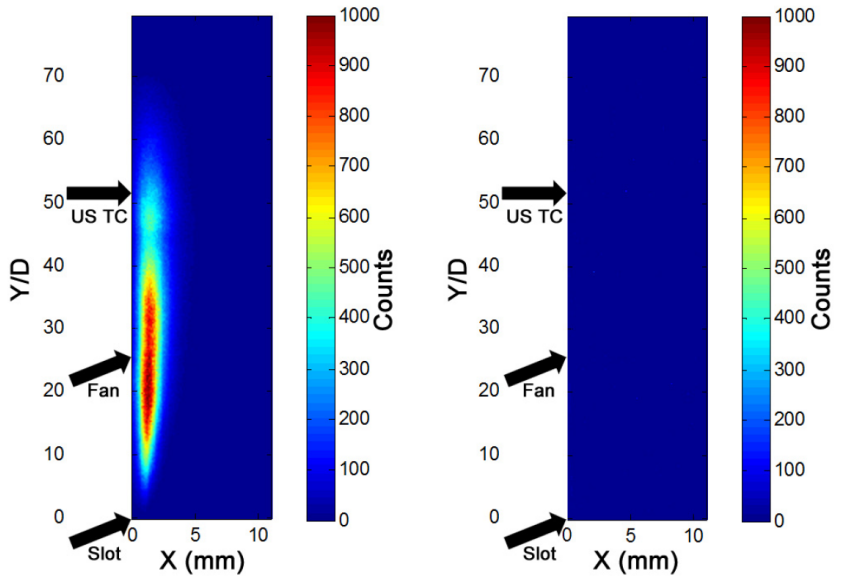

Figure 2.16: PLIF Measurements showing reaction-indicative OH radical presence shown by photon counts

near the leading edge. The vane is located in flow that experiences significant free-stream radical concentration due to its proximity to a UCC cavity. High temperature regions can be seen in the cooled case near the slot injection points. While the slots create high gas temperatures near the leading edge of the vane, the gas temperature profile is improved near the trailing edge due to earlier radical consumption [11]. The broader temperature distribution would be easier to cool further downstream, but requires special attention near the injection points. At a glance the analysis shows some of the potential benefits and hazards of cooling configurations that intentionally create radical-consuming flames.

A visualization of Johnson's analysis further away from the UCC cavity is shown in Figure 2.18. Fewer freestream radicals are present at this location, and none are located at the slot injection point. The cooled case shows the significant delay of the start of the high temperature region, moving from approximately the 'C' location to the 'D' location. Additionally, the trailing edge gas temperature profile also shows improvement in the

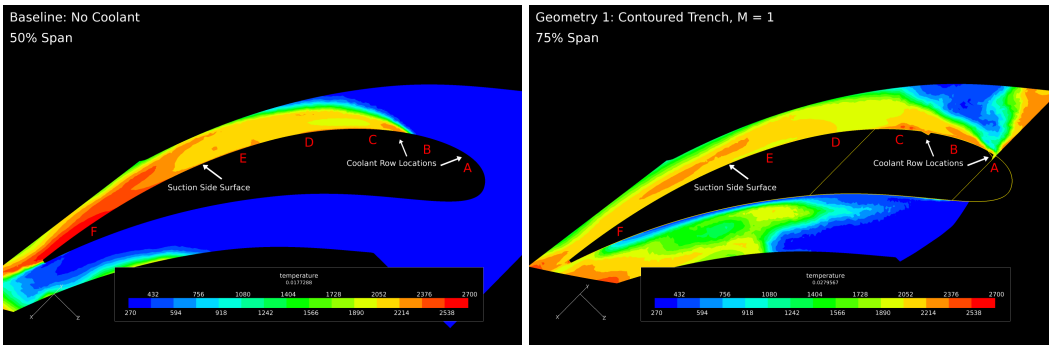

Figure 2.17: Johnson CFD analysis of reacting coolant on UCC hybrid vane, 50% radial location from inner radius, left: uncooled, right: cooled with two suction side slots [11]

cooled case. This analysis suggests that a coolant layer established prior to interaction with radicals can remain effective for longer distances and delay the onset of reaction-induced blade heating.

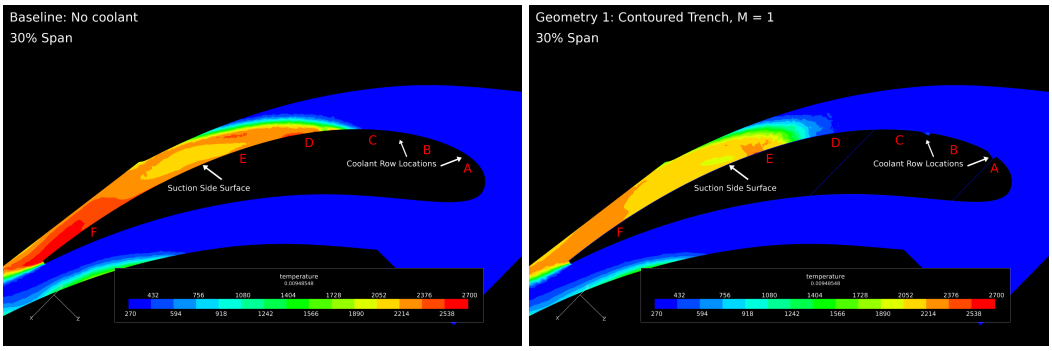

Figure 2.18: Johnson CFD analysis of reacting coolant on UCC hybrid vane, 30% radial location from inner radius, left: uncooled, right: cooled with two suction side slots [11]

The delayed high-temperature onset effect can be applied to the current research: If near-wall radicals can be mostly consumed prior to coolant introduction, the resulting cooling configuration might become more effective. Also, Johnson's research implies that once established, a non-reacting attached coolant layer will remain effective for at least

some distance downstream. A configuration that produces both of these effects would allow cooling configurations to consume radicals and protect the wall, fulfilling the major thesis objectives.

2.5.1 Determination of Adiabatic Wall Temperature.

An article by Popp et. al. [24] showed a means of determining convective heat transfer coefficient and adiabatic wall temperature by using heat flux measurements in the wall. By taking heat flux data at separate wall temperatures and constant freestream conditions, a linear correlation can be determined. The slope of this correlation corresponds to the value of the convective heat transfer coefficient, as shown in Figure 2.19. If this slope is extrapolated to the point of zero heat flux, the adiabatic wall temperature is known [24].

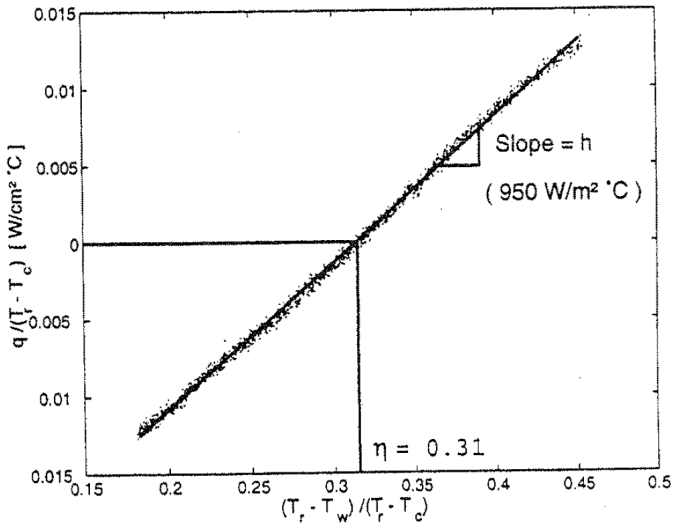

Figure 2.19: Extrapolation to Zero Heat Transfer [24]

DeLallo's experiment [7] also attempted to apply the methodology of Popp et. al. to finding the adiabatic wall temperature [8]. The assumption of linear convective heat transfer coefficient was made for this study because it was shown to be valid in Popp's research. Two data points at different wall temperatures were taken to draw each constant 'h' line.

DeLallo obtained these points by first using cold-side water coolant, and then heated oil. By contrast, Popp's experiment used the transient increase of the wall temperature over time to construct the slope. The results of DeLallo's study are shown in Figure 2.20

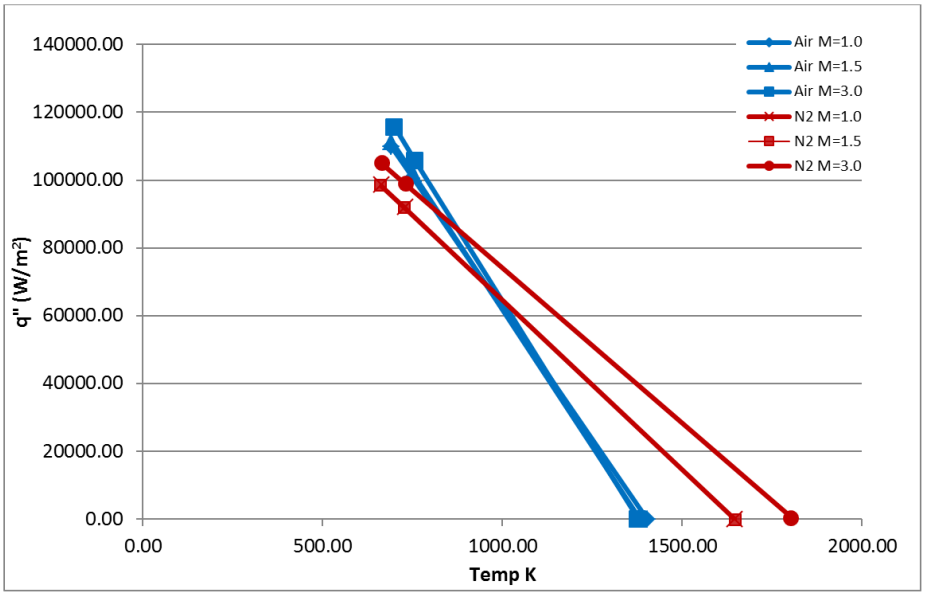

Figure 2.20: DeLallo Wall Temperature Study, Normal Trench cooling arrangement, $\phi = 1.3$ [8]

DeLallo found that a lower adiabatic wall temperature was calculated for the reactive case (run with air as a coolant), than for the non-reactive case (using N_2 as a coolant). This result does not make physical sense. The reacting coolant produces higher freestream temperature than the non-reacting coolant. The reacting case should thus require a corresponding higher T_{aw} in order to produce zero heat transfer. Because the results were obtained based on a two-point extrapolation, the problem is assumed to be one of non-linearity in the curves, suggesting that the method presented in Popp et. al. is not valid at these flow conditions.

At the time of this writing, research is being performed by Greiner et. al. to thoroughly explore the effect of wall temperature on heat transfer for reacting flows [10]. Their research is using the same experimental setup used in the research of this thesis. A sample of their results is shown in Figure 2.21. Empirical measurements are shown against an array of different analytical methods for predicting flat plate heat transfer in turbulent flows. The research by Greiner et. al. has shown definitively that non-linearities exist in the effective heat transfer coefficient at gas turbine representative flow conditions.

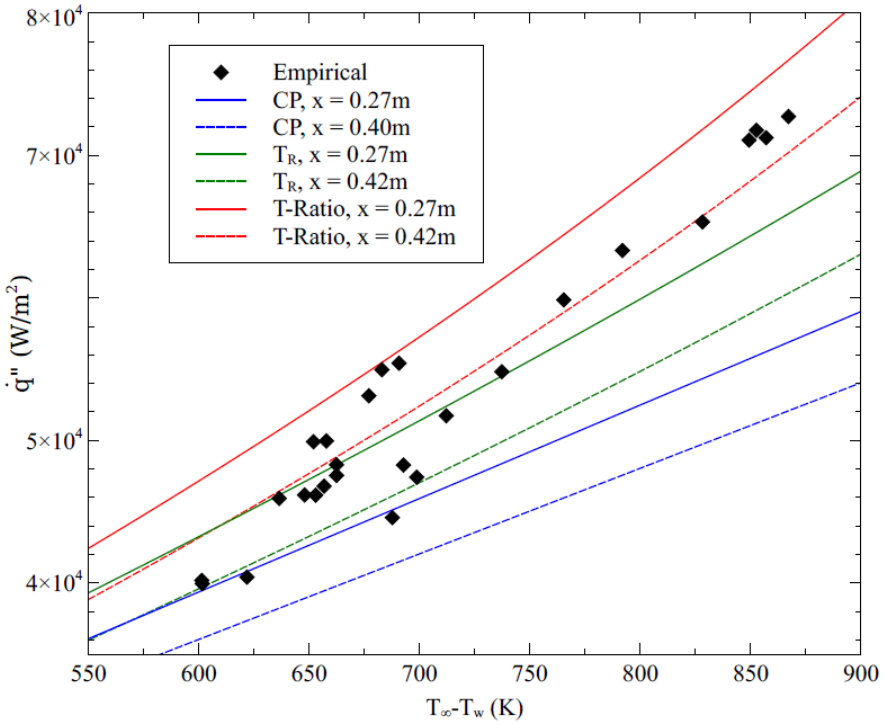

Figure 2.21: Greiner et. al. Wall Temperature Study, no film cooling, $\phi = 1.3$ [10]

2.5.2 Evaluation of Reactive Film Cooling.

Because the traditional metric of adiabatic effectiveness is impossible to use without a reliable determination of T_{aw} (see Equation 2.6), another means of evaluation is necessary. DeLallo proposed using heat flux augmentation (heretofore referred to as augmentation or

σ) as a useful tool [7]. This is simply the percentage change in heat flux for otherwise identical flow conditions from a non-reacting to a reacting case. This is shown in Equation 2.16.

$$\sigma = \frac{q''_{reacting} - q''_{non-reacting}}{q''_{non-reacting}} \tag{2.16}$$

The aforementioned dependence of convective heat transfer coefficient on wall temperature will affect the results shown by augmentation. If the air case and N_2 case are measured at different wall temperatures, it will change the degree of augmentation according to equation 2.5. However, it is impractical to control all test points to identical wall temperature with the current test rig. Because adiabatic film effectiveness is not practical for implementation in the current research, augmentation will be used as the primary means of evaluation for film cooling schemes in this thesis.

III. Experimental Setup

3.1 Objectives

The primary objective of this thesis was to characterize the downstream effectiveness and heat transfer of various film cooling hole arrangements devised to protect the wall from additional heat release induced by secondary combustion. Another objective was to attempt to consume fuel and radicals at a standoff distance from the wall being cooled. Ultimately, the research aimed to create a film cooling scheme for use in a high fuel-air environment in a turbine. Previous research on reactive film cooling had failed to capture temperature and heat release data any closer than 25 injection hole diameters downstream. The PLIF experiment by Bohan et. al. showed that the majority of the heat release from the reactions occurred inside of this distance [6]. The setup used by Evans [9], Bohan [5], and DeLallo [7] was incapable of measuring heat flux and temperature in this region. As such, a new experimental rig was designed in order to obtain a fuller knowledge of the physics of reactive film cooling.

3.2 New Experimental Rig

This thesis utilized a new experimental rig constructed in conjunction with the Air Force Research Laboratory (AFRL). The rig was designed to enable the necessary test conditions and measurement capability to fulfill the Thesis objectives. The setup could achieve the fuel-rich test conditions necessary to create reacting films. Modular inserts allowed easy changing of cooling schemes on plates that could accommodate many closely spaced rows of holes. The overall flow path and layout of the new test rig are shown in Figure 3.1.

The rig passed reacted air/fuel mixture at a controlled equivalence ratio from a well-stirred reactor (WSR) to a flow straightener duct. This removed the swirl from the reactor

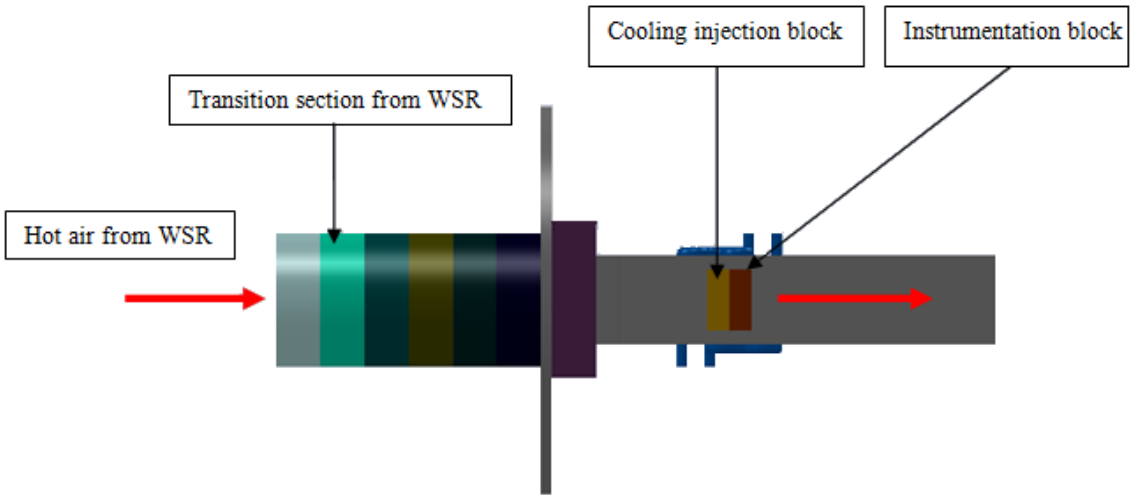

Figure 3.1: Test Rig

and turned the flow to the axial direction. From here the flow transitioned to a rectangular cross section via a series of ceramic transition rings. The cross-sectional area was 863 mm^2, and the width was 50.7 mm. The corners of the rectangular cross-section were rounded off slightly by support brackets. The hydraulic diameter was 26.4 mm. For most testing in this thesis conducted with 0.012 kg/s of air supply, $\phi = 1.175$ and a freestream temperature of 1670 K, the freestream velocity was 73.0 m/s giving a $Re_{D_H} = 6261$. Hydraulic diameter and Reynolds number were calculated using equations 3.1 and 3.2.

$$D_H = \frac{4A}{P} \tag{3.1}$$

$$Re_{D_H} = \frac{\rho U D_H}{\mu} \tag{3.2}$$

At a freestream temperature of 1670 K the mach number was 0.091. One wall of the tube housed a flush mounted film cooling injection insert and an instrumentation insert. Thermocouples inserted in the instrumentation insert downstream of the cooling scheme took temperature measurements at different flow conditions in order to characterize the

effectiveness of the film cooling at specified locations. The film cooled and instrumented wall (”test wall”) was subjected to forced cold-side convection of either oil, water, or nitrogen. This feature allowed wall temperature control and helped ensure one-dimensional heat transfer in the instrumented region. A sliding, 2.54 cm diameter sapphire window was integrated into the wall opposite the instrumentation insert. The window allowed infrared imaging of the affected area of the wall. The sliding feature allowed it to avoid exposure to the flow and subsequent coking until it was needed. Fused silica side wall windows were also integrated to allow for flow visualization and eventual optical flow diagnostics. The overall setup in the lab is shown in Figure 3.2.

The amount of air and fuel that were combusted in the WSR were precisely controlled from a digital control board. Data from pressure transducers and thermocouples was fed to a data acquisition array then to a Labview routine on a desktop computer. The data was collected via Labview, transitioned to a post-processing spreadsheet (shown in Appendix A), and further post-processed using Matlab routines (also shown in Appendix A).

3.3 Well Stirred Reactor

The test rig was supplied hot, fuel rich air from a well-stirred reactor (WSR), the design of which was initially conceived by Nenniger et al. [22] and then developed through several design evolutions at AFRL. The WSR, shown in Figure 3.3 is an Inconel toroidal combustor that allows precise control of equivalence ratio and temperature at its exit. The WSR supplied propane and air from the laboratory supplies, and was controlled with existing laboratory equipment. This allowed the experiment to simulate high equivalence ratios in support of the research objectives.

The WSR used in the experiment is a new design that was adopted in light of several lessons learned from previous research. The experiments of Evans [9] and DeLallo [7] both utilized a previous design iteration that used a ceramic toroid. The ceramic would take over

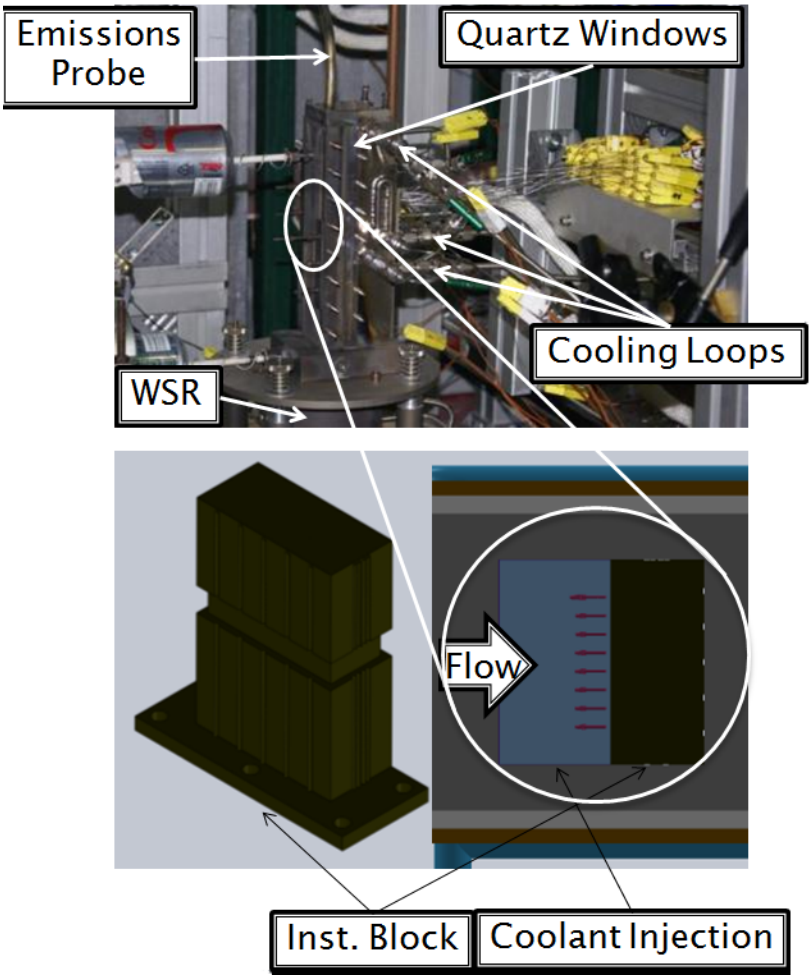

Figure 3.2: The New Experimental Rig

an hour to warm up to a steady temperature and allow consistent measurements. Its high thermal inertia also meant that any change in ϕ took significant amounts of time to obtain steady freestream temperature. In addition to these issues, the ceramic was also prone to cracking, and required frequent replacement. This behavior placed time constraints on the research performed. The new WSR is made of Inconel® and is actively cooled by water to prevent overheating. This design has the advantage of a fast warm-up period and excellent durability. The major con is that the active cooling and lower operating temperature lead to

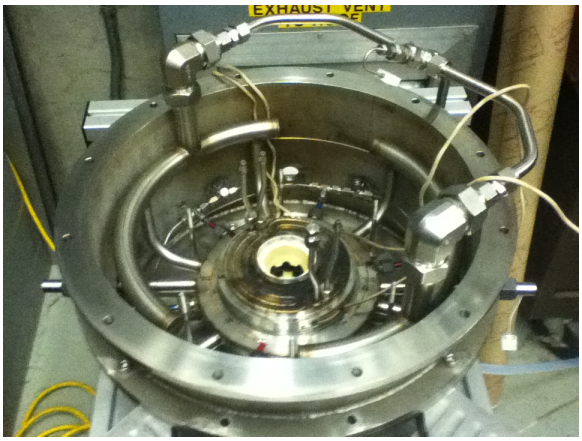

Figure 3.3: Well Stirred Reactor

lower exit temperatures of the reacted gas. This trade-off was readily accepted for the time savings and reliability that it would afford.

3.4 Transition Section

Flow entered the rectangular test section from the WSR via a transition stack made of ceramic pieces, which are housed in a metal cylinder. A cutaway side view of these pieces is shown in Figure 3.4.

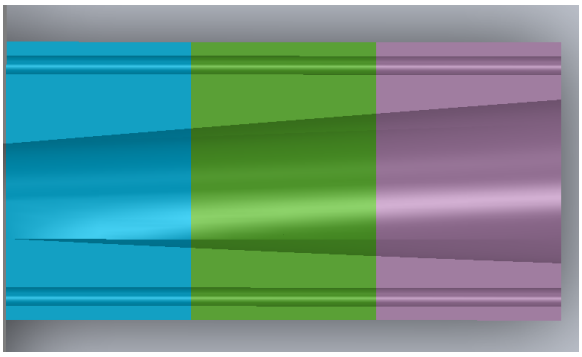

Figure 3.4: Transition Piece

The transition section also housed an internal flow straightener pictured in 3.5. Evans reported discrepancies in his spanwise measurements heat flux measurements, which he speculated was caused by the WSR [9]. The WSR swirls the combustion reactants as a natural consequence of its design. Using the same test rig, Bohan integrated an eight spoke flow straightener and reported improvement in spanwise uniformity [5]. As such the current study uses a similar eight spoke ceramic flow straightener.

Figure 3.5: Flow Straightener and Transition Section

3.5 The Hastelloy-X Block

The cornerstone of the rig is the 28 cm x 2 cm x 2 cm Hastelloy-X ® block. The block is bolted onto a circular base plate which fits to the transition section. The baseplate is structurally connected directly to the WSR housing by four rods, which are visible in Figure 3.2. It forms a wall of the flow channel and provides a mounting point for the cooling and instrumentation inserts. The block is actively cooled on the cold side by forced convection of either water, temperature-controlled oil, or nitrogen through milled and welded channels. This cold-side cooling strategy was implemented in order to provide as high a degree of 1-dimensional heat transfer through the block as possible, as shown in Figure 3.6.

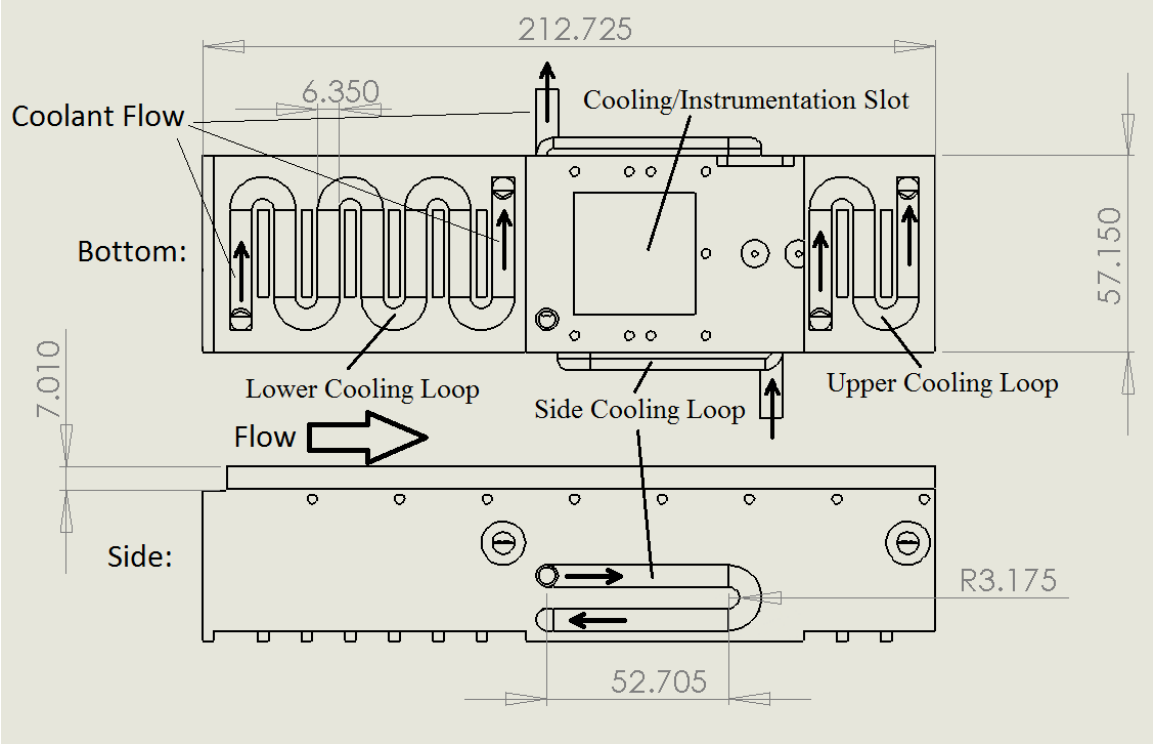

Figure 3.6: The Hastelloy-X® Block

The block also provided a step in the path of the flow in order to ensure turbulence in the passage representative of typical combustor and turbine conditions. This step is pictured in figure 3.7. The step was selected to be 7.01 mm high in order to ensure that the flow was fully transitioned to turbulence over the cooling configuration insert and instrumentation block. The methodology used to calculate this step height is detailed in Appendix B.

All testing in this thesis utilized temperature-controlled oil as the cold-side coolant. A Mokon® oil temperature control system uses a pump, electric heater, and water-cooled heat exchanger system to precisely control the temperature of the oil coming out of the machine (which is then input into the rig's cooling loops). The oil is limited to 600° F (589 K) as a maximum. At the input to the rig, the oil temperature was measured at 293° F ± 10° F for all testing except for the wall temperature study detailed in section 4.6. Before

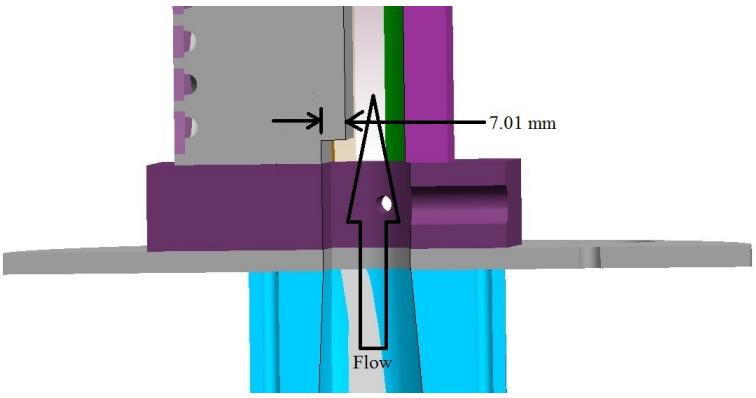

Figure 3.7: Trip included in block

insertion into the block, the flow was divided into three paths, feeding the upper, side, and lower coolant paths respectively (labeled in Figure 3.6). After passing through the block, the three coolant paths were joined and passed back to the oil system. Screw valves immediately prior to the re-joining were adjusted (changing the flow rate of each loop) such that the output temperature of all three loops was 335° ± 10° F. The outlet temperatures were desired to match in order to provide as even a cold-side cooling as possible. Future researchers may wish to quantify mass flow in the cold-side cooling loops and perform a more in-depth analysis to determine the best way to promote one-dimensional heat flux in the block.

3.6 Film Cooling Insert

Modular rectangular film cooling plates were mounted on a universal plenum and inserted integrally into the wall of the test rig. This enabled several different cooling designs to be evaluated in the same experimental set up. Additionally, the plenum enabled multiple stacked rows of cooling injection. A thermocouple was inserted into the plenum and maintained 2 mm from the wall. The resulting measurement was considered to be the coolant temperature in any calculations. This assumption neglected temperature rise

Figure 3.8: Oil Cooling System

through the plate. Several different combinations of designs were evaluated as part of this program, some of which were inspired by combustor liner design. Typical combustor liners experience high fuel-air environments similar to those of concern to this thesis. They remain cool by generating a build up effect along the wall much the same as the slot configuration of DeLallo [7]. Combustor liners also utilize high mass-flux injection normal to the flow. This type of hole generates turbulence which aides in the mixing process and enhances the reactions; another objective of the current research. The normal component of the jet also results in reactions that occur away from the wall. Successful implementation of combustor-type cooling would therefore meet all research objectives. However, combustors have the advantage of controlling the distribution of fuel in the flowfield. Combustors are intentionally designed such that radicals are statistically unlikely to be proximate to the

liner wall. Reactive film cooling in turbine blades cannot avoid the presence of radicals near the wall, and so must find a way to consume them. Other configurations that were evaluated in this program include the fan shaped and angled holes evaluated previously as well as combination of rows of holes with the objective to enhance the burning rates upstream, while cooling the wall downstream. All configurations were placed such that the trailing edge of the most downstream row of holes was 1.27 mm from the trailing edge of the cooling plate insert. This was a standard inherited from Evans' research [9].

3.7 Cooling Configurations

Two different sets of cooling configurations were produced that tested different strategies of reactive film cooling. The objectives of the first set were to build a thick coolant layer on the wall which would separate the flame from the wall, protecting the surface from the harmful effects of the reactions. This set is described in detail in Section 3.7.3. The second set attempted to enhance the rapid mixing of the coolant with the freestream flow. The objective was to consume radicals rapidly away from the wall while protecting it. This set of configurations is detailed in Section 3.7.4.

3.7.1 Comparison to Previous Results.

The first configuration was tested in order to validate the new experimental rig against results obtained in past research with similar rigs. The configuration, heretofore referred to as the Evans Fan, was identical to the baseline configuration used in Evans' and DeLallo's experiments, and is shown in Figure 3.9. Dimensioned drawings of all cooling configurations are located in Appendix E. It consisted of a single row of laidback fan shape holes injecting at a 30° angle. The laidback fan injection geometry starts with a cylindrical hole bored 30° above the streamwise coordinate with a 0.51 mm diameter. The hole is then fanned out so the trailing edge of the injection geometry is flat and injects at an angle of 20°. This shaping diffuses the flow and helps it attach to the wall, improving performance

in traditional film cooling. The injection points were spaced 6.9 diameters laterally, with eight total holes on the plate.

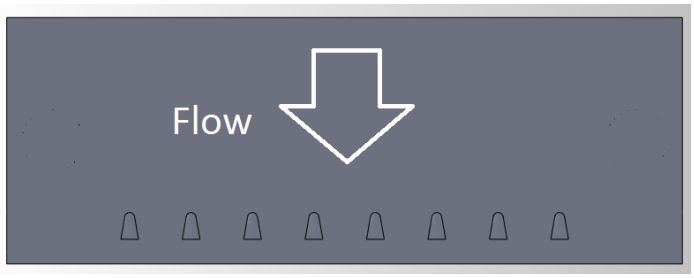

Figure 3.9: Evans' Fan Cooling Configuration

3.7.2 4D Spaced Laidback Fan.

The second configuration tested was identical to the first, except that the holes were spaced four diameters apart in order to closer match typical configurations found in the industry. The configuration is shown in Figure 3.10. Twelve total holes were thus able to be put on the plate. This configuration served as the baseline performance for the current research, and will also be used by other researchers such as Greiner in the near future.

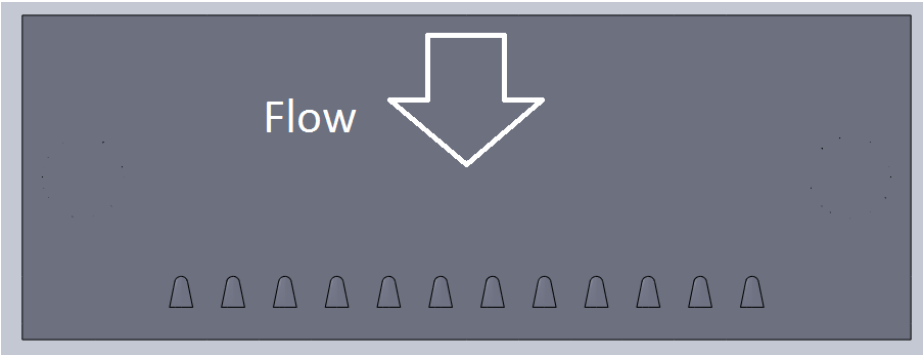

Figure 3.10: 4D Spaced Laidback Fan Cooling Configuration

3.7.3 Test Campaign 1: Row Build Up.

The first test campaign attempted to examine the effects of building up multiple rows of cooling to create a sufficiently thick coolant layer to provide separation of the reactions from the wall. The resulting type of cooling is similar to the effusion cooling described in Section 2.4. The effort concentrated on using simple cylindrical hole configurations angled 30° from streamwise. It used one row of injection as a baseline configuration, then tested three rows of injection and finally five rows of injection. Five rows was selected as a maximum because the literature shows reduced gains in effectiveness for more rows (see section 2.4).

The first configuration tested was known as the Single Row configuration. Twelve cylindrical holes with a diameter of 0.51 mm injected coolant 30° above the streamwise coordinate. The thickness of the plate was set such that the length-to-diameter ratio (l/d) was 5.0. The arrangement is shown in Figure 3.11. This configuration served as the baseline for the row buildup study.

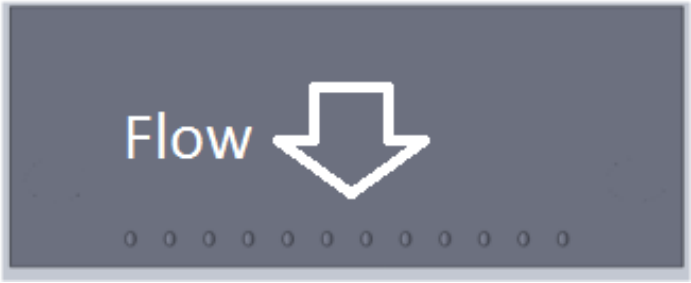

Figure 3.11: Single Row of Cylindrical Holes Cooling Configuration

The next configuration was called the Triple Row, and spaced three rows of injection holes four diameters streamwise from each other. The holes followed the standard of the Single Row configuration, with d=0.51 mm and l/d=5.0. Each row maintained four diameter spacing between holes spanwise, and the first and third rows had twelve holes.

The middle row was offset spanwise from the other two and only had eleven holes. The configuration is shown in Figure 3.12.

Figure 3.12: Triple Row of Cylindrical Holes Cooling Configuration

The five row configuration followed the same pattern, with five rows instead of three. It is shown in Figure 3.13. The second and fourth rows were offset and had eleven holes while the odd numbered rows were in line and had twelve. This was the final configuration tested in the Row Build Up testing campaign.

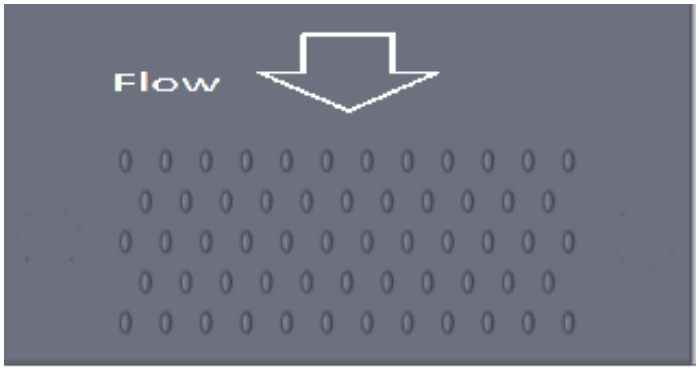

Figure 3.13: Five Rows of Cylindrical Holes Cooling Configuration

3.7.4 Test Campaign 2: Enhanced Mixing.

The research then attempted to test cooling configurations that promoted mixing and reactions away from the wall. This would allow for greater power generation and wall

protection in UCC and fuel-rich streak scenarios. Time and manufacturing constraints limited testing to three configurations, leaving room for future study on the matter.

3.7.4.1 Roll Forward.

The first mixing configuration testing was termed the ”Roll Forward” configuration, and is shown in Figure 3.14. It injected coolant at the same surface locations as the Five Row configuration, except that the upstream row of holes injected normal to the flow instead of at 30 ° . The next row injected at 75 ° , the next at 60 ° , the next at 45 ° , and the final at 30 ° . The 30 ° row was maintained such that l/d=5.0, giving the normal injection holes an l/d=2.5. The first rows injecting more normal to the flow become ”sacrificial,” with no hope of attaching a cool layer to the wall. However, the researcher hypothesized that the upstream rows would consume radicals quickly, protecting the downstream rows and allowing their attached flow to cool more effectively.

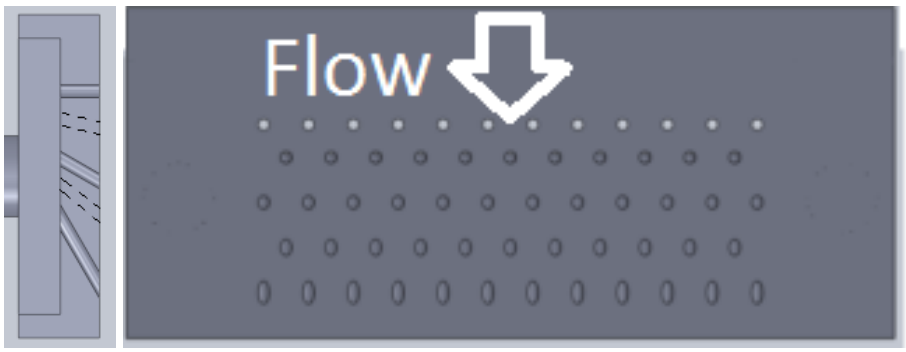

Figure 3.14: Roll Forward Cooling Configuration, Side and Top View

3.7.4.2 1 Row Upstream and 2 Row Upstream to Three Row.

The next two configurations tested used the Triple Row configuration as a baseline (see Figure 3.12). The 1 Row Upstream configuration added a row of holes eight diameters upstream of the most windward row of the 3 Row configuration, and is shown in Figure

3.15. Upstream-facing holes were tested to see if the increased penetration described in the literature (see section 2.4) could be taken advantage of in a reacting film situation.

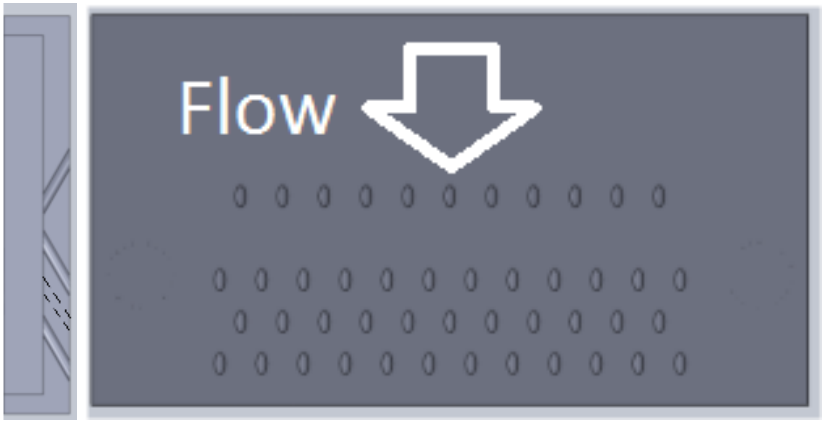

Figure 3.15: 1 Row Upstream Cooling Configuration, Side and Top View

The upstream-facing row of holes injected at a 150° angle from streamwise. The researchers hypothesized that this would further promote mixing and create swirling structures and flame zones away from the wall. The 2 Row Upstream configuration was identical, except that it added another row of holes four diameters upstream of the first that also injected at 150° . It is shown in Figure 3.16.

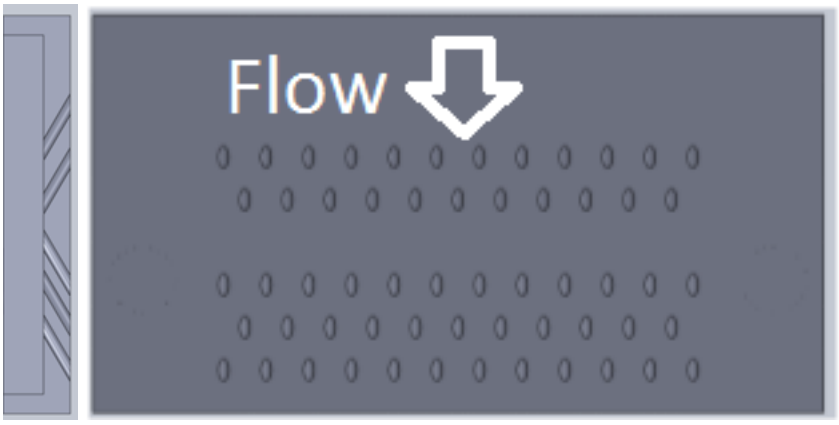

Figure 3.16: 1 Row Upstream Cooling Configuration, Side and Top View

3.8 Instrumentation Block

A removable rectangular Hastelloy-X instrumentation block was integrally inserted immediately downstream of the cooling block. The instrumentation was placed much closer to the cooling holes than has been shown previously in the literature [8], [2]. This allowed the experiment to capture surface heat flux measurements between 8 and 30 injection hole diameters downstream, vastly improving understanding of the nature of the physical phenomena. Thirty-two Omega® ungrounded Inconel 660 Type-K thermocouples were inserted into the instrumentation block forming sixteen pairs. A visualization is shown in Figure 3.17. The locations of these blocks is enumerated in Table 3.1. There are two thermocouples at each location: one "Upper" at 0.76200 mm depth from the hot gas side of the block, and one "Lower" at 5.08 mm depth. The origin of the coordinate system is centered on the trailing edge of the cooling insert, as shown in Figure 3.18. The y axis obeys the right hand rule, being positive into the block.

The instrumentation block is visible as the red piece in the wall in Figure 3.1. The standard hole diameter for this experiment was 0.51 mm. As such, this block contained two primary rows of 5 thermocouples at 8 and 30 hole diameters from the last cooling row. It furthermore contained additional thermocouples at two spanwise locations at streamwise distances of 15, 17, 19 and 21 diameters. This vastly improved the data density. Additionally, linking these temperature measurements with side window visualization provided the needed understanding of where the reactions take place and provided a better insight into the effects of design on reaction timing.

Also shown in Figure 3.17 is the nomenclature convention used for the thermocouples in the test. As illustrated, the instruments were labeled in an intuitive row/column layout. As an example the position of TC-3-2-U is indicated in the figure. The line up of the thermocouples with the injection holes is shown below in Figure 3.18, where the black dots are indicative of a thermocouple pair. All configurations tested had twelve trailing

Location	x (mm)	z (mm)
1-1	-12.2	2.39
1-2	-6.1	2.39
1-3	0	2.39
1-4	6.1	2.39
1-5	-12.2	2.39
2-2	-6.1	6.18
2-3	0	7.23
2-4	6.1	6.18
3-2	-6.1	9.53
3-3	0	8.62
3-4	6.1	9.53
4-1	-12.2	13.49
4-2	-6.1	13.49
4-3	0	13.49
4-4	6.1	13.49
4-5	-12.2	13.49

Table 3.1: Thermocouple locations in instrumentation block

edge holes centered spanwise on the wall. As such, the thermocouples lined up spanwise exactly between the holes in the trailing edge row for all configurations tested.

The construction of the Hastelloy-X® Instrumentation Block allowed the researcher to assume steady-state, 1-dimensional conduction from its hot side to its cold side. Steady state was achieved by allowing temperatures in the block to change less than 0.5° F per minute following a change in test conditions. This allowed the researcher to calculate heat flux and wall temperature by the method described in Appendix A.

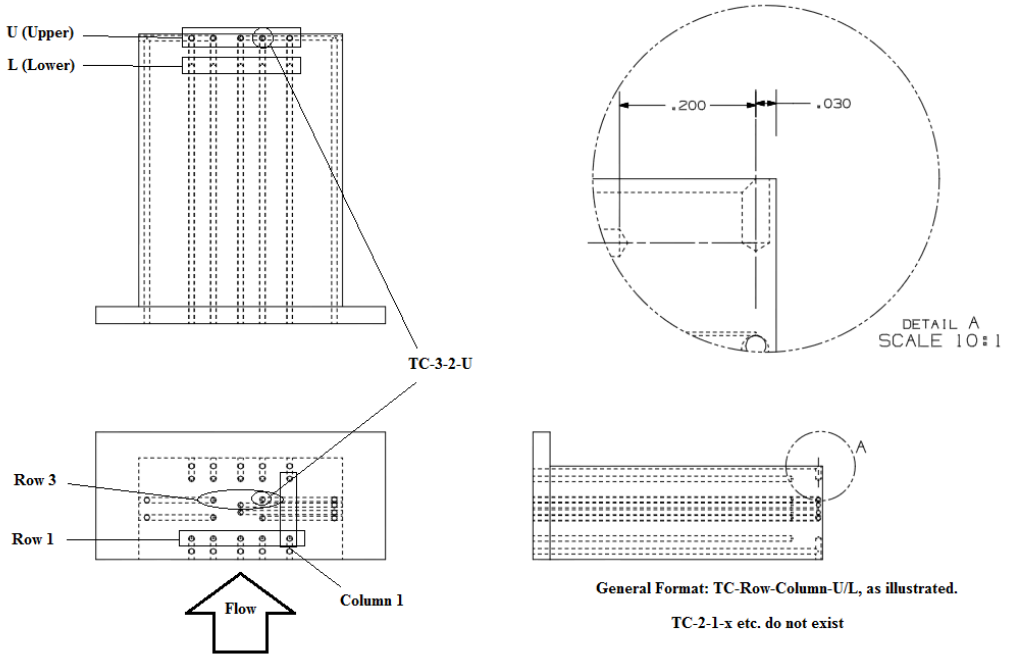

Figure 3.17: Thermocouple Configuration

3.9 Optical Acess

A fused silica side window and a 2.54 cm sliding sapphire window were integrated into the experimental setup in order to provide another means of analysis to the researcher. The sapphire window is shown in Figure 3.19. Sapphire is highly transmissive in the infrared (IR) spectrum, allowing future use of a IR cameras as a data-collection tool. The window frame was designed to easily slide in its mounting brackets. When the window was needed, it could be slipped into place easily. When not in use, the window could avoid exposure to the fuel-rich flow in the rig and consequent carbon deposits on the material.

The fused silica side windows allow visible spectrum imaging of the flow for qualitative information on flame structures created by the coolant and quantification of flame length. The side window is shown in Figure 3.20 with a ruler used to calibrate the images.

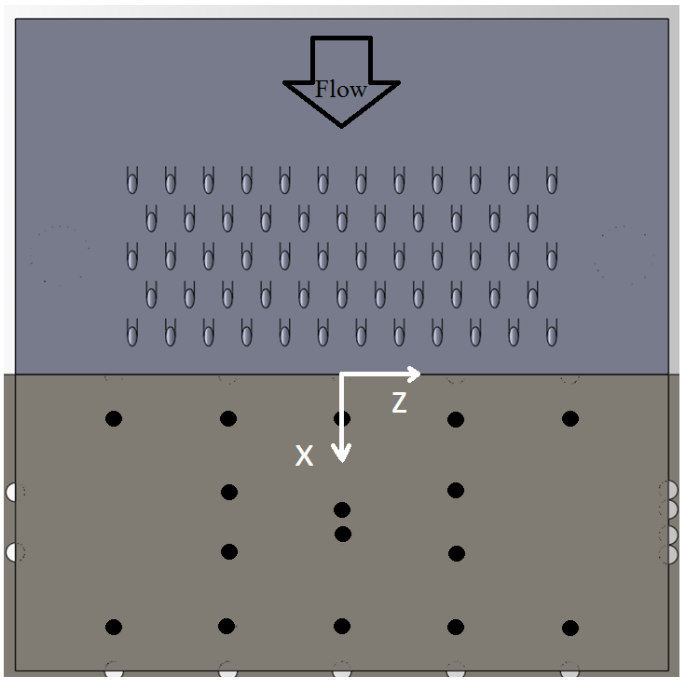

Figure 3.18: Spanwise Thermocouple Alignment with Injection Holes

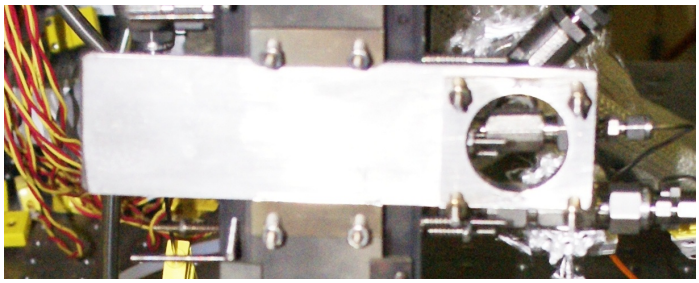

Figure 3.19: Sapphire Viewing Window

3.10 Repeatibility

3.10.1 Heat Flux Repeatibility.

Fourteen heat flux measurements were taken at repeatable flow conditions over the course of testing. These heat flux measurements were loaded into a Matlab routine to

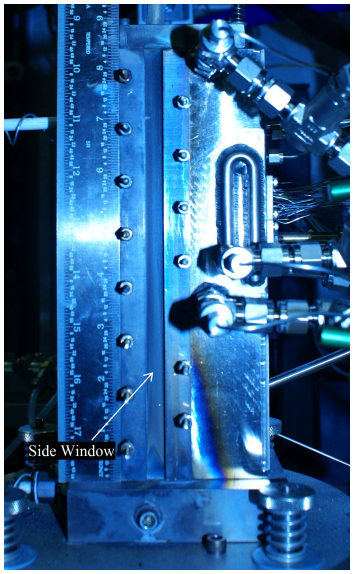

Figure 3.20: Fused silica side window

create a histogram and approximate a Gaussian distribution. The resulting 95% confidence interval is shown below in Table 3.2 for each thermocouple location. The results shown are a percentage of the mean heat flux measured at that location over the course of testing. As shown, some thermocouple locations showed widely variant behavior. As such, an effort to correct the heat flux for variations in the difference between the freestream and wall temperatures was conducted (see equation

This level of uncertainty in heat flux measurements was unacceptable. However, the data is largely presented in the form of augmentation (see equation 2.16). As such, a repeatability analysis on augmentation was performed.

3.10.2 Augmentation Repeatibility.

Each configuration had one data point tested at least twice, with $\phi = 1.175$ and $M = 2.0$. One measurement was collected during the blowing ratio sweep, and one was collected during the equivalence ratio sweep. The Single Row, Triple Row, Five Row, and Roll Forward configurations were all tested on multiple days. The difference in

Location	95% Confidence, Uncorrected	95 % Confidence, Corrected
1-1	16.0	19.8
1-2	18.4	21.4
1-3	22.8	30.1
1-4	22.5	15.6
1-5	25.9	37.5
2-2	45.5	50.3
2-3	16.8	15.9
2-4	28.5	34.5
3-2	66.8	71.2
3-3	11.0	14.1
3-4	43.0	42.3

Table 3.2: 95% Confidence Interval of Heat Flux at Location

percentage augmentation was calculated for each repeated data point. Statistical analysis of the resulting differences was then performed. The histogram of the initial calculation is shown in Figure 3.21. This calculation gave a 95% confidence interval in augmentation of 14.5%. This is unacceptable for the data. However, the data clearly shows higher probability clustered around a percentage difference of zero than the Gaussian distribution does. This indicates that the data has a tighter confidence interval than indicated by the normal distribution.

The experimental rig was designed in such a way that thermocouples in the instrumentation block could become dislodged if disturbed, throwing off the resulting heat flux calculation from that location. The author believes that the outliers in Figure 3.21 are likely a consequence of dislodged thermocouples. The data from the thermocouple locations generating the outliers was discounted for the applicable day of testing for all

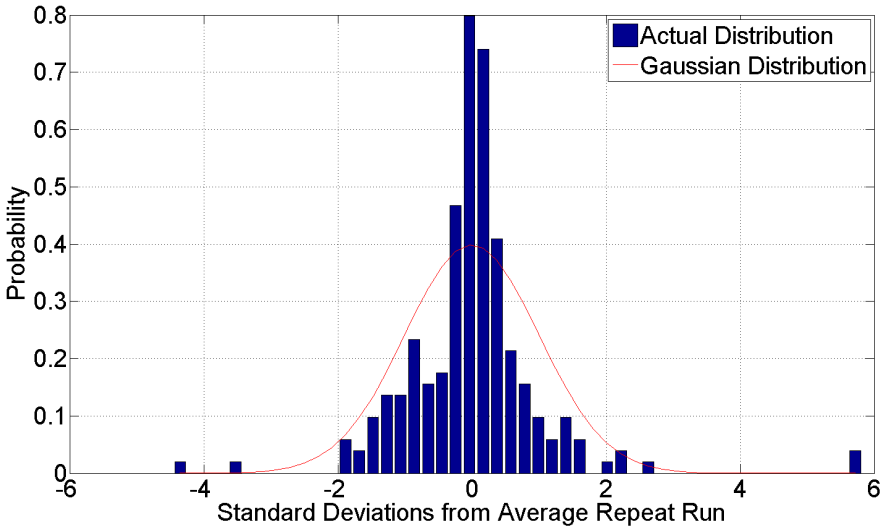

Figure 3.21: Histogram, differences in calculated augmentation between repeated runs

calculations. An outlier was considered to be a data point that showed greater than 4% difference from other repeat runs. Eighty-one data points were thus removed from the set of 220. No thermocouple locations at the fifteen diameter location showed sufficient repeatibility to be used for the Two Row Upstream configuration, and as such are not reported. The corresponding data points in all subsequent analysis were also removed. The resulting histogram and corresponding Gaussian distribution are shown in Figure 3.22. This data set predicted a 95% confidence interval that the difference in augmentation between repeat runs would be $-0.06 \pm 3.7\%$. This Gaussian distribution appears to fit the data set much better.

The resulting error bars on an augmentation plot appear like those shown in Figure 3.23.

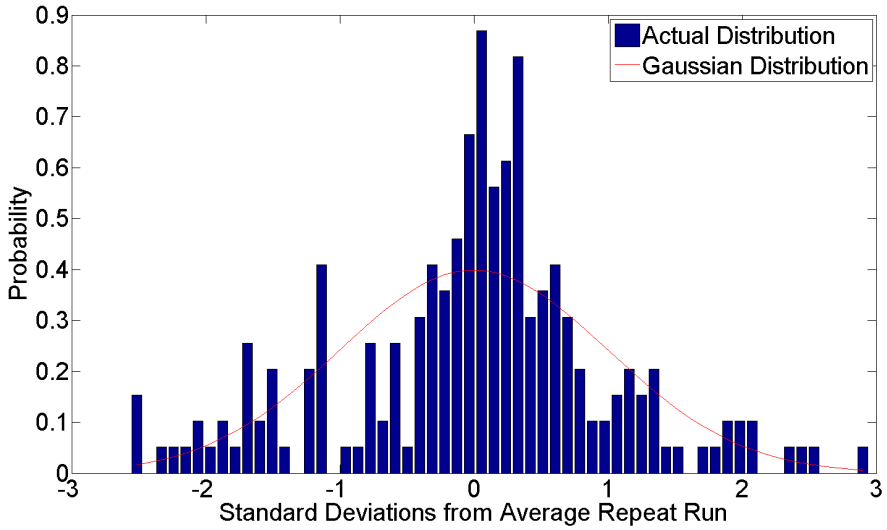

Figure 3.22: Histogram, differences in calculated augmentation between repeated runs

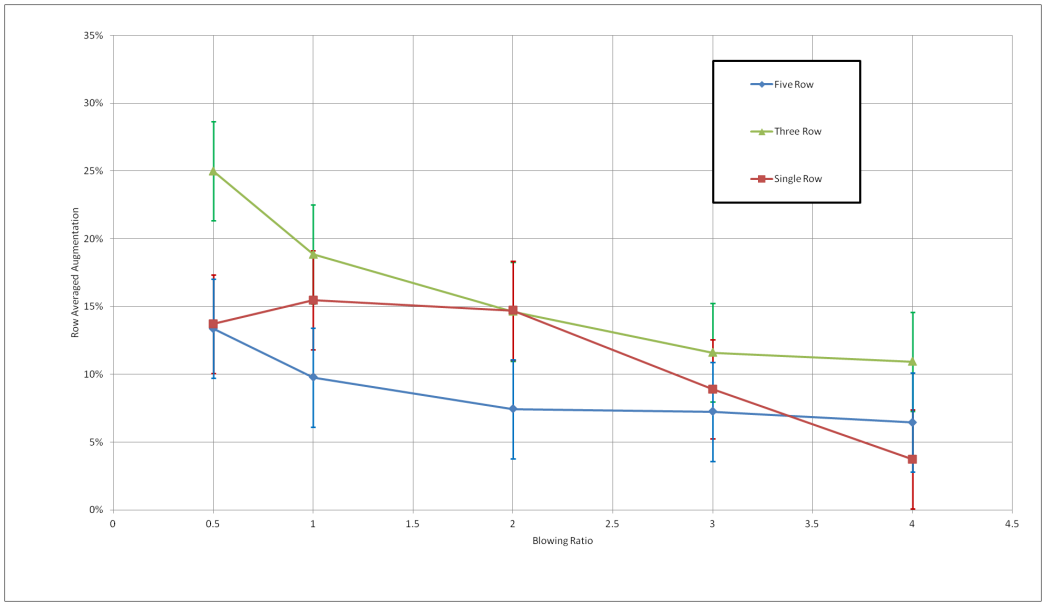

Figure 3.23: Augmentation results with error bars, blowing ratio sweep, Layer Buildup configurations, $\phi = 1.175$

IV. Results and Analysis

4.1 Test Plan

4.1.1 Initial Validation.

The initial phase of testing focused on validating the measurements of the test rig. Cooling hole geometry identical to the previously described Evans' Fan shaped cooling hole (see Figure 2.11) was implemented in the new rig and effective convective heat transfer coefficient measured at an equivalence ratio of $\phi = 0.6$. Heat transfer measurements were interpolated at a location 25D downstream of the cooling holes in order to directly compare the data of the current experimental rig to that obtained previously by DeLallo. Because the new WSR is of Inconel construction and actively cooled, different flow conditions are necessarily produced from the uncooled, ceramic reactor used by Evans and DeLallo (details in section 3.3). In order to produce an equivalent bulk velocity to Evans and DeLallo, the WSR was supplied 0.004 kg/s of air. However, the active reactor cooling dropped the temperature compared to the previous research, making it difficult to directly compare to results obtained with the ceramic reactor. As such, the initial testing included two blowing ratio sweeps. One used a 0.004 kg/s reactor air supply, in order to approximately match previous bulk velocities. The second used a maximum flow rate of 0.012 kg/s in order to match freestream temperature as closely as possible. The Inconel reactor was intentionally limited to 0.012 kg/s as a maximum in order to promote longevity of the ceramic transition section and flow straightener. The test matrix used is shown in Table F.1 in Appendix F. After testing it was determined that the high flow rate, high temperature flow conditions achieved results much closer to the work of Evans and DeLallo. Additionally, these conditions are more representative of actual gas turbines. As such, a 0.012 kg/s air supply to the WSR was adopted for the remainder of testing. This resulted in Re_{D_H}=6261, as discussed in section 3.2.

4.1.2 Test Campaigns.

The "Layer Buildup" Campaign consisted of testing the Single Row, Triple Row, and Five Row configurations described in 3.7.3. The purpose of these designs was to fulfill the thesis objectives by testing the feasibility of building a "thick" attached coolant layer. The researcher hypothesized that this strategy would allow a non-reacting protective layer to remain intact for some distance under the a mixing and burning layer. This outcome would fulfill the objective of creating a film cooling scheme for use in a high fuel-air ratio environment. Each configuration was tested at a range of blowing ratios from 0.5 to 4. Air coolant was injected at each blowing ratio to test the performance of a reacting case. Diatomic nitrogen was also injected at each test point in order to provide a non-reacting performance comparison. Details are shown in Table F.2 in Appendix F. The reader should note that holding M constant leads to higher mass flow in configurations populated by more holes. Typical blowing ratios found in industry range from 0 to 2 (higher can result in coolant separation). The current testing went as high as four to examine effects associated with fulfilling the thesis objective of consuming radicals away from the wall. Higher blowing ratios caused separation, which led to increased vorticity and mixing. This enhanced burn rates and helped radical consumption. The blowing ratio sweeps were all performed at ϕ of 1.175 (see Appendix D for explanation). Visible spectrum photographs were taken at each blowing ratio in order to provide qualitative understanding of the flame physics. A side view through the fused silica window was used, the shutter speed was set at 1/20th of a second and the aperture was set to f/5.6 for all photos.

Each configuration was also tested at a range of ϕ from 1.1 to 1.4. The associated test matrix is shown in Table F.3 in Appendix F. A blowing ratio of 2 was selected for these sweeps in order to provide a test point that was applicable to turbine and fuel-rich streaks as well as the UCC. This created a "crux" test point with a blowing ratio of 2 and a ϕ of 1.175 that was performed twice for each configuration: once for the M sweep, and once for

the ϕ sweep. Visible spectrum photographs were taken at different equivalence ratios at the same camera settings as those taken for the blowing ratio sweep.

The "Enhanced Mixing" Test Campaign evaluated the Roll Forward, One Row Upstream, and Two Row Upstream configurations described in Section 3.7.4. This campaign was conducted in order to evaluate the efficacy of these configurations at consuming radicals away from the wall while protecting it. This test campaign followed test matrices identical to those of the Layer Buildup Campaign (shown in Tables F.2 and F.3).

4.2 Comparison to Previous Results

The heat flux and augmentation results obtained from the Evans Fan configuration (described in Section 3.7.1), interpolated to the 25 diameter location are shown in Table 4.1. All q" is shown in $\frac{W}{m^2}$. All testing was performed at $\phi = 1.3$ for DeLallo's cases. The new rig cases were all performed at $\phi = 1.175$. For a definition of augmentation (σ) and explanation of its use as a metric, refer to section 2.5.2. The initial run of testing supplied 0.004 kg/s of air to the WSR in order to approximately match flow rates to DeLallo's testing. As the tables show, these results do not compare well. DeLallo usually achieved a freestream temperature with the ceramic WSR of approximately 1760 K [7]. At this condition, the freestream temperature of the new Inconel® rig was measured much lower than this at 1371 K. The lower driving temperature resulted in much lower heat transfer to the block, weaker reactions, and corresponding lower augmentation.

The results of running 0.012 kg/s supply to the WSR are shown below in Table 4.2. At the 0.012 kg/s condition, the new reactor obtained a freestream temperature of 1704 K. It was decided not to push the flow rate any higher due to durability concerns of the ceramic transition and flow straightener components. These results compared much better to those of DeLallo's, staying within 15% for heat flux and augmentation, in spite of running at

Coolant	N_2, $M = 1$	N_2, $M = 2$	Air, $M = 1$	Air, $M = 2$	$M = 1$	$M = 2$
	q''	q''	q''	q''	σ	σ
DeLallo	75901	77468	87690	92142	10.63	15.15
New rig, 0.004 kg/s supply	28189	28232	28311	29257	0.39	5.58
Percent Difference	64.7	66.7	68.1	69.2	96.7	58.1

Table 4.1: Comparison of DeLallo results to new experimental rig results, matching bulk velocity

slightly different equivalence ratios. As such, the measurements of the new test rig were considered to be validated with respect to prior research. Because of the comparability of these results as well as the more industry representative freestream temperature, 0.012 kg/s air supply to the WSR was adopted as a constant for all subsequent testing.

Coolant	N_2, $M = 1$	N_2, $M = 2$	Air, $M = 1$	Air, $M = 2$	$M = 1$	$M = 2$
	q''	q''	q''	q''	σ	σ
DeLallo	75901	77468	87690	92142	10.63	15.15
New rig, 0.012 kg/s supply	79873	84807	88792	95105	11.83	13.33
Percent Difference	5.2	9.5	1.3	3.2	11.3	12.0

Table 4.2: Comparison of DeLallo results to new experimental rig results, matching temperature

4.3 Surface Temperature Uniformity

A key problem in the work of Evans and DeLallo had been spanwise non-uniformity due to swirl in the flow from the WSR. While this problem was largely mitigated by Bohan with the addition of a flow straightener [5], the author desired to examine the surface

uniformity of the new rig to preempt any issues. Wall temperatures were calculated using the process described in Appendix A. The Single Row configuration's surface temperature distribution at the crux test point is shown in Figure 4.1.

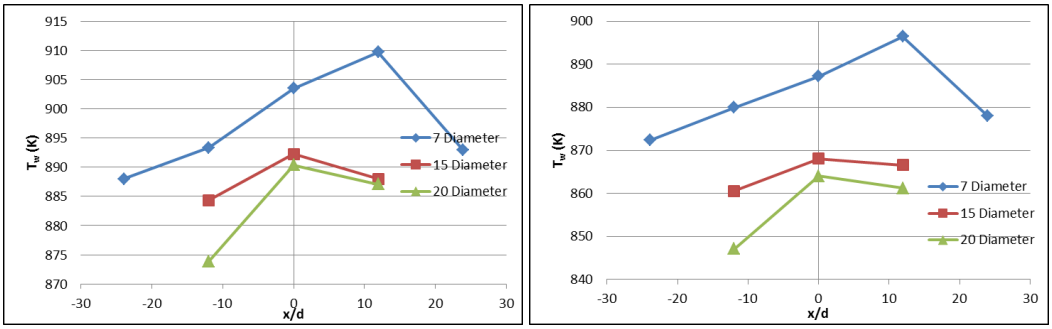

Figure 4.1: T_w, Single Row, ϕ = 1.175, M=2, Left: Air Coolant, Right: N_2 Coolant

As shown, the Single Row configuration demonstrated variation of up to 22 K in the 7D location (2% variation). The 15D location showed 8 K of variation, and the 20D location showed up to 16 K of variation. This is acceptable uniformity in the author's judgement, and was most likely aided by lateral conductive heat transfer. Hastelloy-X® has a thermal conductivity in excess of $20\frac{W}{m-K}$ in the temperature range of interest (see Appendix A). A preliminary analysis of the heat transfer in the block was conducted in order to promote one-dimensionality, and is detailed in Appendix B. In spite of the promising results of the analysis, research experience shows that multi-dimensional heat transfer did occur in the instrumentation block due to streamwise gradients in surface temperature. Future researchers may wish to conduct more in-depth analysis of the effect of cold-side convection cooling on heat transfer in the block to promote one dimensionality. The temperature gradient disallowed direct comparison of heat flux from the 7D location to the 15D and 20D locations. It also prevented the use of data from the 27D row of thermocouples entirely, as the uncertainty was too high. The front to back increase in temperature is consistent for all test points. The researcher hypothesizes that the streamwise

temperature gradient may be caused by the manner in which the cold-side convection cooling with heated oil was implemented (see Figure 3.6). For comparison, the Triple Row configuration uniformity is shown in Figure 4.2. The Triple Row configuration shows even better spanwise uniformity, varying less than 10 K spanwise. The researcher speculates that this is due to the increased mass flow of cooling improving the spanwise uniformity of coolant on the surface. The reactions induced by the coolant would therefore also be more even. Also, the reactions are starting closer to the 7D location, suggesting that lateral conduction to the outboard thermocouples might be improving the uniformity.

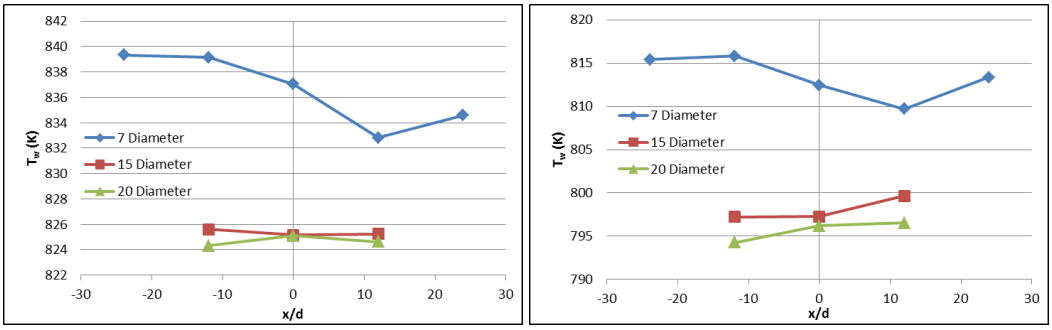

Figure 4.2: T_w, Triple Row, ϕ = 1.175, M=2, Left: Air Coolant, Right: N_2 Coolant

The Five Row configuration is shown in Figure 4.3. The Five Row also demonstrated excellent results, varying less than 10 K spanwise. The outboard thermocouple locations show higher surface temperatures. They lie 2 diameters outboard of the spanwise coordinate of the outermost injection holes and do not recieve full coolant coverage. The fact that the temperatures are higher on the outboard locations for this configuration, but were not for the Single Row and Triple Row indicates that the Five Row is lowering wall temperature from what it would be otherwise. Overall the surface temperature distributions were promising, and showed that freestream swirl had minimal impact on the results.

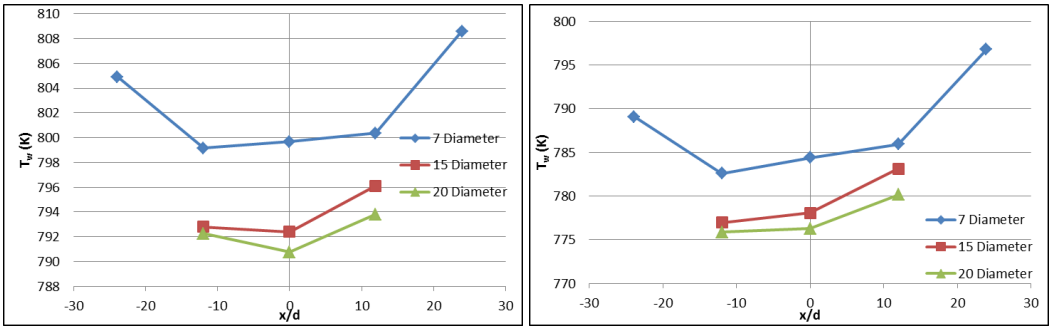

Figure 4.3: T_w, Five Row, ϕ = 1.175, M=2, Left: Air Coolant, Right: N_2 Coolant

4.4 Layer Buildup Performance

4.4.1 Blowing Ratio Sweep.

The comparative results of the Layer Buildup Campaign blowing ratio sweeps are shown in Figures 4.4, 4.5, and 4.6. As shown, the blowing ratio, M, was varied from 0.5 to 4.0. The augmentations (see equation 2.16) shown are the averages of the row of thermocouples at a streamwise coordinate. The fifteen and twenty diameter charts average thermocouples located at 14 and 16, or 19 and 21 diameters respectively (see Table 3.1 for details). Figure 4.4 shows the results at seven diameters downstream of initial injection. The Single Row configuration clearly shows evidence that no reactions are occurring at this location by demonstrating negative heat flux augmentation at all blowing ratios. The negative augmentation is an unintuitive result suggesting that air cooled the wall better at this location than nitrogen. This phenomenon is discussed in detail in section 4.6. However the Triple Row configuration begins showing evidence of augmentation (and therefore reactions) because its initial injection row of holes is located eight diameters further upstream from the measurement location than the Single Row. The Five Row configuration continues this pattern, showing the highest consistent augmentation of the three at this location. The blowing ratio has no effect on the augmentation of the Single Row configuration because no flame is occurring at this location. As the blowing ratio increases,

the Triple Row configuration shows consistently increasing heat flux. As the mass flow of air increases, this configuration is failing to protect the wall from the increasing chemical potential heat energy being released. The Five Row configuration also shows increasing augmentation as mass flow increases, but to a lesser degree. As such, the Five Row configuration is beginning to protect the wall from the effects of the flame.

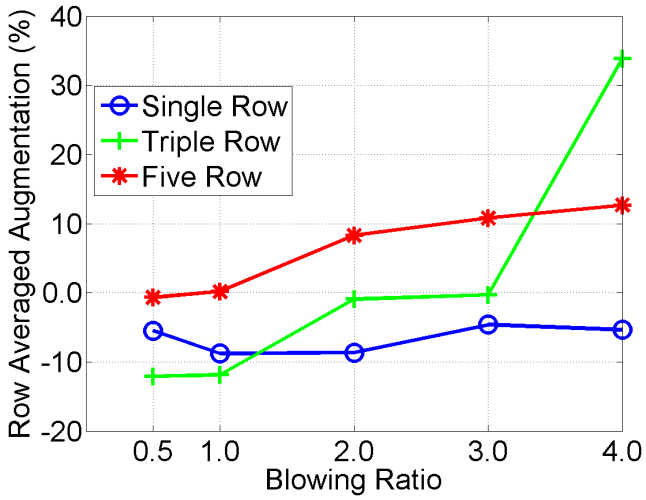

Figure 4.4: Augmentation (σ) vs. M, Three Configurations, Seven Diameters Downstream of Injection

Moving downstream to the fifteen diameter location (shown in Figure 4.5), reactions and augmented heat flux have begun in earnest for all configurations. The Five Row configuration shows the best consistent performance, showing augmentation close to five percent from blowing ratios of one to four. Interestingly, the Triple Row configuration demonstrates worse augmentation performance than the Single Row. The greater mass flow injection of the Triple Row configuration at a given blowing ratio directly translates to greater heat release potential due to chemical reactions. Because the coolant layer is not yet sufficiently thick to provide a non-reacting layer, the configuration performs worse.

The second row of injection holes in the Triple Row configuration is also offset spanwise from the first and third rows. As such, this row is unprotected from freestream radicals by an upstream row. This pattern demonstrates that the Five Row configuration is performing sufficiently well to both consume more fuel and protect the surface of interest, fulfilling a key objective of this thesis. This confirms a pattern shown in non-reactive film cooling discussed in section 2.4.

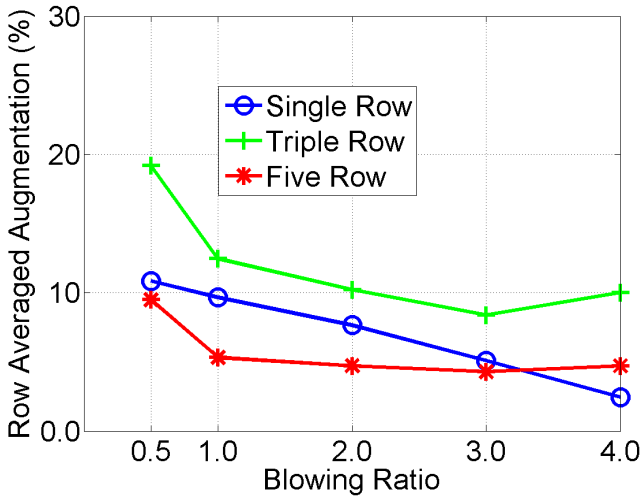

Figure 4.5: σ vs. M, Three Configurations, Fifteen Diameters Downstream of Injection

The trends seen at fifteen diameters continue at the twenty diameter location, as shown in Figure 4.6. The Single Row configuration begins to approach zero with increasing blowing ratio, indicating possible detachment of the flow. The Three Row mirrors the trend of dropping augmentation, but begins leveling out at higher blowing ratios. The author believes this reflects sufficient mass injection to begin protecting the wall, as the pattern appears much like that of the Five Row configuration. When compared to the fifteen diameter location, the Five Row trend looks very similar, but at slightly higher

augmentation levels. This is probably due to gradual increase in coolant layer temperature as diffusion and burning occur moving downstream.

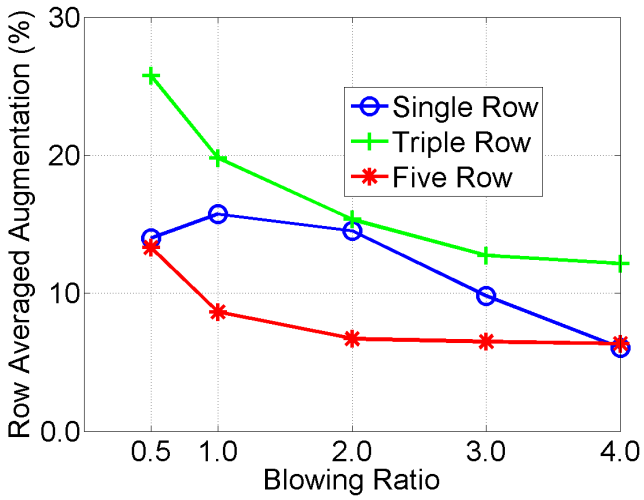

Figure 4.6: σ vs. M, Three Configurations, Twenty Diameters Downstream of Injection

4.4.2 Equivalence Ratio Sweep.

The results of the Layer Buildup Campaign's ϕ sweeps are shown in Figures 4.7, 4.9, and 4.10. Again, the row-averaged augmentation results are presented. Figure 4.7 shows the results seven diameters downstream of trailing injection. The Single Row and Triple Row configurations both show negative augmentation at this location, decreasing with increasing ϕ. This implies again that the air was a more effective coolant than the non-reacting N_2, an effect explained in section 4.6. The Five Row configuration shows an increase followed by a decrease in augmentation. Differences in freestream radical concentration would create differences in local equivalence ratio at the measurement location, which may increase or decrease the ignition time and spreading rate of the flame.

Moving to the fifteen diameter location, evidence of reactions in all cases appears, as shown in 4.7. The Single Row configuration augmentation decreases at the highest ϕ,

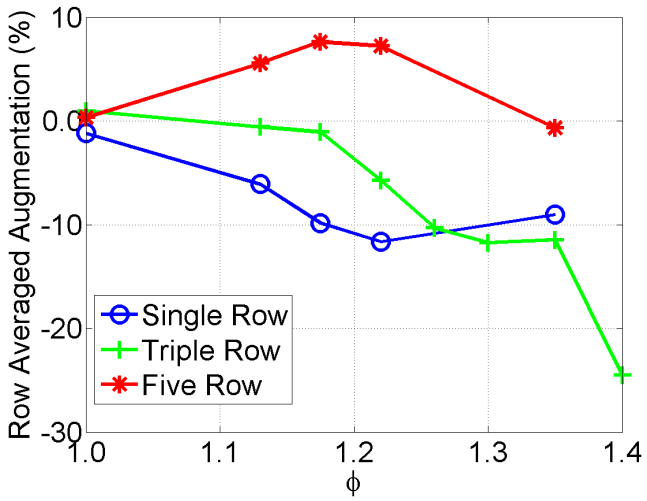

Figure 4.7: σ vs. ϕ, Three Configurations, Seven Diameters Downstream of Injection

suggesting that its supply of fresh oxygen is beginning to be consumed more fully. Looking at the Single Row's $\phi = 1.35$ test point in Figures 4.7, 4.9, and 4.10, the augmentation does consistently increase going downstream. An explanation is that the flame is burning over this entire distance, increasing the local gas temperature more and more as the flow moves downstream. Figure 4.8 shows an enhanced-blue value visible spectrum photograph of the flame created by the Single Row configuration at a blowing ratio of 2.0. As shown, the flame appears to be burning at high strength over the 20D location and beyond.

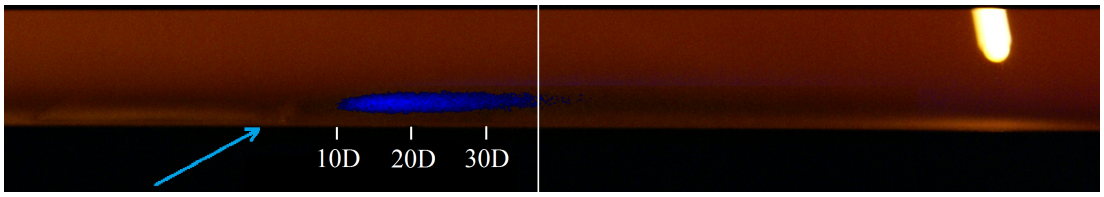

Figure 4.8: Single Row Configuration Photo, Blue Values enhanced ϕ=1.175, M=2.0

The Triple Row and Five Row configurations both demonstrate increasing augmentation all the way to the highest equivalence ratio tested. This demonstrates that local equiv-

alence ratios are still approaching their highest flame-generating potential as they increase over the range tested.

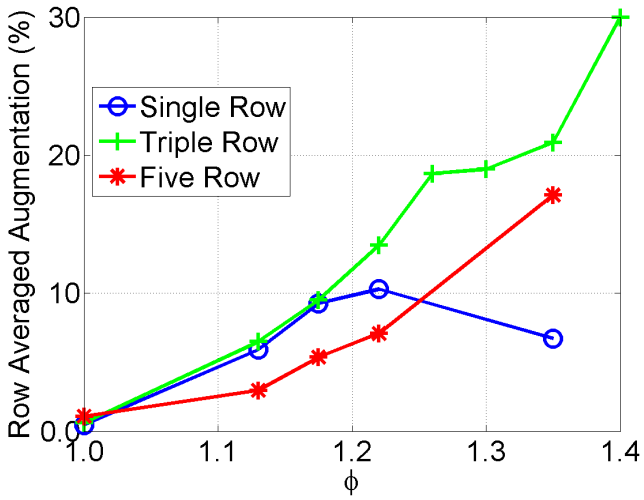

Figure 4.9: σ vs. ϕ, Three Configurations, Fifteen Diameters Downstream of Injection

At the twenty diameter location, similar trends are visible. All configurations have increased augmentation over the fifteen diameter location. The Single Row augmentation appears to be leveling off at the $\phi = 1.35$ test point, indicating perhaps that the flame will begin lowering in temperature with increasing ϕ due to local rich conditions in the injected coolant. The Triple Row and Five Row augmentations both increase through the highest equivalence ratio tested, indicating that a local maximum of potential heat release has still not been reached. The Five Row configuration does consistently show lower augmentation than the Triple Row. While the greater mass flow of the Five Row does give the flow greater chemical potential for heat release, the configuration is providing a much better buffer layer between the reactions and the flow.

Overall, the Five Row configuration demonstrated the best consistent low augmentation performance over a range of blowing ratios and equivalence ratios. It showed that a

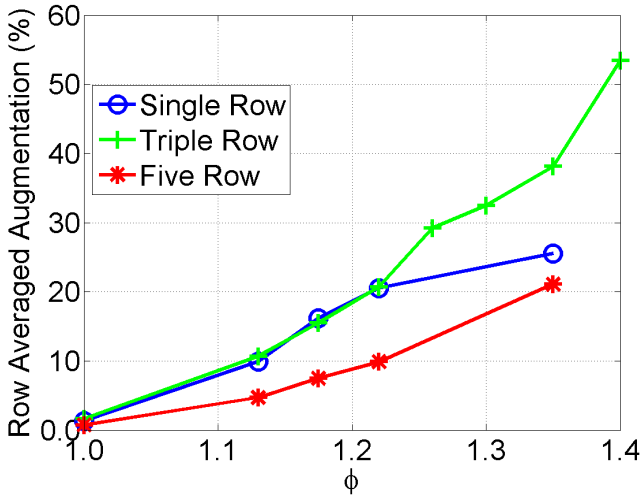

Figure 4.10: σ vs. ϕ, Three Configurations, Twenty Diameters Downstream of Injection

low-reactive coolant layer can be established in a fuel-rich environment with sufficient rows of injection, fulfilling the major objective of this thesis. However, the continued increase in augmentation as ϕ increased demonstrated the need for further improvement for use in higher fuel-air environments. This might be accomplished either with additional rows of coolant or upstream radical consumption schemes designed to lower the equivalence ratio near the wall.

4.4.3 Flame Visualization.

Photographs of the flames produced by the Triple Row and Five Row configurations are shown in Figure 4.11. All photographs shown were taken with a shutter speed of 1/20th of a second, and an aperture of f/5.6. The photos were calibrated by means described in section 3.9. While the visible spectrum does not provide detailed information about the reactions, it does inform as to where they are occurring. The opposite wall is a strip of Inconel that was inserted into the slot intended for another side window. Replacing the opposite window with metal enabled greater photograph contrast. The opposite wall is visible in the photographs radiating orange. The Five Row photo is notable for showing an

orange layer below the blue flame, indicating that the opposite wall radiation is visible. The Triple Row does not show this layer, indicating a blue-violet reaction zone completely to the wall. In conjunction with the quantitative results, the author believes that this demonstrates a configuration that has created a non-reacting coolant layer on the surface, creating a stand-off distance between the wall and the flame, fulfilling a major research objective. The flame penetration into the flow is also shown, where the Five Row configuration obtained a slightly higher penetration of 7.7 diameters. High flow penetration is desirable to help attain a higher degree of radical consumption in the flow in support of the thesis objectives.

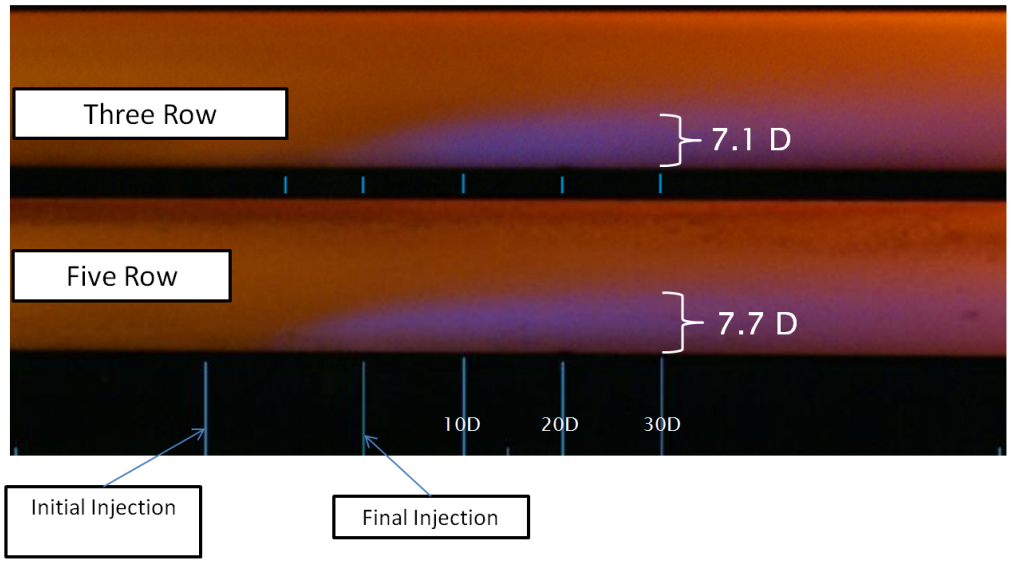

Figure 4.11: Flame Visualization (Visible Spectrum), Triple Row and Five Row Configurations, ϕ = 1.175, M=2.0

4.5 Enhanced Mixing Performance

The Enhanced Mixing Campaign schemes universally produced higher augmentation than the Five Row configuration of the Layer Buildup Campaign. The One Row Upstream, Two Row Upstream, and Roll Forward configurations had four, five, and five rows of

injection holes respectively. Because some of the coolant was being committed to full separation, mixing, and radical consumption, these configurations could not build the same type of coolant layer as the Five Row configuration. The One Row Upstream and Two Row Upstream configurations both had three rows of coolant injection at 30° . As such, the Triple Row configuration is included in the following charts for comparison, because it commits a similar amount of coolant to be attached to the wall.

4.5.1 Blowing Ratio Sweep.

The seven diameter augmentation performance of the Enhanced Mixing schemes at a range of blowing ratios is shown in Figure 4.12. As shown, all three enhanced mixing schemes have begun reacting at this point. This is a promising result showing more rapid radical consumption of the enhanced mixing schemes. They produce higher augmentation than the Five Row configuration, and are consistently much worse than the Triple Row configuration. However, the Roll Forward configuration follows the trends of the Five Row configuration closely and remains within 5% of its augmentation values until a blowing ratio of four is reached. The Two Row Upstream configuration shows very little increase in augmentation with blowing ratio, which has promising implications for the ability of this configuration to consume radicals without harming the wall.

At the fifteen diameter location, all configurations are reacting. The Two Row Upstream results are not shown due to repeatability concerns, as discussed in section 3.10. The One Row Upstream configuration performs worse than the Three Row configuration. This result is interesting the upstream injection scheme injects three rows of coolant (identical in geometry to the Triple Row configuration) downstream of its counterflow-injection rows. This result suggests that the counterflow injection is somehow disturbing the film cooling action further downstream. The Roll Forward configuration outperforms the Triple Row, however, and maintains less than 10% augmentation throughout the blowing ratio range. The Roll Forward performs only marginally worse than the Five Row

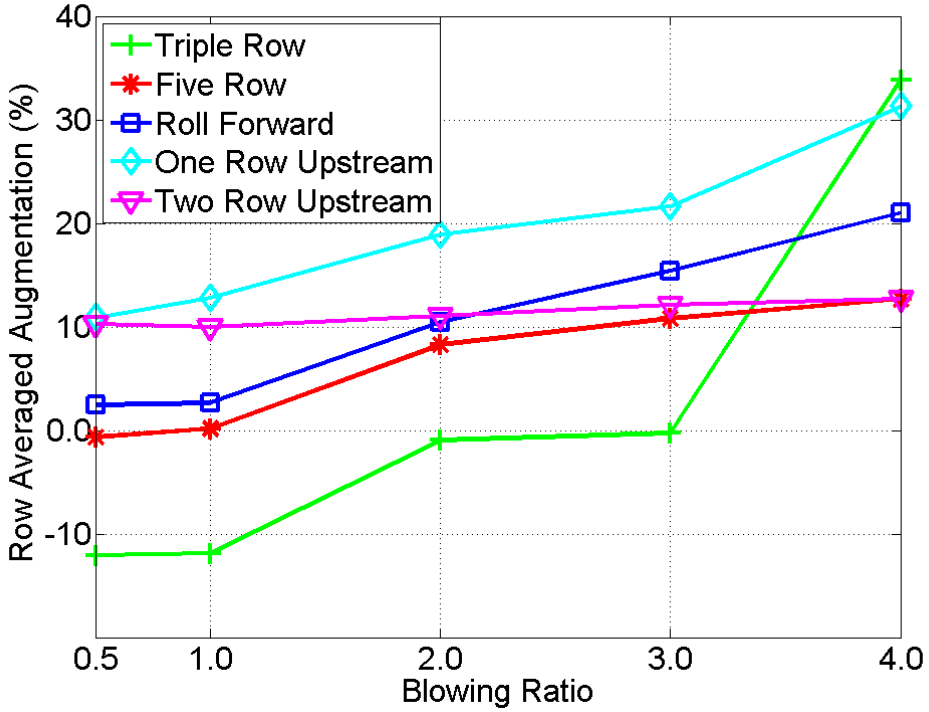

Figure 4.12: σ vs. M, Five Configurations, Seven Diameters Downstream of Injection

configuration, which is a promising result for the potential benefits of enhanced mixing schemes.

At the twenty diameter location, the One Row Upstream and Two Upstream begin to outperform the Triple Row at low blowing ratios. The Two Row Upstream configuration again shows little change in augmentation with blowing ratio, indicating increased radical consumption with few consequences. Another interesting behavior is the Roll Forward configuration's increase in augmentation with blowing ratio, which diverges from the decreasing pattern of the Five Row. This suggests that the separation effects of the high blowing ratio begin to take a toll in performance further downstream.

Overall the Roll Forward configuration demonstrated the lowest augmentation performance of the enhanced mixing schemes over the blowing ratios tested, and was very

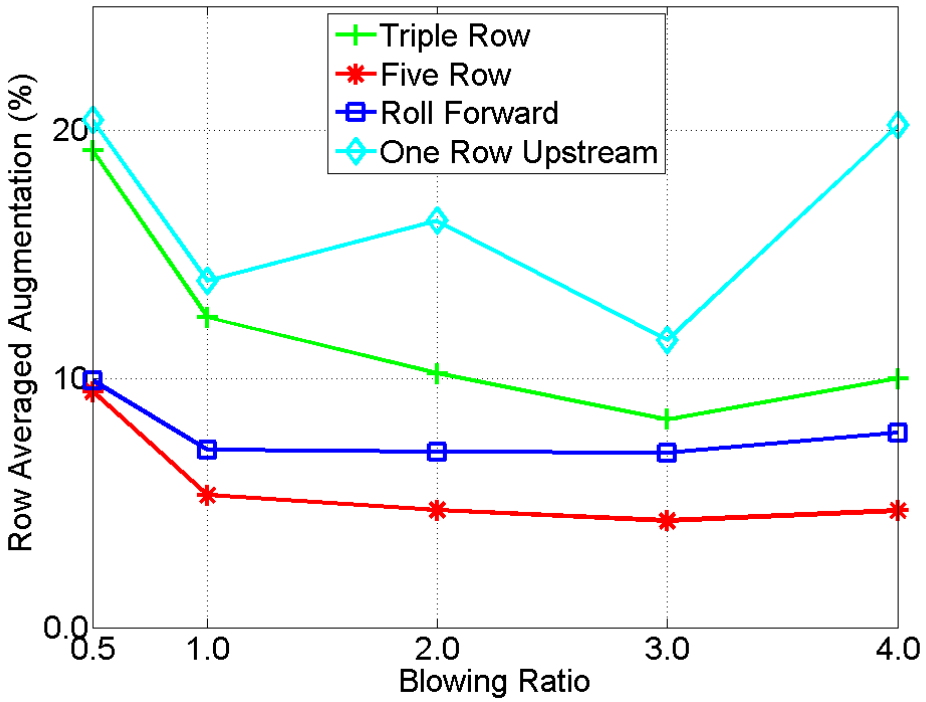

Figure 4.13: σ vs. M, Five Configurations, Fifteen Diameters Downstream of Injection

comparable to the Five Row performance. Future iterations of this type of scheme must take care at higher blowing ratios. The One and Two Row Upstream configurations produced relatively high augmentations at most blowing ratios, and as such did not completely fulfill the thesis objective of wall protection. However, the high augmentation implies the One Row Upstream and Two Row Upstream configurations created more rapid radical consumption than other schemes. A new performance metric for reactive film cooling is needed to account for this performance, and is discussed in section 4.7.

4.5.2 Equivalence Ratio Sweep.

The augmentation performance of the enhanced mixing schemes over a range of ϕ was largely promising. At the seven diameter location, shown in Figure 4.15, all three enhanced mixing configurations show higher augmentation than the Triple Row and Five

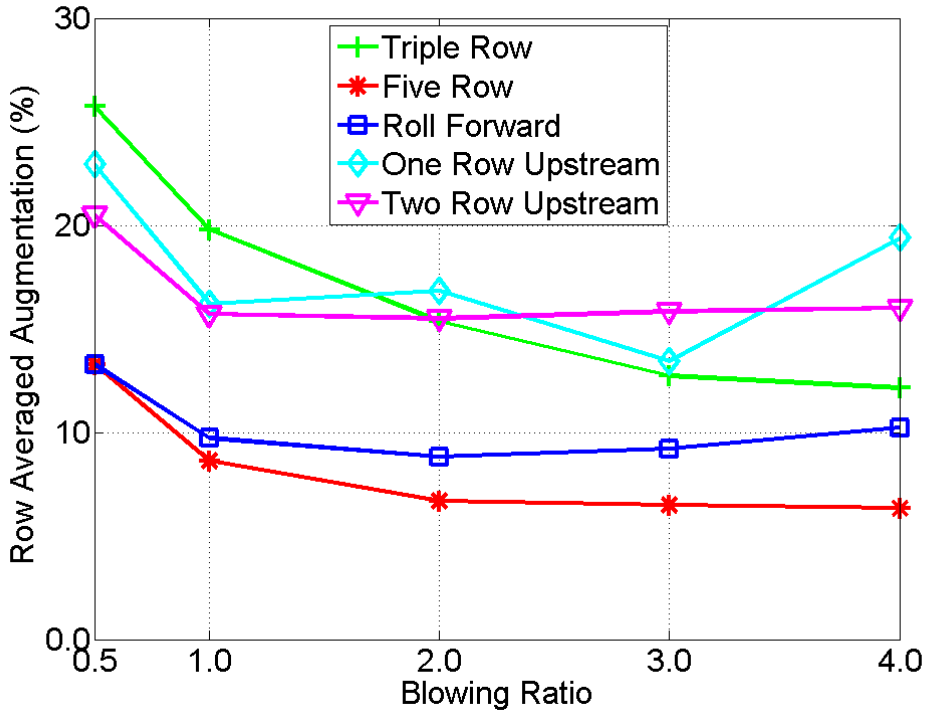

Figure 4.14: σ vs. M, Five Configurations, Twenty Diameters Downstream of Injection

Row. This result at the seven diameter location was expected, as a major objective of the enhanced mixing schemes was to consume radicals further upstream.

At the fifteen diameter location, the Roll Forward again performs the best of the enhanced mixing schemes, with augmentation performance between that of the Triple Row and Five Row configurations. The high slope of the One Row Upstream configuration does have promising implications for radical consumption. This trend does indicate higher heat flux augmentation at a range of ϕ, which is bad for wall protection. However, the One Row Upstream is producing greater increases in heat flux than the Five Row and Roll Forward configurations while injecting less mass flow. The chemical potential of the coolant is correspondingly lower. The lower chemical potential in conjunction with the higher rise

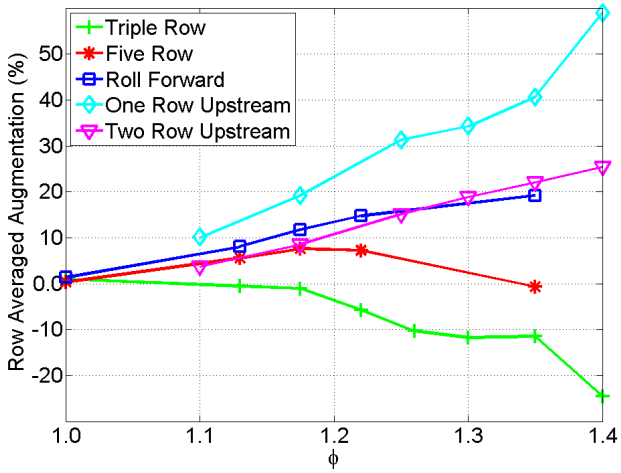

Figure 4.15: σ vs. ϕ, Five Configurations, Seven Diameters Downstream of Injection

in augmentation suggests that the One Row Upstream configuration is consuming radicals further upstream than the other configurations, fulfilling the related thesis objective.

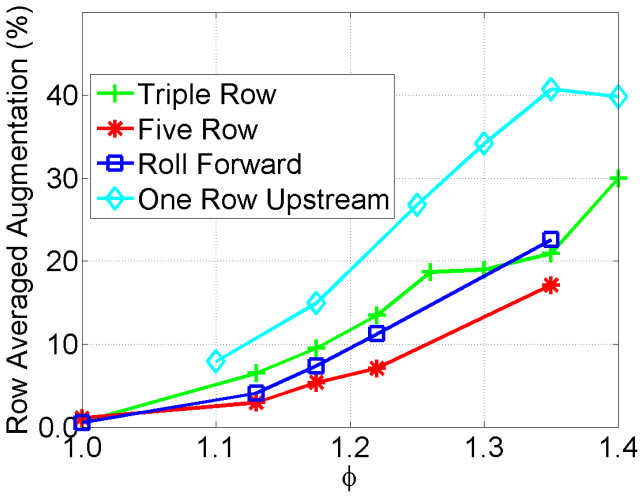

Figure 4.16: σ vs. ϕ, Five Configurations, Fifteen Diameters Downstream of Injection

At the twenty diameter location, shown in Figure 4.17, more interesting trends appear. The One Row Upstream configuration shows approximately equal augmentation to the Three Row configuration. As such, more mass flow is being injected and more radicals are being consumed for little or no increase in heat flux. The Two Row Upstream configuration shows lower augmentation than the Three Row, indicating a further increase in radical consumption and a concurrent increase in wall protection. The Roll Forward configuration continues its trend of producing slightly higher augmentations than the Five Row configuration.

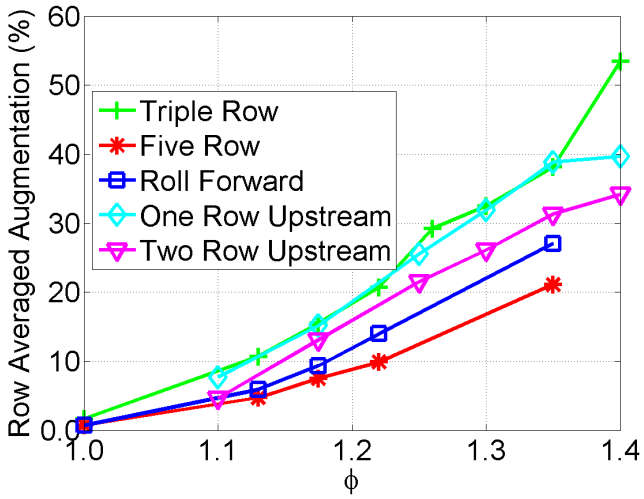

Figure 4.17: σ vs. ϕ, Five Configurations, Twenty Diameters Downstream of Injection

Overall the Roll Forward configuration demonstrated good ability to maintain cooling properties for the wall in an enhanced mixing configuration. The One and Two Row Upstream configurations significantly increased the heat flux to the wall. While bad for wall protection, this does demonstrate a possible path forward for rapid radical consumption.

4.5.3 Flame Visualization.

Photographs were taken at the same settings and location as those for the Layer Buildup campaign (described in Section 4.1.2). The photographs taken at the M=4.0 test point are shown below in Figure 4.18. The enhanced mixing schemes as a group demonstrate the highest-penetration flames observed in the current research. The One Row and Two Row Upstream configurations show very unique flame structures. The Two Row Upstream configuration appears to stop producing a strong flame after the ten diameter downstream location, although side window coking makes it difficult to judge. The flame in both instances is very separated from the surface, offering an explanation for these configurations' shortcomings in wall protection. The upstream injection likely created vortices off of the wall, similar to those shown in section 2.4. These vortices could have entrained the downstream coolant off of the wall completely, and conveyed hot, freshly reacted gases to it. The Roll Forward photograph shows distinct flames forming at the injection location of each row of holes. Reactions in the Roll Forward photograph are still occurring at the injection point of the second and third rows as the flow moves downstream, indicating that radicals are still reaching these locations. However, the two downstream rows are not reacting immediately upon injection, suggesting that the near-wall radicals have been consumed. The Roll Forward configuration has therefore successfully consumed near wall radicals before creating a protective coolant layer, fulfilling the thesis objectives. All three enhanced mixing schemes achieved high flow penetration. The 11.1 diameter penetration of the One Row Upstream and Roll Forward configurations was a 44% increase from the Five Row penetration. The Two Row Upstream configuration achieved a 55% increase in penetration over the Five Row configuration.

The enhanced mixing schemes all demonstrate excellent flow penetration and radical consumption, fulfilling a major thesis objective. The Roll Forward configuration

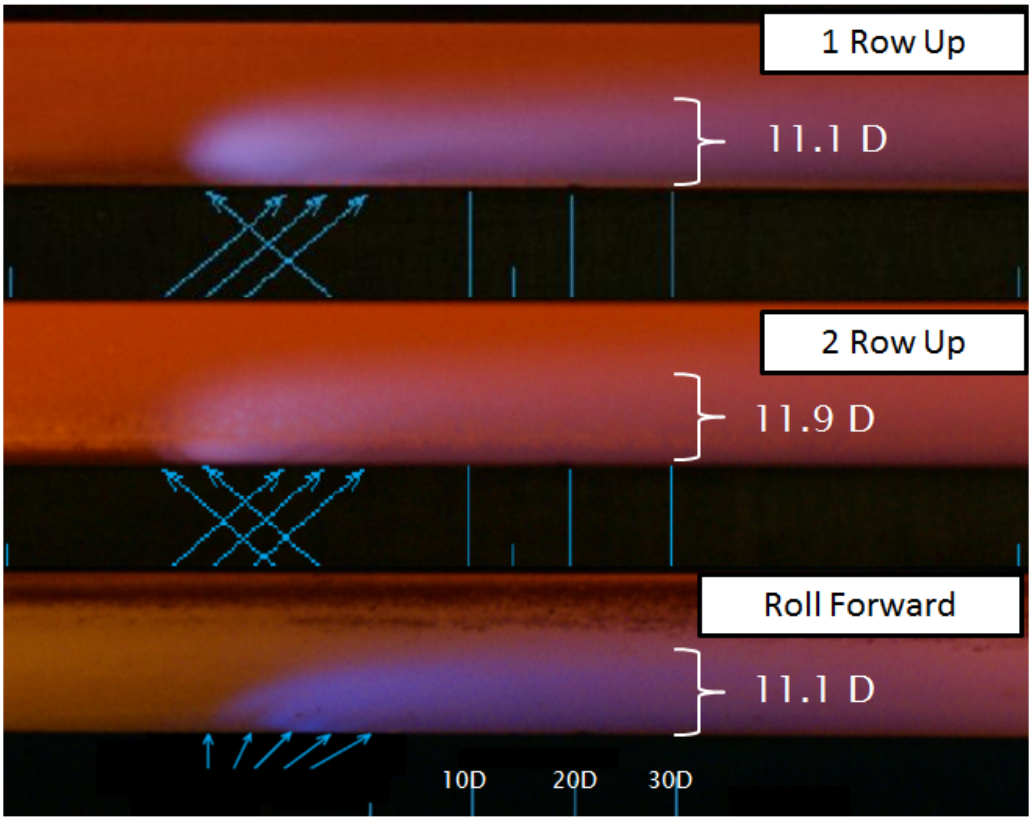

Figure 4.18: Flame Visualization (Visible Spectrum), One Row Upstream, Two Row Upstream, and Roll Forward Configurations

demonstrates the ability to combine consumption with wall protection, providing a clear step forward in the study of fuel-rich film cooling.

4.6 Wall Temperature Study

A brief study of the effect of wall temperature on heat flux was conducted in order to better quantify the physics involved. The study was conducted on the Triple Row cooling configuration, selected as a good ”average” configuration to examine. As with all other testing in this thesis, Mokon oil was supplied to the cold side cooling loops. However, the input oil temperature was varied from 225 to 400° C in order to vary wall temperature. Testing followed the plan detailed in Table F.4 in Appendix F.

The findings at seven diameters downstream of injection are shown in Figure 4.19. The data implies that reactions are not occurring at this location. Over the range of cold-side coolant temperatures tested, the wall temperatures in this region do not overlap for the air coolant and nitrogen coolant cases. This is probably due to conductive heating from reactions occurring further downstream in the air-cooled case. As might be expected in this case, the air coolant and nitrogen coolant cases are both relatively linear, and line up fairly well. This chart offers an explanation for the negative augmentations seen for several configurations at this location. Because the air is behaving as a non-reacting fluid, but the wall temperature is higher due to conduction from downstream, the heat flux is lower as a natural consequence of the linear relationship shown in Equation 2.4. Lower heat flux in the air case versus the nitrogen case results in a negative augmentation. As we move on to the 15 diameter location, evidence of reactions occurring appears, as shown in Figure 4.20.

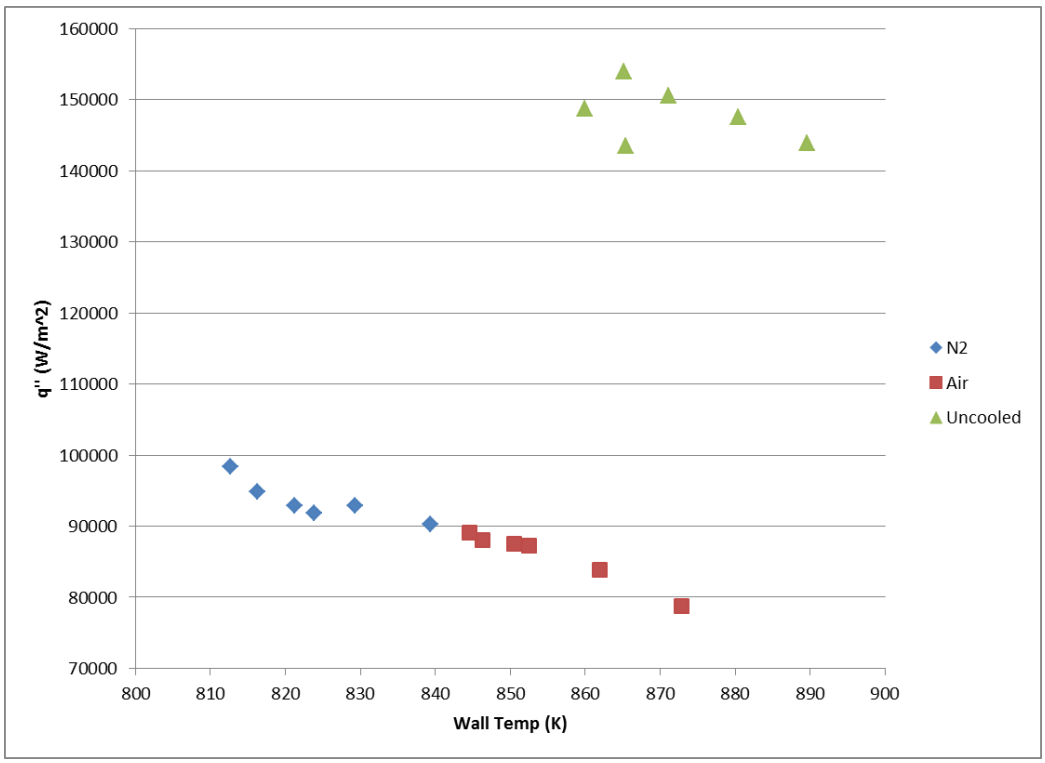

Figure 4.19: q" vs. T_w, Triple Row, $M = 2$, seven diameters downstream of injection

The N2 data shows high variability compared to that of the uncooled and air-cooled test points. All data was taken at a blowing ratio of 2.0. This is typically as high a blowing ratio as traditional film cooling will produce, because going any higher generally results in seperation. There are three N_2 data points that seem to have a linear relationship at lower heat fluxes, and three that appear to correlate at higher heat fluxes. The higher points also demonstrate a steeper slope, which is directly related to a higher convective heat transfer coefficient. In light of this evidence, the author hypothesizes that the coolant has detached from the wall in the higher heat flux cases, demonstrating instability at this blowing ratio. The air cooling shows a very linear relationship over the range tested until the highest wall temperature, where it begins to curve up. This is consistent with the non-linear trends shown previously by Greiner et. al. [10].

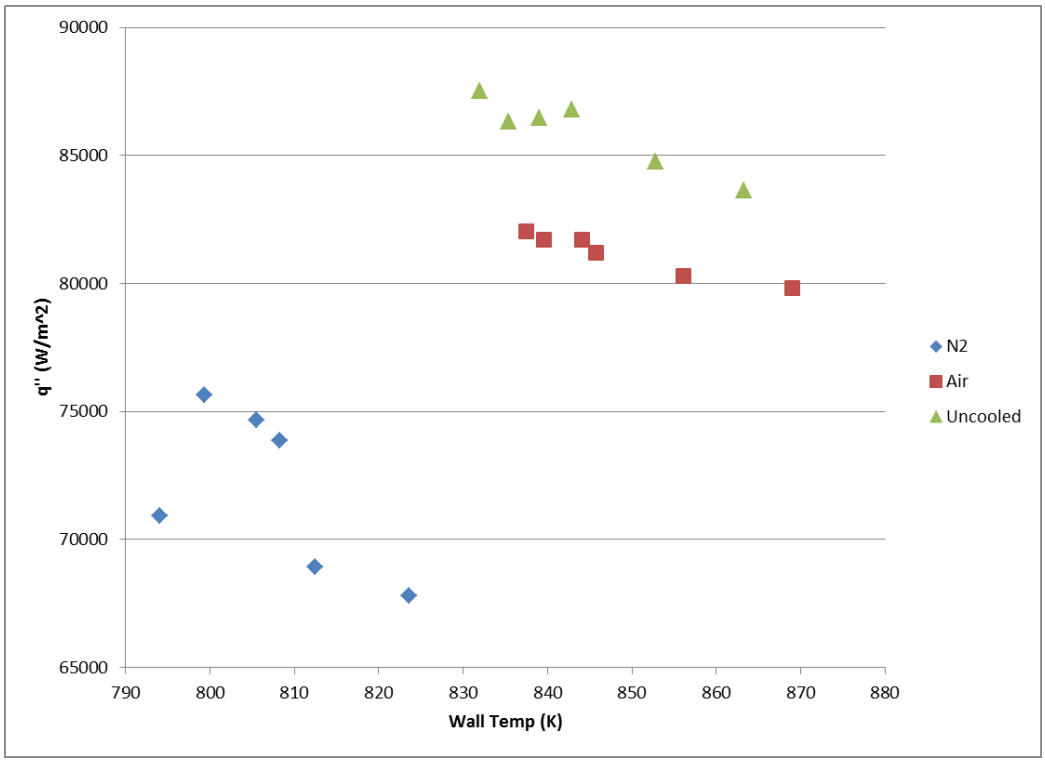

Figure 4.20: q" vs. T_w, Triple Row, M = 2, 15 Diameters Downstream of Injection

At the twenty diameter location, trends similar to those of the fifteen diameter location are seen. There remain two distinct groupings of N_2 coolant cases, attributed to the same attachment instability as is surmised to exist at the fifteen diameter location. The air case is now seen to be actively heating the wall over the uncooled case, demonstrating stronger reactions than seen at the fifteen diameter location. Additionally, the highest wall temperature data point shows an increase in heat flux over the next-highest wall temperature. This further confirms the results of Greiner et. al. [10] and indicates significant non-linearity that must be better understood by future study.

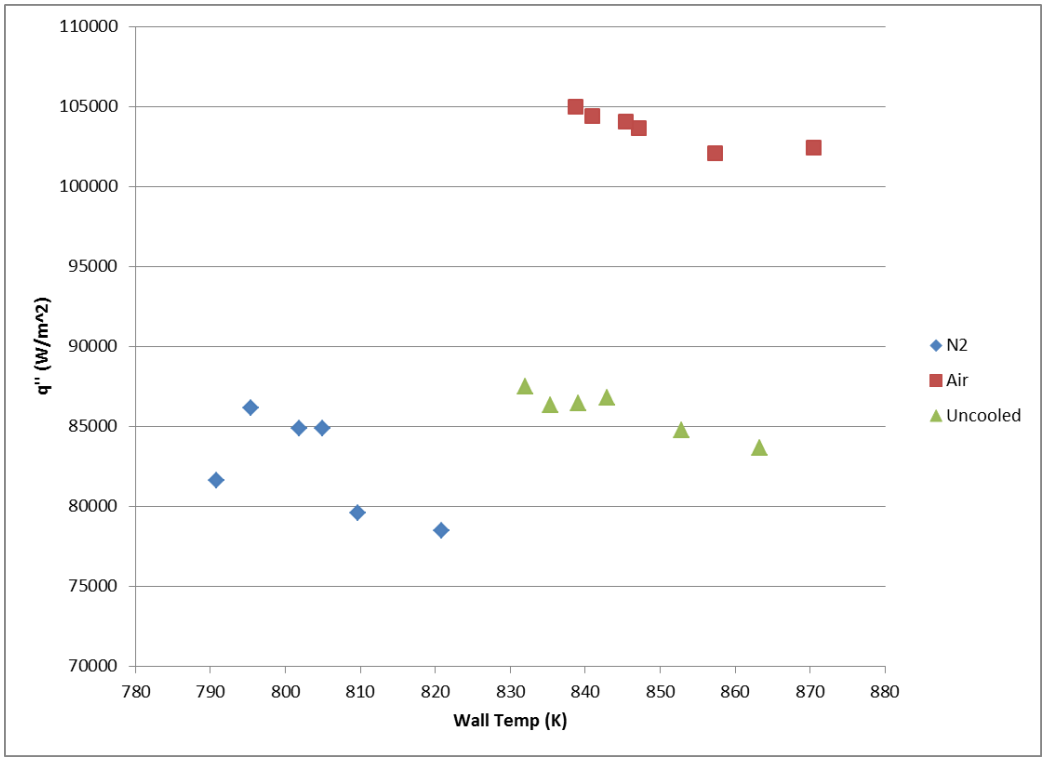

Figure 4.21: q" vs. T_w, Triple Row, M = 2, 20 Diameters Downstream of Injection

Overall the wall temperature study has strong implications for the means by which reactive film cooling is evaluated. As shown before, the augmentation metric can have misleading results due to the strong dependence of heat transfer on wall temperature. In

order to better understand the impact of wall temperature effects on evaluation, several linear fits of the data have been performed, shown in Figures 4.22, 4.23, and 4.24. The results at the seven diameter location (Figure 4.22) are presented with two linear fits for the N_2 test points, one for the previously discussed "high" results ($N_2 - 1$) and one for the "low" ($N_2 - 2$). Additionally, the highest wall temperature data point has been eliminated from the air data curve in order to improve the linearity. The author does this with the caveat that the heat flux dependence on wall temperature is linear only in the local temperature region over small wall temperature perturbations. These modifications were also made to the fifteen and twenty diameter linear fits. The resulting slopes of the N_2-2 fit and the air fit differ by 8.6%. The magnitude of the slope of these lines is proportional to the convective heat transfer coefficient, h. The similar slopes and alignment of the air-cooled case and the N_2-cooled case indicate that the difference in heat flux between the two cases is caused purely by a higher wall temperature in the air-cooled case (see equation 2.1). Thus, while the augmentation metric shows a negative number, it does not indicate that the air is cooling more effectively.

At the fifteen diameter location, the N_2-2 and air curve slopes differ by 13.2%, still demonstrating close correlation of effective heat transfer coefficient. However, the air-cooled curve no longer aligns with the nitrogen-cooled curves, showing a positive offset due to increased heat transfer from the flame. As a thought experiment the air-cooled and nitrogen-cooled curves can be extrapolated to an identical wall temperature, at which the air-cooled case would show much higher heat transfer. Neglecting radiation, and assuming a constant convective heat transfer coefficient and wall temperature, the increase in heat transfer for the air case must be caused by a rise in the driving temperature according to equation 2.4. Thus, the fifteen diameter location clearly shows an increase in heat transfer due to reactions of the coolant with the fuel-rich air.

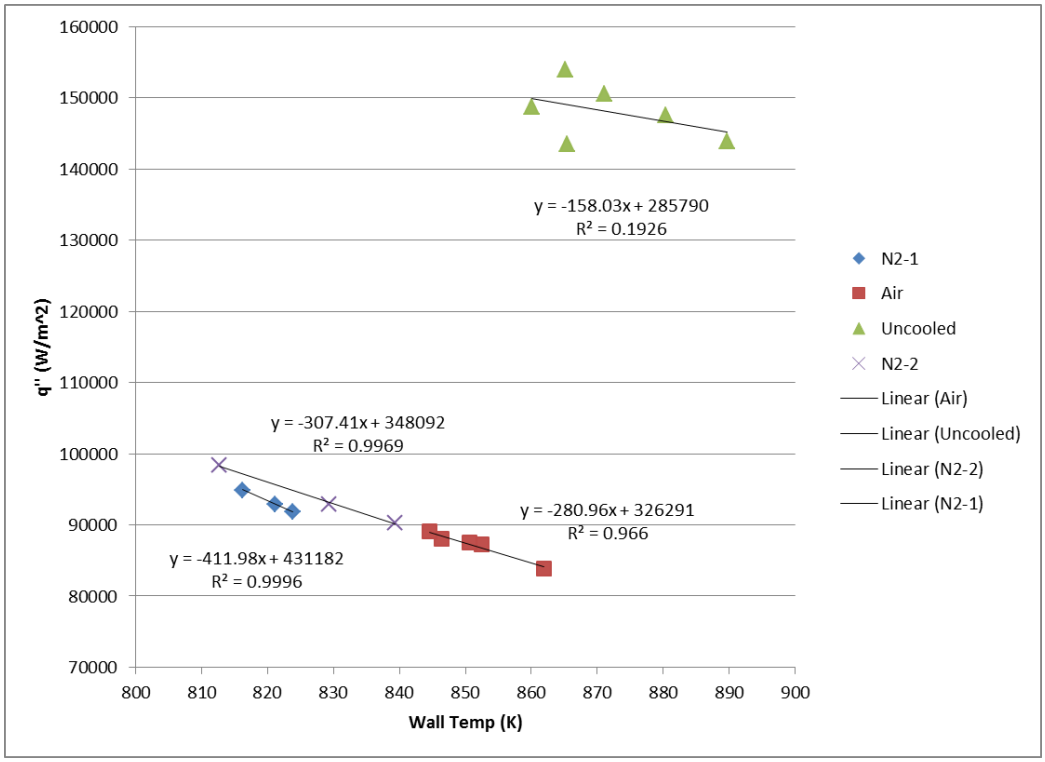

Figure 4.22: q" vs. T_w, Triple Row, M = 2, 7 Diameters Downstream of Injection

At the twenty diameter location, the N_2-2 and air curve slopes differ by 42.3%, as the reactions begin to play a larger role, and the slope of the air curve becomes significantly higher than that of the N_2 curve. The higher slope of the air curve relative to the N_2 is indicative of a proportionally higher convective heat transfer coefficient. This phenomenon can be attributed to a bulk acceleration of the flow as it reacts and heat is released. Again, the thought experiment of curve extrapolation can be performed, showing a rise in heat flux due to both an increased convective heat transfer coefficient and an increased driving temperature.

Over the course of the wall temperature study, the average freestream temperature was measured at 1573 K, differing only ± 4 K. Assuming that the freestream temperature is constant and assuming local linearity, the effective heat transfer coefficient, h_{eff}, adiabatic

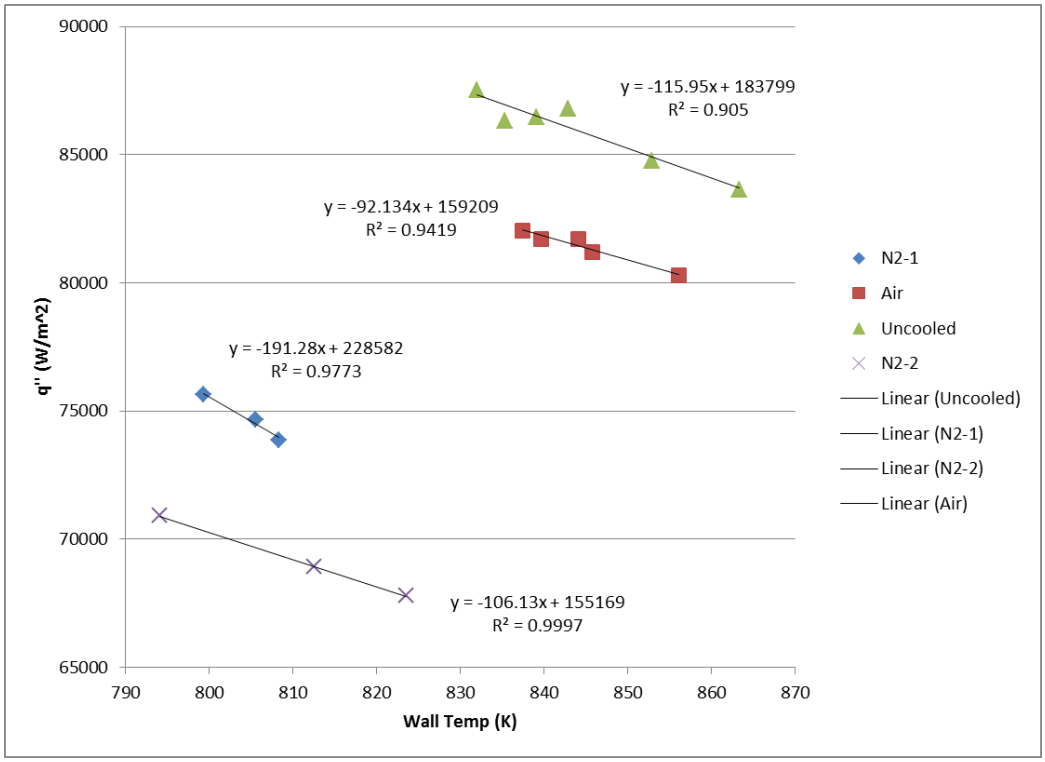

Figure 4.23: q" vs. T_w, Triple Row, M = 2, 15 Diameters Downstream of Injection

wall temperature, T_{aw}, and the adiabatic effectiveness, η, can be calculated (see equations 2.4 and 2.6). The assumption of constant freestream velocity is not valid for reacting flows, but for the purposes of this analysis the author will consider the temperature rise due to reactions to be confined to the local film temperature. The results of these calculations are shown in Table 4.3. The uncooled configuration shows adiabatic wall temperatures very close to the freestream temperature at the fifteen and twenty diameter locations, as one would expect. The higher adiabatic wall temperature at the seven diameter location is likely a result of measurement uncertainty. It is informative to see that air coolant produces negative and near-zero adiabatic effectiveness at the fifteen and twenty diameter locations. Also, this configuration produces very low adiabatic effectiveness for the non-reacting case as the flow moves downstream. This suggests that improvement could be made to the configuration in the pure film cooling sense, probably with a combination of lower blowing

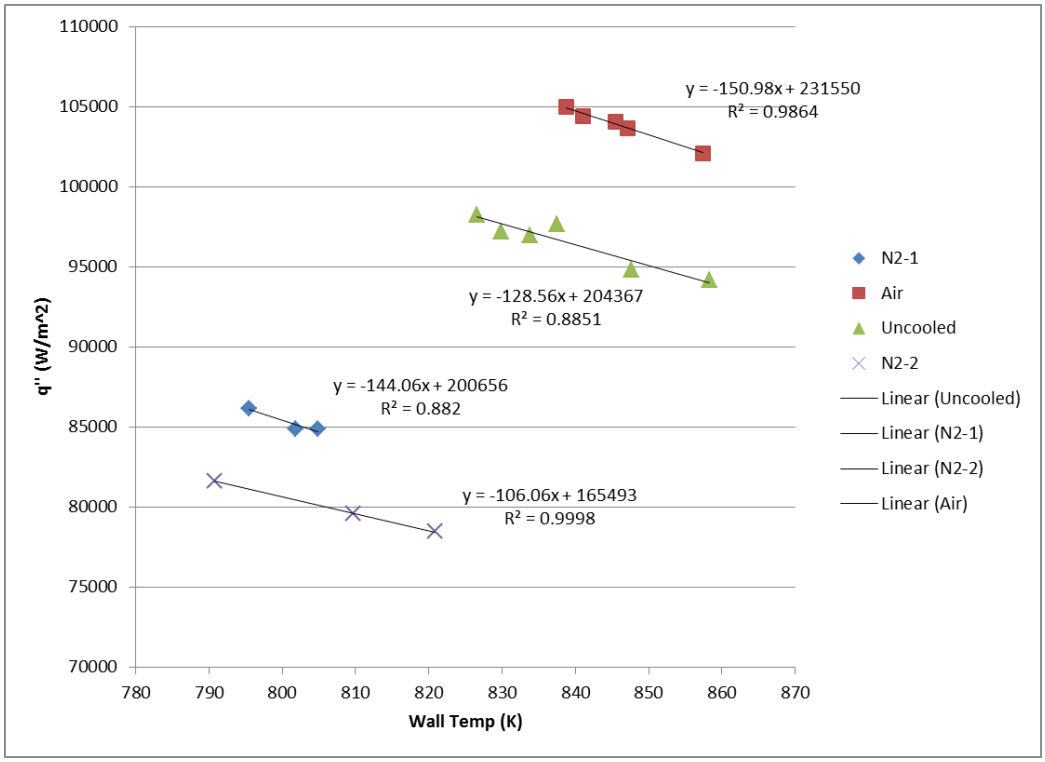

Figure 4.24: q" vs. T_w, Triple Row, $M = 2$, 20 Diameters Downstream of Injection

ratio, laidback fan geometry, and shallower injection angle. The impact that these changes would have on the reactive case would also need to be characterized.

The wall temperature study shows that locally linear analysis is still useful, although the dependence of the metrics obtained on wall temperature should always be kept in mind. The results also lead to the deduction that wall temperature effects will have an impact on augmentation calculations, due to the difference in slopes of the N_2 curves and air curves. This will be discussed further in section 3.10. Eventual design of efficient cooling schemes for real-world fuel-rich applications will require accurate prediction of the effect of wall temperature on near-wall reactions and heat transfer augmentation.

Coolant	Location	h_{eff} ($\frac{W}{m^2K}$)	T_{aw} (K)	η
Uncooled	7D	211	1808	-
	15D	118	1585	-
	20D	131	1590	-
Air	7D	119	1161	0.38
	15D	112	1728	-0.14
	20D	143	1533	0.04
N_2-1	7D	124	1047	0.49
	15D	97	1195	0.35
	20D	110	1393	0.17
N_2-2	7D	126	1132	0.41
	15D	91	1462	0.10
	20D	104	1560	0.01

Table 4.3: Wall Temperature Study Performance Metrics

4.7 Potential Heat Release

Different configurations tested in the current research have so far been compared at identical blowing ratios regardless of the number of holes they possess. As a result, the mass flow rate of coolant for a blowing ratio varies in configurations with different numbers of holes. As mass flow rate of coolant increases, the chemical potential for heat release climbs as well. In order to control for this variation, heat absorption in the wall was compared to the magnitude of the predicted maximum potential heat release for each configuration. The NASA-developed program Chemical Equilibrium with Applications (CEA) was used to predict the chemical potential energy of the coolant. Details on its use are described in Appendix A. As the name implies, the program assumes chemical equilibrium and solves for composition by minimizing the Gibb's Free Energy. The

program is then able to predict thermodynamic properties based on a large NASA database. A further assumption made in the author's application is one of an adiabatic flame. While the assumptions of chemical equilibrium and an adiabatic flame will not hold true for the flow, they do allow the prediction of the maximum potential heat release for the given inputs.

As a validation, CEA was used to predict the freestream composition (WSR products) at the measured freestream temperature during testing of the Five Row configuration. While the test setup had the ability to measure CO and CO_2 emissions, it could not measure the quantity of other species. As such, the CEA results for these species at the measured freestream conditions are shown below in Table 4.4. All concentrations shown are volumetric.

	CO (%)	CO_2 (%)	T_∞
Measured	3.47	11.32	1670
CEA	4.24	8.80	1670

Table 4.4: Composition Measurement vs. Prediction, Five Row Freestream Conditions

The results show that the freestream mixture did not quite reach the predicted equilibrium state. However, the CO measurement only differs from the prediction by a net 0.8%, and the CO_2 differs by a net 2.5%. In the author's judgment, these measurements were close enough to the predictions to justify using CEA for freestream calculations. The lack of data on other species made any empirical determination of chemical potential impossible, and CEA was used for all subsequent composition calculations shown in the current section.

First, the chemical composition of the WSR products needed to be determined for each configuration. All configurations were compared at M=2.0 and $\phi = 1.175$. The

average freestream temperature for each configuration was used to calculate the equilibrium composition. This called for the use of a Temperature-Pressure (TP) method in CEA. Freestream temperatures varied widely between configurations as a result of test rig degradation over time. However, for any one cooling insert, this temperature was found to vary no more than ±5 K at a given ϕ. Because of the different temperatures, each configuration was predicted to encounter a slightly different composition, affecting the potential heat release.

The second step in the analysis was to predict the equilibrium composition of the mixture after a proportional amount of coolant air was injected. This portion used the CEA-predicted products of the WSR and air as reactants. The measured temperature of each was specified, and an enthalpy-pressure (hp) analysis performed. The resulting thermodynamic properties allowed the calculation of a heating value, which produced a maximum power generation by the coolant flame when multiplied by the mass flow rate.

The third step of the process was to determine the measured increase in heat flux and compare it to the potential heat release of the flame. The average change in heat flux from the N_2-cooled case to the air-cooled case was calculated for the second and third row thermocouple locations. These locations are shown boxed in red in Figure 4.25 on a top-down view of the instrumentation block. The boxed thermocouples were chosen because they have been shown to experience augmented heat flux for all configurations tested. They also produce largely similar heat transfer measurements due to their physical proximity.

The final step of the process was to determine a means of directly comparing an increase in heat flux $[\frac{W}{m^2}]$ to a maximum potential power generation [W]. A characteristic area was needed to normalize the heat flux data. The author selected the area of the flame sheet as the characteristic area. The resulting scaling of the parameter allows future designers to account for the ability of a configuration to both provide film cooling and

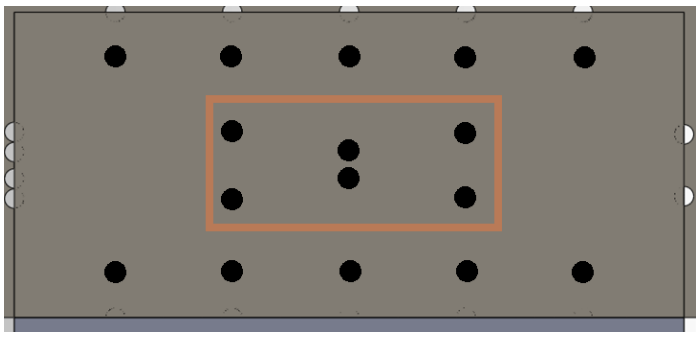

Figure 4.25: Thermocouple Locations Used in Potential Heat Release Analysis

rapidly consume radicals, allowing direct evaluation of the two primary objectives of this thesis.

The width of the flame sheet was taken to be the spanwise distance between the farthest outboard injection holes. This distance was 2.24 cm for all configurations. The length of the flame was determined using the visible spectrum photographs and methodology described in Appedix A. The photos were modified to enhance blue values in the rgb data, and are shown below in Figure 4.26. The white line in each photograph denotes the end of the flame.

Using the flame length and width, a flame sheet area was determined for each configuration. This area was multiplied by the measured heat flux increase to obtain a nominal power absorption by the wall under the flame. This value was divided by the predicted maximum heat release of the flame to obtain a percentage absorption under the flame based on a local measurement. The results are shown in Table 4.5.

By the Wall Absorption metric, the Two Row Upstream and Roll Forward configurations produce the best performance of those tested. The Five Row still does well, however this analysis shows that its flame length of 138 diameters is significantly longer than any other. The Five Row configuration therefore obtains its high cooling performance

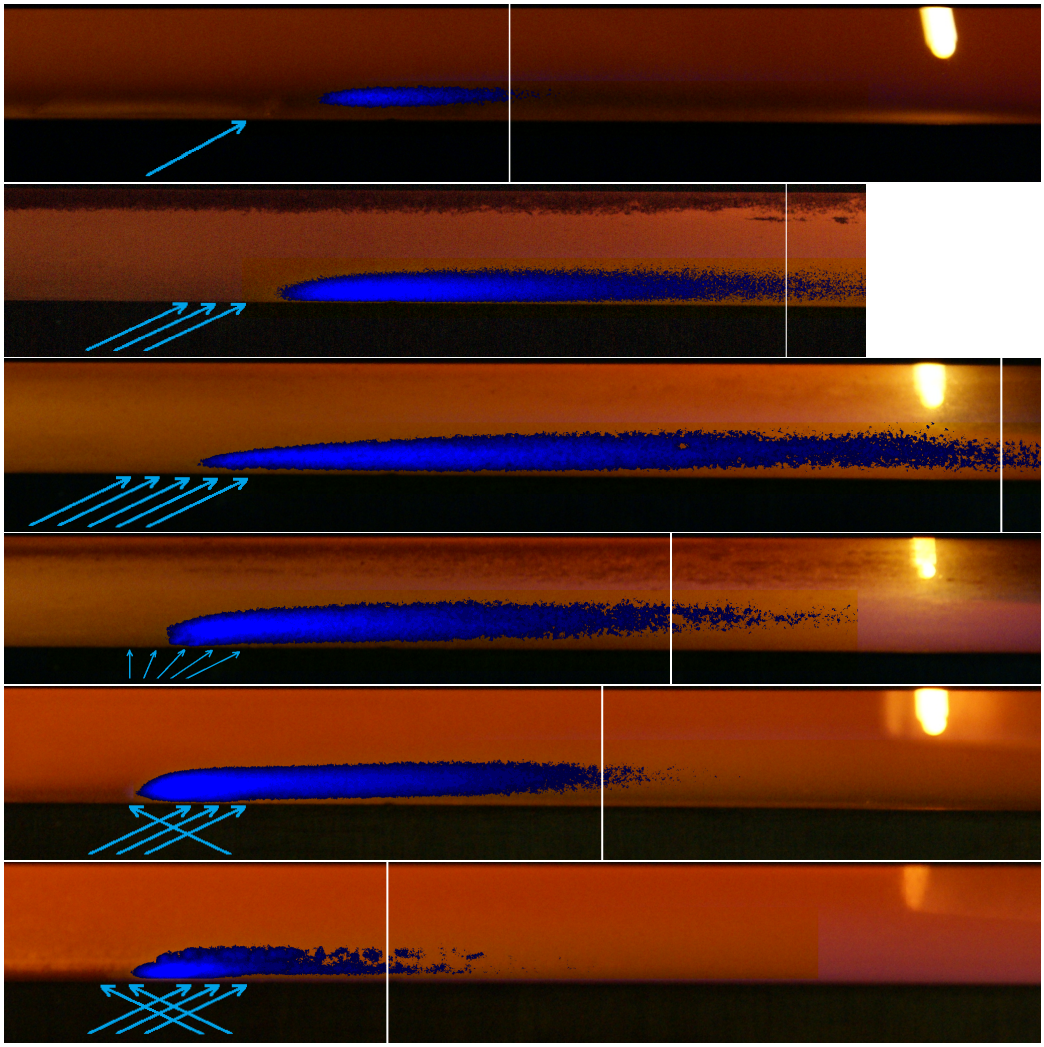

Figure 4.26: Enhanced Blue Value Photographs for Flame Length Quantification, M=2.0, ϕ = 1.175, Single Row, Triple Row, Five Row, Roll Forward, One Row Upstream, and Two Row Upstream

by reducing the mixing of oxygen and radicals, thereby spreading the reactions over a much larger area. The Roll Forward and Two Row Upstream configurations perform well because they encourage fast mixing and reactions. Taking augmentation analysis into account, the Roll Forward manages to balance these two objectives very well. The choice between these two types of cooling is therefore application dependent. A desire to consume high

Configuration	Potential Heat Release (W)	T_∞	Flame length (d)	Wall Absorption (%)
Single Row	258	1684	28.0	1.67
Triple Row	597	1654	72.0	1.44
Five Row	1022	1670	137.8	0.75
Roll Forward	1083	1678	71.8	0.57
One Row Up	765	1644	66.1	1.35
Two Row Up	1019	1528	35.8	0.49

Table 4.5: Potential Heat Release by Configuration

amounts of radicals quickly demands a mixing configuration like the Roll Forward, which can burn and protect well. However, if radical consumption is not a need for the situation, a configuration in the vein of the Five Row could conceivably delay full mixing and much of the reaction until after the flow leaves the blade, resulting in higher cooling performance.

V. Conclusions

5.1 Overview

The objectives of this thesis were first to characterize the downstream effectiveness and heat transfer characteristics of various cooling schemes. The second objective was to consume fuel radicals at a standoff distance from the wall as rapidly as possible. The third objective was to create a film cooling scheme for use in a fuel-rich environment. In support of these objectives, six cooling configurations were tested. In the "Layer Buildup" test campaign, three configurations tested the concept of building a thick coolant layer that could create a physical separation of reacting radicals from the wall by adding multiple rows of closely spaced injection hole rows. In the "Enhanced Mixing" test campaign three configurations tested the concept of a cooling scheme that could intentionally enhance mixing and burn rate with the flow while still protecting the wall. A brief study of the effect of wall temperature on the physics of reactive film cooling was conducted in order to gain a better understanding of the phenomena. Finally, a new metric for evaluating reactive film cooling was introduced in the form of wall absorption.

5.2 Findings

The Layer Buildup test campaign showed that attached coolant injected into fuel-rich flow could protect the wall by using five rows of closely spaced injection holes. This configuration created a non-reacting layer adjacent to the wall (visible in Figure 5.1) and resulted in the minimum increase in heat transfer of all configurations tested. This configuration fulfilled the thesis objective of protecting the wall downstream of injection from the effects of reaction with freestream radicals.

The Enhanced Mixing test campaign showed that increasing the angle of injection of coolant can dramatically increase reaction rate. The Roll Forward configuration flame

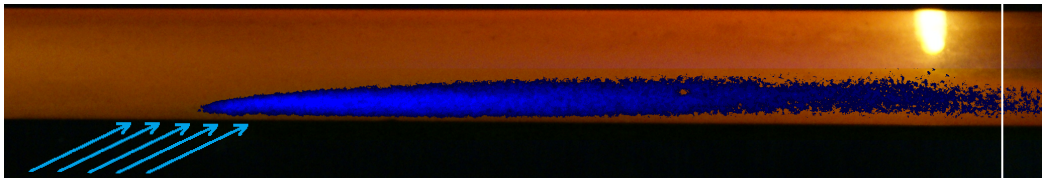

Figure 5.1: Enhanced blue value photograph of Five Row flame, M=2.0, ϕ=1.175

length of 72 diameters was 52% of the Five Row configuration's flame length. The Two Row Upstream configuration flame length of 36 diameters was 26% of the Five Row configuration's flame length. All three of these configurations were compared at identical mass flow rates.

The tradeoff between consumption schemes and protection schemes will become an important design decision in future applications. A buildup approach to a coolant layer like the Five Row will minimize the heat transfer to the wall and slow the mixing of radicals with the coolant. An approach similar to the Roll Forward configuration will allow a dramatic decrease in reaction time and length scales while still providing protection to the wall. Mach number increases, leading to increasing Rayleigh losses in combusting flows. As a result, efficiency considerations may drive the design towards rapid radical consumption to force combustion to occur prior to encountering these difficulties. Implementing a configuration like the Two Row Upstream will require intensive cold-side impingement cooling or other strategies in order to maintain acceptable wall temperatures in the immediate vicinity of the flame.

5.3 Future Work

Four new cooling designs have been proposed for the immediate future, building on experience gained in the preparation of this thesis. They include a dilution scheme, a upstream crossflow scheme, an enhanced swirl scheme, and a backward-facing step. All

four of these configurations build on the reduced augmentation shown by the Five Row Configuration, and aim to improve the Five Row by various strategies.

5.3.1 Dilution.

The dilution scheme would inject flow through large-diameter jets upstream of five 30° rows of coolant injection, as shown in Figure 5.2. The jets are intended to consume large amounts of radicals in the flow, allowing the five rows downstream to protect the wall even more effectively. The jets will also achieve high flow penetration, similar to those found in combustor liners, allowing radical consumption far into the flow.

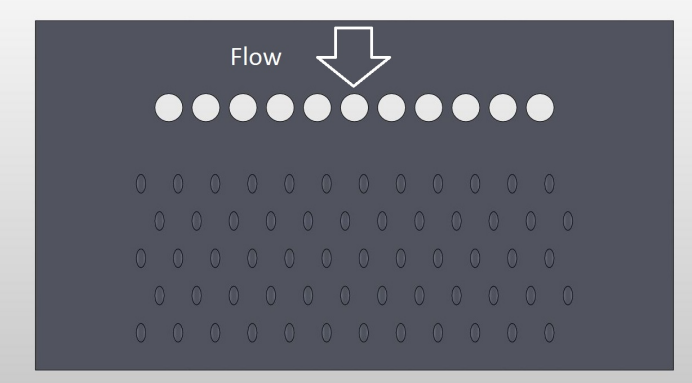

Figure 5.2: Top view of Dilution Scheme

5.3.2 Crossflow.

The crossflow scheme would inject one rows of holes 45° above the spanwise coordinate. The next row downstream would inject 45° above the spanwise coordinate in the opposite direction. These crossflow rows would be located upstream of five 30° rows of coolant injection, as shown in Figure 5.3. The opposing crossflow injection would create high turbulence and mixing, enhancing reaction rate and reducing the amount of radicals introduced to the five rows downstream.

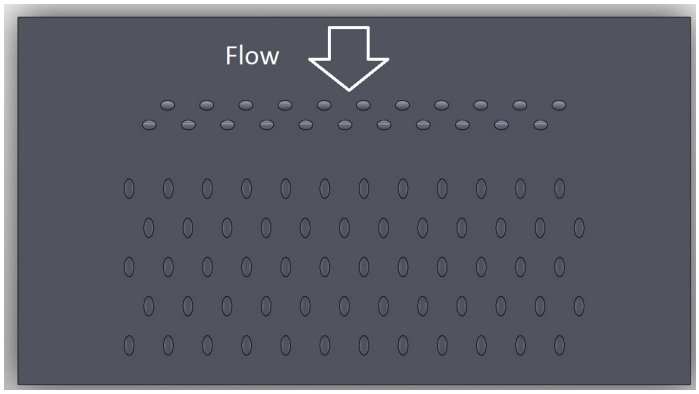

Figure 5.3: Top view of crossflow scheme

5.3.3 Enhanced Swirl.

The enhanced swirl scheme, shown in Figure 5.4, attempts to start two large vortices above the cooling region by sweeping the injection angle from outboard holes to central ones. These vortices would promote rapid mixing and circulation, enhancing the burn rate. The scheme may also demonstrate an ability to contain the flame to a smaller width spanwise. The ability to shape and control the flame in this manner would open up more cooling options for turbine designers confronted with the presence of fuel radicals. The area under the flame could be more intensively cooled with impingement and cold-side convection, while areas outside of the flame's influence could be less thoroughly cooled.

5.3.4 Backward-Facing Step.

The backward facing step has been experimented upon in previous reacting film cooling research by Milanes et. al., and was shown to enhance heat transfer to the wall. However, modification of the coolant blowing ratio allowed control of the mixing layer, making this configuration an attractive one for future research [18]. A design for a backward facing step is shown in Figure 5.5, and is followed by three rows of coolant. Normal holes are injected upstream of the step, and 20° injection holes eject coolant from the face of the step, for a total of five rows of coolant injection.

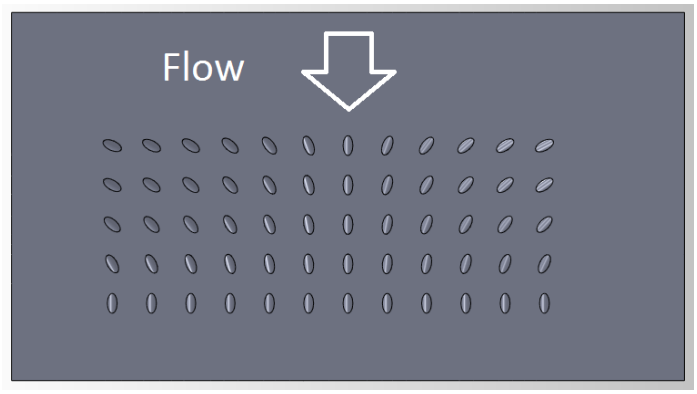

Figure 5.4: Top view of enhanced swirl scheme

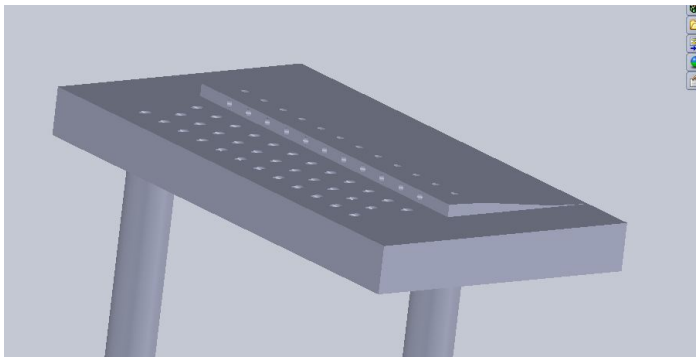

Figure 5.5: Isometric view of backward-facing step

5.3.5 Infrared Camera.

The experimental rig described in this thesis is capable of allowing infrared imaging of the instrumentation block and cooling insert via a sapphire window, as described in section 3.9. Future work should take advantage of this feature, as it would allow direct measurement of the surface temperature of both of these surfaces. Additionally, IR imaging can be manipulated in interesting ways. For instance, Figure 5.6 shows a photon count color map of two flow cases for the current test rig, looking through the sapphire window described in 3.9. The cooling plate in place is the Evans Fan configuration, described in 3.6 The photon counts for an N_2 coolant case were subtracted from the counts for an air

coolant case. As a result, places where the air-cooled case were hotter appear visible on the map. The case shown does not reflect any meaningful results for this thesis, and was only generated to test the feasibility of using an IR camera.

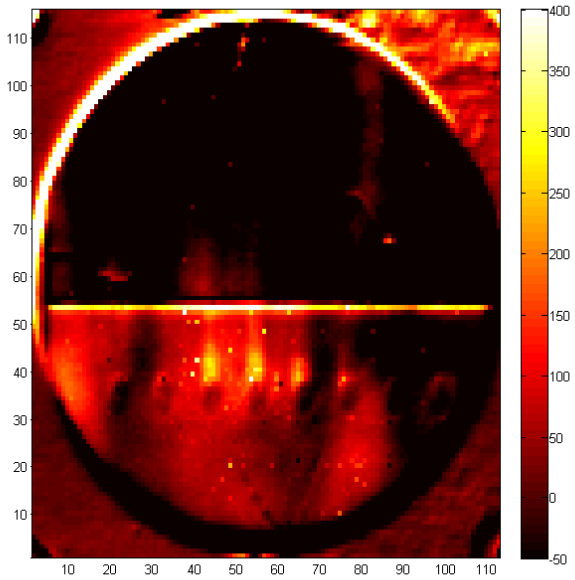

Figure 5.6: IR Camera results, (air coolant - N_2) photon count colormap

5.3.6 Rig Improvement.

Future researchers could improve the quality of their research by improving the uncertainty in the heat flux measurements. Reduced uncertainty could be accomplished by increasing the spacing between thermocouple pairs. Also, steps should be taken to minimize the streamwise surface temperature gradient on the instrumentation block. Adjustment of the cold-side cooling method would be necessary, and implementation of a mass-flow measurement capability to the cold-side cooling would allow much more detailed analysis of the effect it has on the overall heat transfer physics of the rig. DeLallo showed peak heat transfer for single rows of coolant injection around an equivalence

ratio of 1.3 [7]. This thesis showed that higher mass flow configurations increase heat transfer through ϕ=1.4. Because of the higher augmentation, future researchers may wish to examine the effect of blowing ratio on heat transfer at higher equivalence ratios than shown in this thesis. Also, while Bohan showed the majority of reactions occuring within 25D of injection [6], the new cooling strategies implemented in this thesis have shown reactions occurring much farther downstream. Future researchers may wish to quantify film effectiveness as far as 100D downstream.

5.4 Closing Thoughts

Overall, the future of reactive film cooling research is bright. While the presence of radicals near turbine blades presents a major design challenge, this thesis shows that the problem is not insurmountable. Improvements on the methods shown in this body of research will soon allow cooling schemes to be designed to encounter fuel-rich environments and thrive.

Appendix A: Processing Methods

A.1 Labview

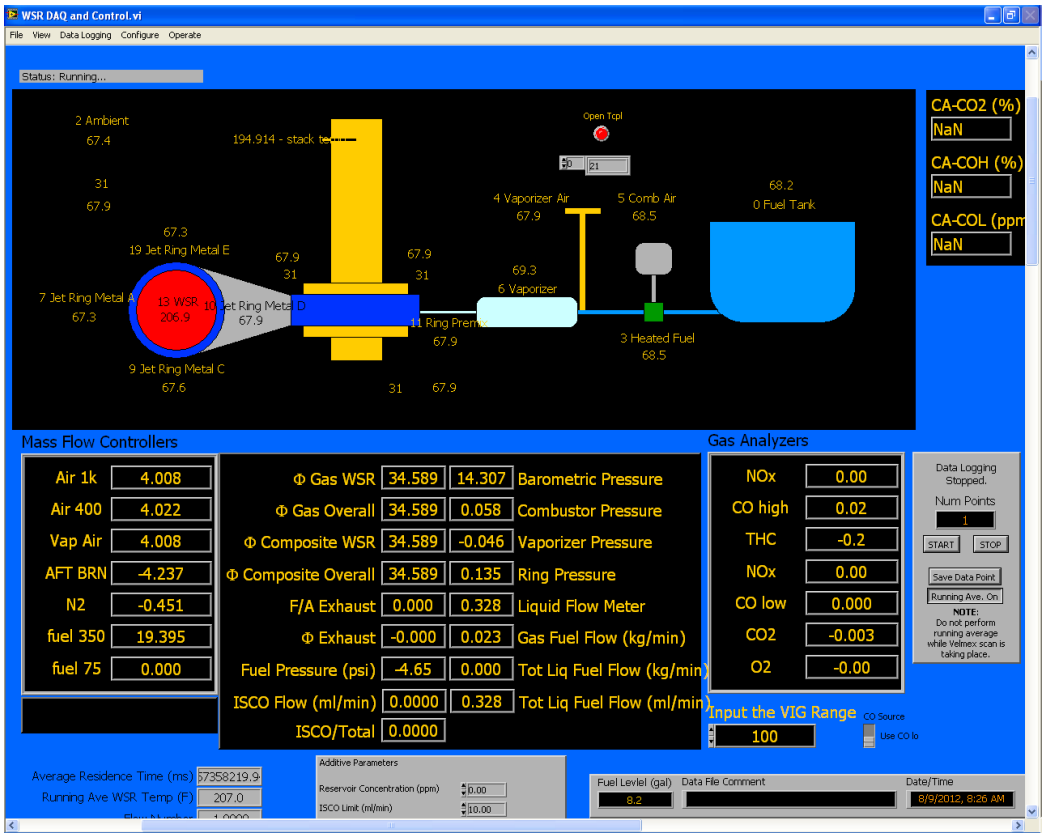

Figure A.1: Labview VI used to collect data

A.2 Excel Datasheet

A.3 Chemical Equilibrium with Applications (CEA)

The NASA-developed chemical equilibrium program CEA was used to produce predictions of the product composition and thermodynamic properties of different reactions. The program was used primarily for two calculations in this thesis: first for

Start	End	Phi	M (des) US Air(0)/N2(1	M (des) DS Air(0)/N2(1	Total Air(SL	Propane(SL	Calc Phi	Req Air US	US flow Co	M (air) US
3541	3571	1.3	1	0	2	1	425	23.3	1.304788	0.957676	0.95	0.991985
3302	3332	1.3	2	0	2	1	425.8	23.3	1.302337	1.918679	1.98	2.06392
3077	3107	1.3	3	0	2	1	425.8	23.3	1.302337	2.878018	2.82	2.939523
2834	2864	1.3	4	0	2	1	425.8	23.3	1.302337	3.837358	3.84	4.002754
4542	4572	1.3	1	0	2	0	425	23.3	1.304788	0.957676	0.95	0.991985
4321	4351	1.3	2	0	2	0	425	23.3	1.304788	1.915351	1.87	1.952645
4032	4062	1.3	3	0	2	0	425	23.3	1.304788	2.873027	2.9	3.028165
3811	3841	1.3	4	0	2	0	425	23.3	1.304788	3.830702	3.84	4.009709
8598	8628	1.5	1	0	2	1	425	26.7	1.495186	0.968439	0.95	0.98096
8351	8381	1.5	2	0	2	1	425	26.7	1.495186	1.936878	1.95	2.01355
8112	8142	1.5	3	0	2	1	425	26.7	1.495186	2.905317	2.931	3.02652
7004	7034	1.5	4	0	2	1	425	26.7	1.495186	3.873756	3.955	4.083892
7881	7911	1.5	1	0	2	0	425	26.7	1.495186	0.968439	0.92	0.949982
7641	7671	1.5	2	0	2	0	425	26.7	1.495186	1.936878	1.98	2.044527
7425	7455	1.5	3	0	2	0	425	26.7	1.495186	2.905317	2.9	2.99451
7221	7251	1.5	4	0	2	0	425	26.7	1.495186	3.873756	3.955	4.083892
5620	5650	1.1	1	0	2	1	425	19.65	1.10039	0.946121	0.978	1.033695
5423	5453	1.1	2	0	2	1	425	19.65	1.10039	1.892242	1.875	1.981777
5155	5185	1.1	3	0	2	1	425	19.65	1.10039	2.838362	2.82	2.980592
4944	4974	1.1	4	0	2	1	425	19.7	1.10319	3.785116	3.84	4.057999
6588	6618	1.1	1	0	2	0	425	19.65	1.10039	0.946121	0.95	1.0041
6364	6394	1.1	2	0	2	0	425	19.65	1.10039	1.892242	1.86	1.965922
6145	6175	1.1	3	0	2	0	425	19.65	1.10039	2.838362	2.815	2.975307
5911	5941	1.1	4	0	2	0	425	19.65	1.10039	3.784483	3.758	3.972009
969	999	0.6	1.5	0	2	0	425.8	10.75	0.600864	1.379415	1.35	1.468014
1249	1279	0.6	1	0	2	0	425.8	10.75	0.600864	0.91961	0.95	1.033047
1511	1541	0.6	2	0	2	0	425.8	10.75	0.600864	1.83922	1.872	2.035646
1830	1860	0.6	1.5	0	2	1	425.8	10.75	0.600864	1.379415	1.38	1.500636
2143	2173	0.6	1	0	2	1	425.8	10.75	0.600864	0.91961	0.95	1.033047
2368	2398	0.6	2	0	2	1	425.8	10.75	0.600864	1.83922	1.87	2.033471

Figure A.2: Excel Sheet used for Data Processing

freestream composition following reaction completion in the WSR at the measured "stack" temperature, and second for an adiabatic flame temperature and enthalpy rise for the complete reaction of injected coolant with the WSR products. A sample input/output report for the program is displayed below in Figure A.3.

A.4 Determination of Wall Temperature and Heat Flux

The method described here was initially described in the research of Evans [9]. At steady state, 1-dimensional heat transfer, the convective heat transfer into the block is equal to the conductive heat transfer through the block. As such, the thermocouple pairs embedded at differential depths allow the researcher to closely estimate heat transfer and wall temperature by using Fourier's Law, shown below in Equation A.1.

```
*******************************************************************************

NASA-GLENN CHEMICAL EQUILIBRIUM PROGRAM CEA2, MAY 21, 2004
BY  BONNIE MCBRIDE AND SANFORD GORDON
REFS: NASA RP-1311, PART I, 1994 AND NASA RP-1311, PART II, 1996

*******************************************************************************


prob
hp p,atm=1 t,k=1800
react
fuel=CO wt=0.04333 t,k=1670
fuel=Ar wt=0.01202 t,k=1670
fuel=CO2 wt=0.14112 t,k=1670
fuel=H wt=0 t,k=1670
fuel=H2 wt=0.00163 t,k=1670
fuel=H2O wt=0.09937 t,k=1670
fuel=N2 wt=0.70253 t,k=1670
fuel=OH wt=0 t,k=1670
oxid=Air wt=0.0 t,k=456
output
siunits massf
plot h u
end

OPTIONS: TP=F  HP=T  SP=F  TV=F  UV=F  SV=F  DETN=F  SHOCK=F  REFL=F  INCD=F
RKT=F  FROZ=F  EQL=F  IONS=F  SIUNIT=T  DEBUGF=F  SHKDBG=F  DETDBG=F  TRNSPT=F

T,K =  1800.0000

TRACE= 0.00E+00  S/R= 0.000000E+00  H/R= 0.000000E+00  U/R= 0.000000E+00

P,BAR =    1.013250

REACTANT        WT.FRAC  (ENERGY/R),K   TEMP,K  DENSITY
EXPLODED FORMULA
F: CO            0.043330  -0.789774E+04  1670.00  0.0000
C  1.00000  O  1.00000
F: Ar            0.012020   0.342962E+04  1670.00  0.0000
AR 1.00000
F: CO2           0.141120  -0.387041E+05  1670.00  0.0000
C  1.00000  O  2.00000
F: H             0.000000   0.296487E+05  1670.00  0.0000
H  1.00000
F: H2            0.001630   0.503225E+04  1670.00  0.0000
H  2.00000
F: H2O           0.099370  -0.223018E+05  1670.00  0.0000
H  2.00000  O  1.00000
F: N2            0.702530   0.533628E+04  1670.00  0.0000
N  2.00000
F: OH            0.000000   0.959486E+04  1670.00  0.0000
O  1.00000  H  1.00000
O: Air           0.000000   0.541176E+03   456.00  0.0000
N  1.56168  O  0.41959  AR 0.00937  C  0.00032

SPECIES BEING CONSIDERED IN THIS SYSTEM
(CONDENSED PHASE MAY HAVE NAME LISTED SEVERAL TIMES)
LAST thermo.inp UPDATE:    9/09/04

g 3/98  *Ar          g 7/97  *C           tpis79  *CH
g 4/02  CH2          g 4/02  CH3          g11/00  CH2OH
g 7/00  CH3O         g 8/99  CH4          g 7/00  CH3OH
srd 01  CH3OOH       g 8/99  *CN          g12/99  CNN
tpis79  *CO          g 9/99  *CO2         tpis91  COOH
```

Figure A.3: CEA Input/Output Report for Five Row Coolant-Anchored Flame Equilibrium Calculation

$$q'' = -k\frac{dT}{dy} \tag{A.1}$$

The y coordinate will be considered the depth into the instrumentation block from the hot surface, as discussed in the nomenclature. This may be rearranged and integrated as shown in Equation A.2.

$$\int q''dx = -\int zdT \tag{A.2}$$

The value of thermal conductivity in Hastelloy-X® varies with temperature, as shown in Figure A.4. The values in this chart were obtained from the technical handbook issued by the alloy manufacturer, Haynes International [1].

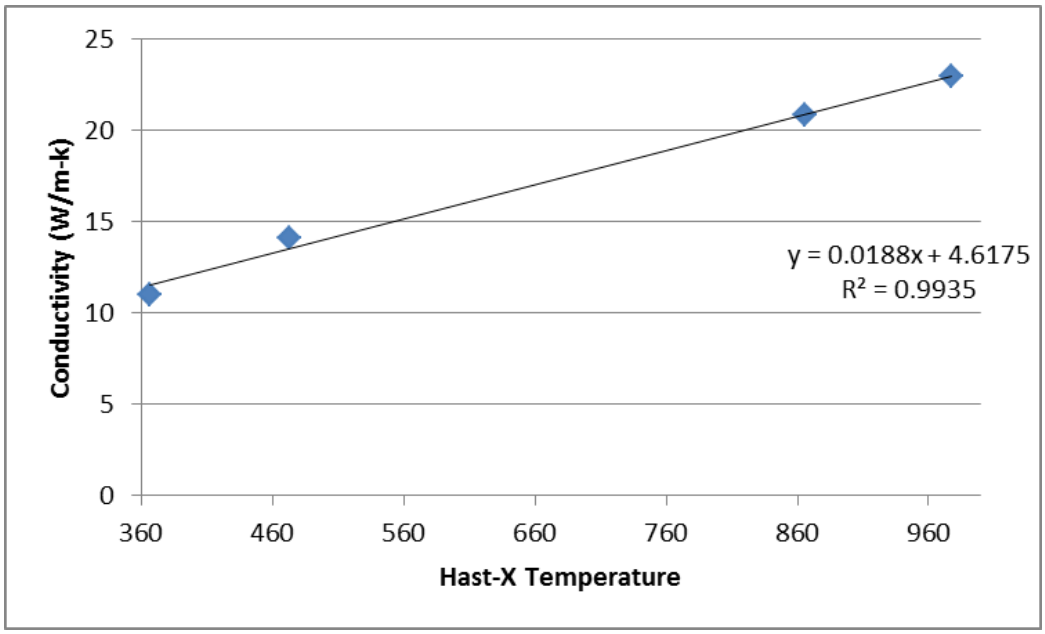

Figure A.4: Hastelloy-X® Themal Conductivity [1]

The conductivity will be represented as linear, taking the form $k = a_0 + a_1T$, where a0=4.618 and a1=0.0188 as shown by the fit on the chart. With this approximation in place, evaluation of equation A.2 gives equation A.3.

$$q'' x - C = -(a_0 T + \frac{a_1}{2} T^2) \tag{A.3}$$

Two thermocouple depths at a wall location give two equations (A.4 and A.5) that can be evaluated:

$$\frac{a_1}{2} T_1^2 + a_0 T_1 + q'' x_1 - C = 0 \tag{A.4}$$

$$\frac{a_1}{2} T_2^2 + a_0 T_2 + q'' x_2 - C = 0 \tag{A.5}$$

Setting these equal gives a solution for q" shown in equation A.6.

$$q'' = \frac{\frac{a_1}{2}(T_1^2 - T_2^2) + a_0 * (T_1 - T_2)}{(x_2 - x_1)} \tag{A.6}$$

Following this, q" can be plugged back into equations A.4 or A.5 and solved for C. With this number, wall temperature can be calculated by plugging C into equation A.3, setting x=0, and applying the quadratic formula.

A.5 Determination of Flame Length

Each Photograph was loaded into Matlab as a matrix of values describing each pixel. A pertinent section of the photo surrounding the visible flame was chosen for detailed analysis. Each pixel was described by a red, green, and blue eight-bit value. First, to enhance visualization of the flame, all pixels with blue values above a certain threshold were modified by scaling them up. The program then summed the blue values in each pixel column as a relative measure of flame strength along the streamwise coordinate. The results of this sum are shown for all six tested configurations at M=2.0 and $\phi = 1.175$ in Figure A.5.

The flame was considered to end when the blue value reached ten percent of its maximum value for the flame. The program drew a vertical white line at this calculated

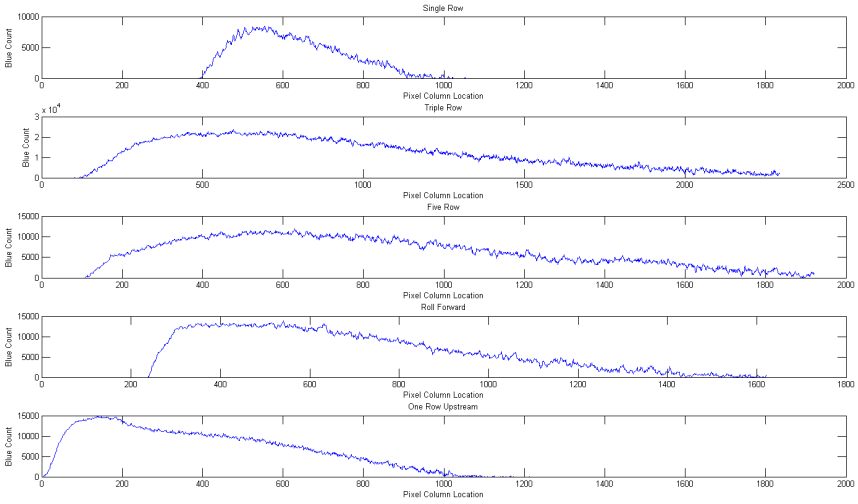

Figure A.5: Total Blue Value in each Column of Pixels

location for each photograph. The code used to perform this analysis is shown in Figure A.6.

```
%% Image Processing for thesis
clc
close all
clear all

Configs={'SingleRow' 'ThreeRow' 'FiveRow' 'Rollforward' '1up'};
Titles={'Single Row' 'Triple Row' 'Five Row' 'Roll Forward' 'One Row
Upstream'};

[bleh num_configs]=size(Configs);
clear bleh

suffix='_M_2.JPG';

for n=1:num_configs
    Picture{n}=imread([Configs{n} suffix]);
end

%% Manipulate image
close all

TRow=[1560 1320 1360 1340 1360];
BRow=[1700 1540 1500 1500 1500];
LCol=[1580 1580 1580 1580 1580];
RCol=[3400 3872 3500 3200 3400];

% TRow=1;
% BRow=2592;
% LCol=1;
% RCol=3872;

Height=BRow-TRow; %Pixels
Width =RCol-LCol; %Pixels



for o=1:num_configs
%Cut down image
Picture_m{o}=Picture{o};%(TRow:BRow,LCol:RCol,:);

%Modify color

for n=TRow(o):BRow(o)
    for m=LCol(o):RCol(o)
        if Picture_m{o}(n,m,3)>110
            Picture_m{o}(n,m,3)=uint8(256);
            Picture_m{o}(n,m,1)=uint8(0);
            Picture_m{o}(n,m,2)=uint8(0);
        elseif Picture_m{o}(n,m,3)>100
            Picture_m{o}(n,m,3)=uint8(218);
            Picture_m{o}(n,m,1)=uint8(0);
            Picture_m{o}(n,m,2)=uint8(0);
        elseif Picture_m{o}(n,m,3)>90
            Picture_m{o}(n,m,3)=uint8(179);
            Picture_m{o}(n,m,1)=uint8(0);
            Picture_m{o}(n,m,2)=uint8(0);
        elseif Picture_m{o}(n,m,3)>80
```

Figure A.6: Code used to Process Photographs for Flame Length

Appendix B: Design Tools

B.0.1 Trip Height Calculation.

Air flow exiting the UCC is expected to be fully turbulent and highly vortical by nature. To ensure representative conditions, a trip step was included at an upstream location in the test section, the necessary height of which was analytically determined before construction. To begin the analysis, the flow was assumed to have no boundary layer at the beginning of the rig's rectangular cross section. This is a conservative assumption, based on the fact that the flow would experience a favorable pressure gradient passing through the transition piece (see Figure 3.4) before entering the rectangular section. Based on worst case assumptions of expected mass flow rate, temperature, and pressure, the Reynolds number was calculated. Based on a given necessary transition location, the step location and height was selected from a chart of experimental data shown in Figure B.1, obtained from Reference blank. The trip was selected to have a height of 0.276 in. at a location of 0.276 in. downstream from the beginning of the rectangular cross section, as shown in 3.7. Code used in this calculation is included in Figure B.2.

B.1 Thermocouple depth

The depth of the lower row of thermocouples was set according to a preliminary uncertainty analysis conducted in the finite element solver Abaqus. An initial two dimensional study was run using a solver created by the author in Matlab. Results are shown in B.3. Boundary conditions on the instrumentation block were estimated based on the findings in [9] and [7]. Based on this preliminary analysis, the decision was made to water cool only the bottom half of the sides of the instrumentation block in order to maintain the heat flux as one dimensional as possible where it is measured by the thermocouples. Further data fidelity was necessary in order to perform a predictive

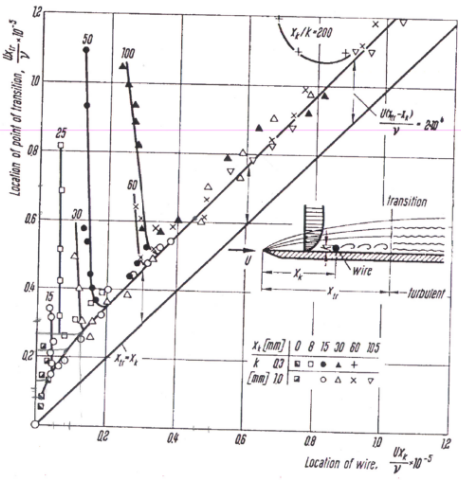

Fig. 17.41. Distance between point of transition, x_{tr}, and the position of the tripping x_k, for "fully effective" operation, plotted from eqn. (17.30), after K. Kraemer [70]

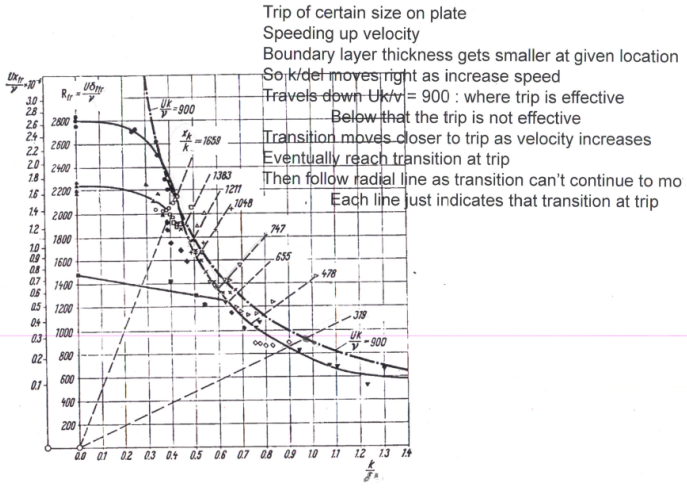

Figure B.1: Charts Used to Calculate Trip Height

uncertainty analysis on the impact of thermocouple placement on the data. A full three dimensional FEM analysis was therefore performed.

B.1.1 2-D Analysis.

B.1.2 3-D Analysis.

```
function Film_Cooling_Calculations
%--------------------------------------------------------------------------
%Date:    April 24, 2012
%Purpose: Begin Preliminary Calculations of Aspects of Film Cooling Test Rig
%Author:  Jacob Robertson
%--------------------------------------------------------------------------
%% Trip height
clc
clear
close all

%--------------------------------------------------------------------------
%SLPM definitions
%http://www.timedomaincvd.com/CVD_Fundamentals/introduction/ideal_gas.html
%1 SLPM = 7.4E-4 moles/second
% This code will use Standard conditions at 1 atm( 101325 Pa) and 273.15 K
% (0 deg C) and the ideal gas law to convert such that:
%Qs=Q*(Tref/T)*(P/Pref)
%Q=Qs*(T/Tref)*(Pref/P) (assuming constant R- worst case)
%This conforms to AFRL SLPM calculation based on ref. density at 1 atm/70F.
%--------------------------------------------------------------------------

%k=[2.42 2.18 2.12 2.06]*10^-3; %wire trip heights (m)

%Test Section Conditions:

P     = 101325       ; % Estimated Pressure (N/m^2)

Tmax  = 1400         ; % Maximum inlet static temperature (K)

R     = 287          ; % Worst case Gas Constant (air) (J/Kg-k)

Qsmin  = 1.4 / 60    ; % volumetric flow rate, (SLPM/(1000*60))

%Reference conditions:

Prefs   = 101325     ; % Reference Pressure, volumetric correction (Pa)

Trefs   = 273.15     ; % Reference Temperature, volumetric correction (For US Standard↙
liters, SI is 293.15) (K)

As    = 0.00129032   ; %Inlet cross sectional area (m^2)  (2"^2)

Trefmu  = 300        ; % Reference Temperature for Sutherland's law (K)     (DeWitt H.T.)

Muref = 184.6e-7     ; % Reference viscosity for Sutherland's law (N-s/m^2) (DeWitt Heat↙
Transfer)

Mumax = Muref*(Tmax/Trefmu)^1.5*((Trefmu+110)/(Tmax+110)); %viscosity from Sutherland's↙
law (air) (N-s/m^2)
```

Figure B.2: Matlab routine used to help determine trip height

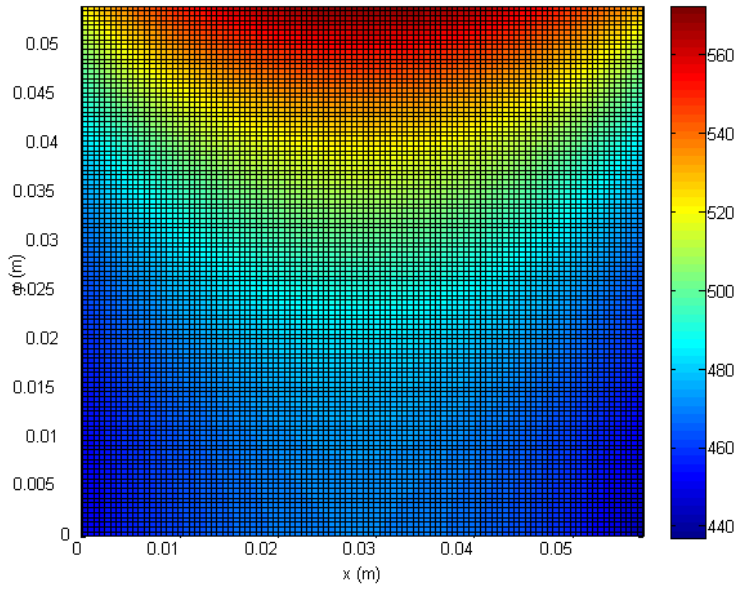

Figure B.3: 2-D Analysis Results

```
%% 2-D Heat Transfer FEM Solver
%-------------------------------------------------------------------------
%Title:  3-D, SS Rectangular block Steady State Heat Tranfer Solver
%Self contained, no input/output outside of code
%Author: Jacob Robertson, 2LT, USAF
%Date:   29 May 2012 Ano Domini
%-------------------------------------------------------------------------
clc
clear
close all

% 3 Node Triangular elements

n_node_el=3;

%Divide into rectangular blocks, each block contains two triangular
%elements

t=0.001; %m, element "thickness"

%Solid "block" portion (BLOCK)
X_L_block= 0.05715;  % (m)
Y_L_block= 0.05398;  % (m)



%Number of rectangular "divisions" in x, and y (BLOCK)
x_div_n_block= 100;
y_div_n_block= 110;

x_div_block=X_L_block/x_div_n_block;
y_div_block=Y_L_block/y_div_n_block;

x=0:x_div_block:X_L_block;
x=x';
[Row_x Col_x]=size(x);

y=0:y_div_block:Y_L_block;
y=y';
[Row_y Col_y]=size(y);

n_point_block =(x_div_n_block+1)*(y_div_n_block+1);
n_el_block    = x_div_n_block*y_div_n_block*2;

%Assign coordinates to nodes
Point_num=1;
for i=1:Row_x
    for j=1:Row_y
        Node(i,j).coord=[x(i),y(j),Point_num];
        Point_num=Point_num+1;
```

Figure B.4: 2-D Analysis Code

Appendix C: Calibration

C.1 Air Calibration

A calibration of the air flow controllers was conducted prior to testing in order to improve accuracy during the test. Airflow rates were calculated in Standard Liters per Minute (SLPM). In the fuels branch of AFRL, SLPM is calculated by multiplying the volumetric flow rate in Liters per minute times the ratio of the gas density to the density of the gas at one atmosphere and 70°F. Three air flow controllers were used: A 1000 SLPM max flow rate controller, a 400 SLPM max flow rate controller (which gives greater control fidelity at lower rates), and a fuel vaporizer air controller (with a max supply rate of 75 SLPM). The calibration was conducted by forcing the air supply through a sonic nozzle of known diameter. A 0.125 in. diameter example is pictured in Figure C.1.

Figure C.1: Sonic Nozzle, D=0.125 in.

Upstream static pressure and temperature were measured. The supply pump drew an electric current corresponding to the flow rate. The flow rate was calculated using

a spreadsheet generated by the manufacturer of the nozzle (Flow Systems Inc.). The spreadsheet ensures choked flow based on the upstream measurements, and calculates the flow rate in SLPM taking account of viscous effects and air properties. The supply flow was swept over the range of expected use, producing a plot of the variation of the current with the flow rate. A linear fit was performed on the data using Excel, and resulting in a minimum R^2 value of 0.9999 This data is shown in Figures C.2, C.3, and C.4.

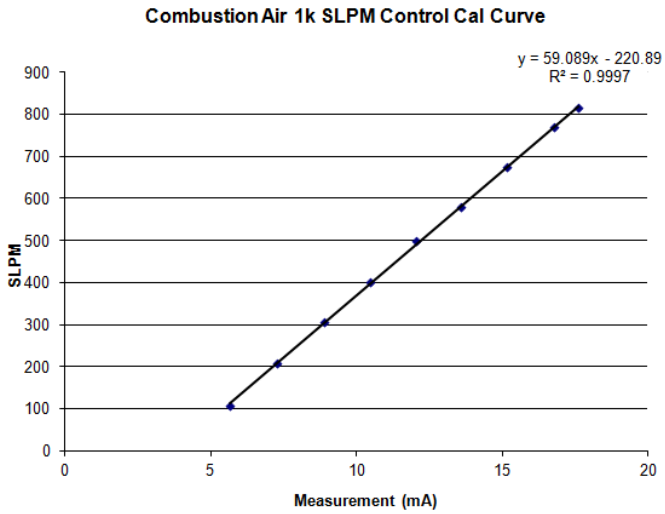

Figure C.2: 1000 SLPM Air Supply Control Calibration Curve

C.2 Fuel Calibration

Calibration was conducted by pumping the supply through a volumetric flow meter, pictured in Figure C.5. Pressure and temperature measurements were taken upstream in order to convert the volumetric flow into SLPM. The total volume passed through the meter was timed over a course of approximately five minutes in order to obtain an average flow rate. A linear curve with a minimum R^2 of 0.9985 was generated correlating electric current drawn by the pump to SLPM.

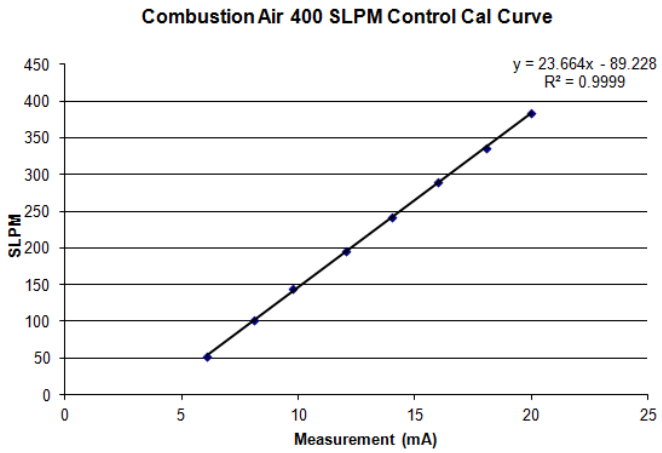

Figure C.3: 1000 SLPM Air Supply Control Calibration Curve

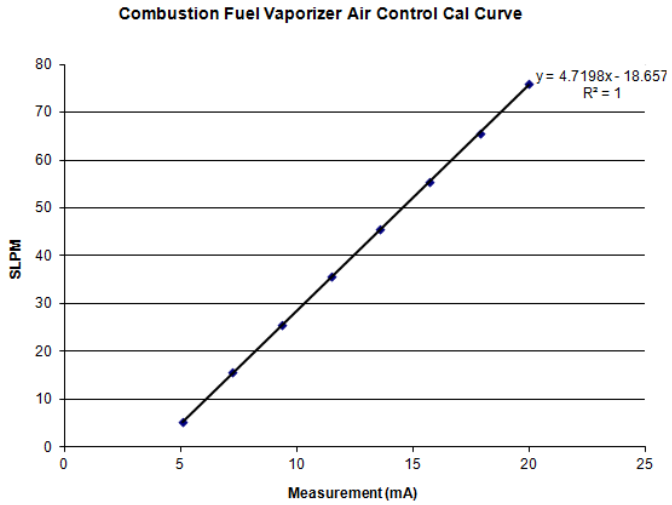

Figure C.4: Fuel Vaporizer Air Control Calibration Curve

Figure C.5: Flow Meter Used to Calibrate Fuel Supply

Appendix D: Errors and Mitigation

D.1 Phi mistake

Originally a ϕ of 1.3 was selected to be the "crux" point of the blowing ratio and ϕ sweeps. This was due to DeLallo's research showing peak heat release around this flow condition. Unfortunately an early mistake in fuel flow calibration went uncaught until much testing had been accomplished. What was thought to be a ϕ of 1.3 was actually 1.175. Time constraints prevented re-testing previous configuration. As such, a ϕ of 1.175 was adopted as the new "crux" point of the sweeps for new configurations. The test matrices shown in Section 4.1.2 were those implemented after this correction was made. The original ϕ sweep was intended to cover 1.1, 1.25, 1.3, 1.35, and 1.5. The test matrices shown cover these points and added 1.175 so that pre-mistake testing was still directly comparable. Also, The 1.5 point was removed and replaced with 1.4 because the reactor could not sustain flames beyond this point consistently. Because of the original mistake, not all configurations have the full range of test points indicated in the test matrices.

D.2 Spanwise Thermocouple Location Mistake

Before design finalization the author made the decision to locate thermocouples both directly in line with and directly between the trailing edge holes of the Single Row configuration in the spanwise coordinate. This would allow evaluation of area covered directly by the hole and area covered by diffused coolant as well as conduction. Unfortunately, a last-minute design mistake was found in the Single Row configuration, and the number of holes was changed from 11 to 12. In an oversight, the instrumentation block was not updated to reflect this change, and all thermocouples happened to line up directly between the trailing edge holes. This error prevented the researcher from evaluating the lateral diffusion of the cooling schemes.

Appendix E: Detail Drawings

All dimensions are given in millimeters.

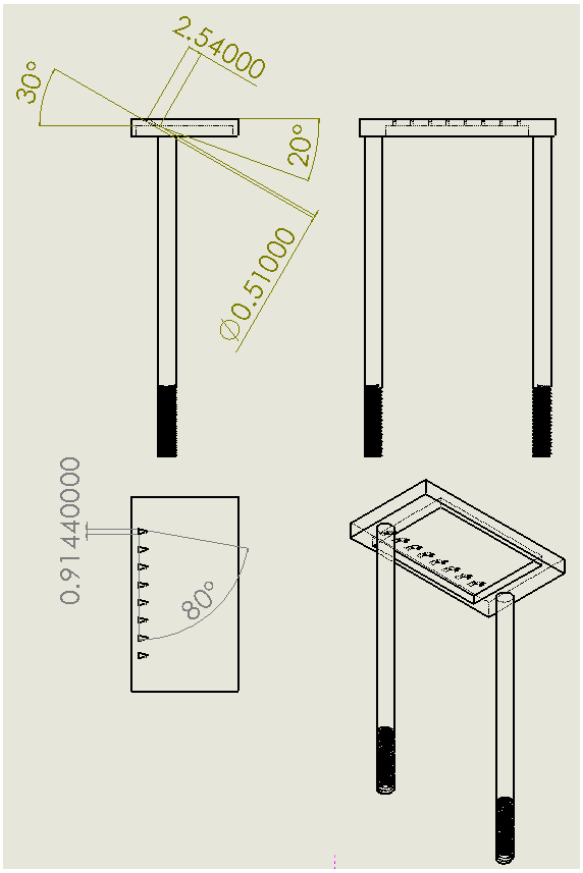

Figure E.1: Evans' Fan Cooling Configuration

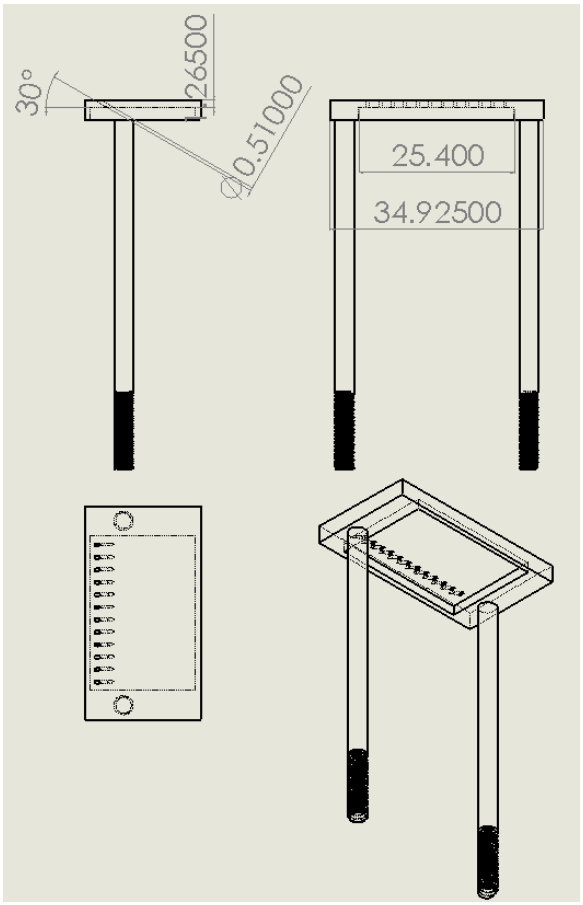

Figure E.2: Single Row of Cylindrical Holes Cooling Configuration

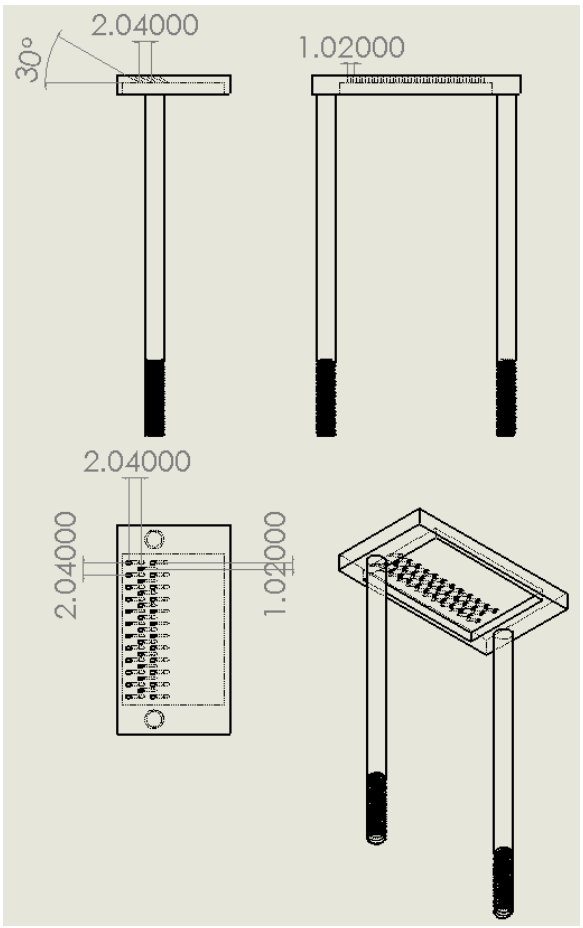

Figure E.3: Triple Row of Cylindrical Holes Cooling Configuration

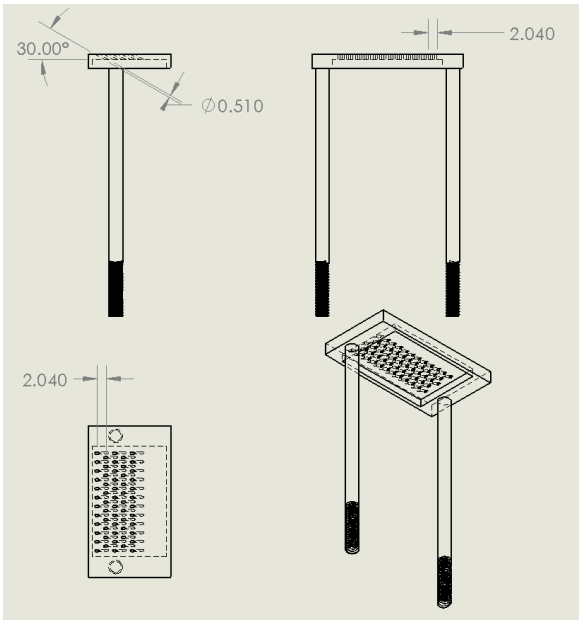

Figure E.4: Five Row Cylindrical Hole Cooling Configuration

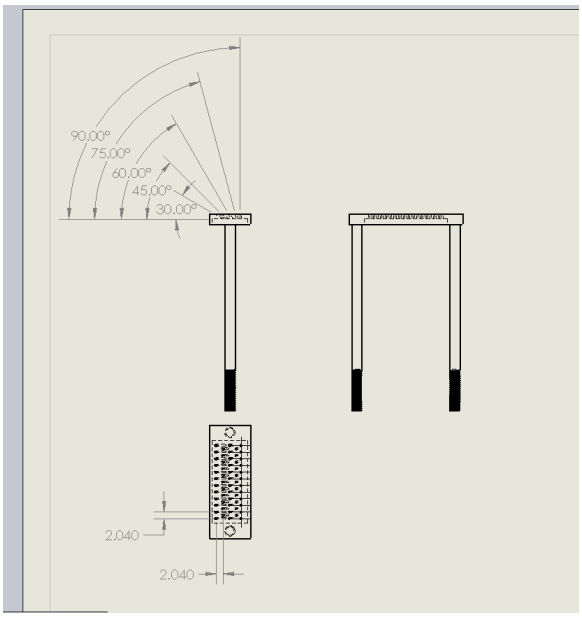

Figure E.5: Roll Forward Cooling Configuration

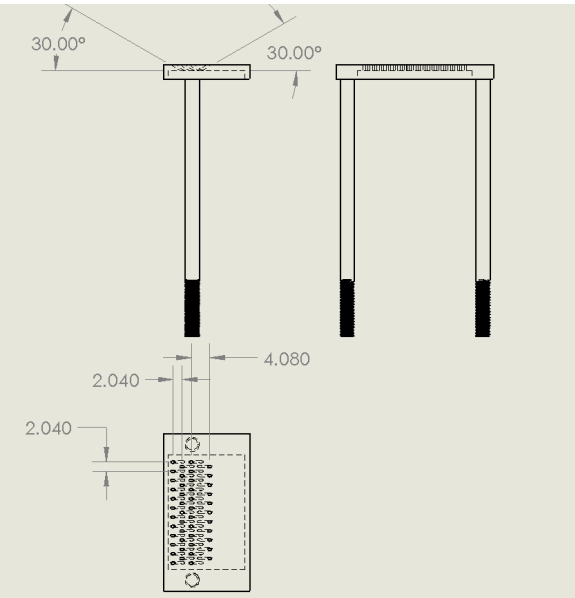

Figure E.6: One Row Upstream Cooling Configuration

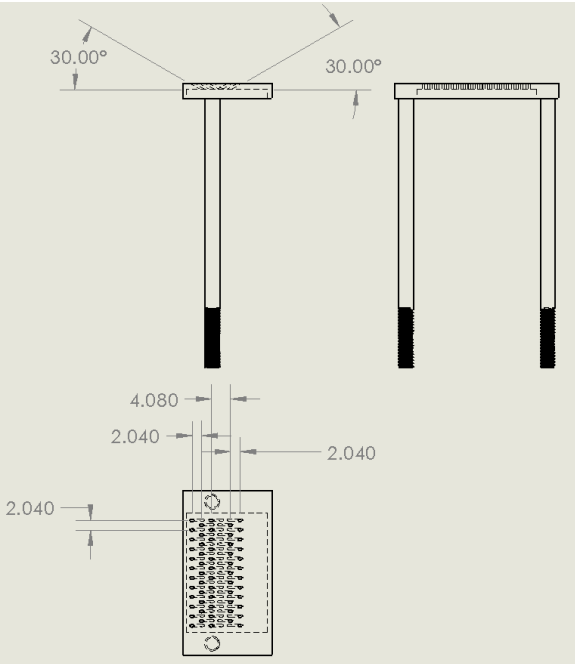

Figure E.7: Two Row Upstream Cooling Configuration

Appendix F: Test Matrices

Air Supply (SLPM)	M	ϕ	Coolant
212	0	1.175	-
212	0.5	1.175	Air
212	0.5	1.175	N_2
212	1.0	1.175	N_2
212	1.0	1.175	Air
212	2.0	1.175	Air
212	2.0	1.175	N_2
600	0.5	1.175	Air
600	0.5	1.175	N_2
600	1.0	1.175	N_2
600	1.0	1.175	Air
600	2.0	1.175	Air
600	2.0	1.175	N_2

Table F.1: Layer Buildup Campaign Test Matrix, Blowing Ratio Sweep

Air Supply (SLPM)	M	ϕ	Coolant
600	0	1.175	-
600	0.5	1.175	Air
600	0.5	1.175	N_2
600	1.0	1.175	N_2
600	1.0	1.175	Air
600	2.0	1.175	Air
600	2.0	1.175	N_2
600	3.0	1.175	N_2
600	3.0	1.175	Air
600	4.0	1.175	Air
600	4.0	1.175	N_2

Table F.2: Layer Buildup Campaign Test Matrix, Blowing Ratio Sweep

Air Supply (SLPM)	M	ϕ	Coolant
600	2.0	1.10	-
600	2.0	1.10	Air
600	2.0	1.10	N_2
600	2.0	1.175	-
600	2.0	1.175	N_2
600	2.0	1.175	Air
600	2.0	1.25	-
600	2.0	1.25	Air
600	2.0	1.25	N_2
600	2.0	1.35	-
600	2.0	1.35	N_2
600	2.0	1.35	Air
600	2.0	1.30	-
600	2.0	1.30	N_2
600	2.0	1.30	Air
600	2.0	1.40	-
600	2.0	1.40	N_2
600	2.0	1.40	Air

Table F.3: Layer Buildup Campaign Test Matrix, Phi Sweep

M	ϕ	Coolant	Oil Temp. (°F)
2.0	1.175	-	225
2.0	1.175	N_2	225
2.0	1.175	Air	225
2.0	1.175	-	250
2.0	1.175	N_2	250
2.0	1.175	Air	250
2.0	1.175	-	275
2.0	1.175	N_2	275
2.0	1.175	Air	275
2.0	1.175	-	300
2.0	1.175	N_2	300
2.0	1.175	Air	300
2.0	1.175	-	350
2.0	1.175	N_2	350
2.0	1.175	Air	350
2.0	1.175	-	400
2.0	1.175	N_2	400
2.0	1.175	Air	400

Table F.4: Wall Temperature Study Test Matrix

Bibliography

[1] *Hastelloy® X Alloy*.

[2] Anderson, W., M.D. Polanka, J. Zelina, D. Evans, S.D. Stouffer, and G.R. Justinger. "Effects of a Reacting Cross-Stream on Turbine Film Cooling". *Journal of Engineering for Gas Turbines and Power*, 132, May 2010.

[3] Bergman, T.L., A.S. Lavine, F.P. Incropera, and D.P. DeWitt. *Fundamentals of Heat and Mass Transfer*.

[4] Bogard, D.G. and K.A. Thole. "Gas Turbine Film Cooling".

[5] Bohan, B.T. *Analysis of Flow Migration in an Ultra Compact Combustor*. Master's thesis, Air Force Institute of Technology, March 2011.

[6] Bohan, B.T., D.L. Blunck, S. Kostka, N. Jiang, S. Roy, M.D. Polanka, and S.D. Stouffer. "Impact of and Upstream Film-Cooling Row on Mitigation of Secondary Combustion in a High Fuel-Air Environment". Number GT-2012-68310 in ASME Turbo Expo 2012. ASME, Copenhagen, Denmark, 2012.

[7] DeLallo, M.R. *Impact of Trench and Ramp Film Cooling Designs to Reduce Heat Release Effects in a Reacting Flow*. Unpublished, Air Force Institute of Technology, March 2012.

[8] DeLallo, M.R., M.D. Polanka, and D.L. Blunck. "Impact of Trench and Ramp Film Cooling Designs to Reduce Heat Release Effects in a Reacting Flow". ASME Turbo Expo 2012. ASME, Copenhagen, Denmark, 2012.

[9] Evans, D.S. *The Impact of Heat Release in Turbine Film Cooling*. Unpublished, Air Force Institute of Technology, 2008.

[10] Greiner, N.J., M.D. Polanka, J.R. Robertson, and J.L. Rutledge. "Effect of Variable Properties Within a Reacting Boundary Layer with Film Cooling". Number GT-2013-94794 in ASME Turbo Expo 2013. ASME, San Antonio, TX, 2013.

[11] Johnson, D.D. and M.D. Polanka. "Cooling Requirements for an Ultra-Compact Combustor". Number AIAA-2012-0948 in 50th AIAA Aerospace Sciences Meeting. AIAA, Nashville, TN.

[12] Kakade, V.U., S.J. Thorpe, and M. Gerendás. "Effusion-Cooling Performance at Gas Turbine Combustor Representative Flow Conditions". Number GT2012-68115 in ASME Turbo Expo. ASME, Copenhagen, Denmark, June 2012.

[13] Kirk, D.R., G.R. Guenette, S.P. Lukachko, and I.A. Waitz. "Gas Turbine Engine Durability Impacts of High Fuel-Air Ratio Combustors Part 2: Near Wall Reaction Effects on Film-Cooled Heat Transfer". Number GT-2002-30182 in ASME Turbo Expo 2002: Land, Sea & Air. ASME, Amsterdam, The Netherlands, 2002.

[14] Lakshminarayana, B. *Fluid Dynamics and Heat Transfer of Turbomachinery*. John Wiley, 1995.

[15] Lewis, G.D. "Centrifugal-Force Effects on Combustion".

[16] Lukachko, S.P., D.R. Kirk, and I.A. Waitz. "Turbine Durability Impacts of High Fuel-Air Ratio Combustors, Part 1: Potential For Intra-Turbine Oxidation of Partially-Reacted Fuel". Number GT-2002-30077 in ASME Turbo Expo 2002: Land, Sea & Air. ASME, Amsterdam, The Netherlands, 2002.

[17] Mellor, A.M., D.W. Bahr, W.S. Derr, K. Depooter, W.J. Dodds, H.E. Eickhoff, L. Gardner, D.C. Hammond, J.E. Peters, R.B. Whyte, and G. Winterfield. *Design of Modern Turbine Combustors*. Academic Press Inc., San Diego, CA, 1990.

[18] Milanes, D.W., D.R. Kirk, K.J. Fidkowski, and I.A. Waitz. "Gas Turbine Engine Durability Impacts of High Fuel-Air Ratio Combustors: Near Wall Reaction Effects on Film-Cooled Backwards-Facing Step Heat Transfer". Number GT2004-53259 in ASME Turbo Expo. ASME, Vienna, Austria, June 2004.

[19] Mongia, H.C. "Gas Turbine Combustor Liner Wall Temperature Calculation Methodology". 37th AIAA/ASME/SAE/ASEE Joint Propulsion Conference and Exhibit. AIAA and ASME and SAE and ASEE, Salt Lake City, Utah, July 2001.

[20] Mongia, H.C. "A Synopsis of Gas Turbine Combustor Design Methodology Evolution of Last 25 Years". ISABE, AIAA, Cincinnati, Ohio, 2001.

[21] Mongia, H.C. and D.J. Brandes. *Design Documentation Report: Counterflow Film-Cooled Combustor Program*. Technical report, NASA Lewis Research Center, June 1982.

[22] Nenniger, J.E., A. Kridiotis, J. Chomiak, J.P. Longwell, and A.F. Sarofim. "Characterization of a Toroidal Well Stirred Reactor". Twentieth Symposium (International) on Combustion, The Combustion Institute, 473–479. 1984.

[23] Oguntade, H.I., G.E. Andrews, A.D. Burns, D.B. Inham, and M. Pourkashanian. "Conjugate Heat Transfer Predictions of Effusion Cooling: The Influence of the Coolant Jet-flow Direction on the Cooling Effectiveness". Number GT2012-68517 in ASME Turbo Expo. ASME, Copenhagen, Denmark, June 2012.

[24] Popp, O., D.E. Smith, J.V. Bubb, H.C. Grabowski III, T.E. Diller, J.A. Schetz, and Wing-Fai Ng. "Steady and Unsteady Heat Transfer in a Transonic Film Cooled Turbine Cascade". *American Journal of where was this published*, 2200.

[25] Sirignano, W.A., J.P. Delplanque, and F. Liu. “Selected Challenges in Jet and Rocket Engine Combustion Research”.

[26] Turns, S.R. *An Introduction to Combustion*.

[27] Zelina, J., G.J. Sturgess, and D.T. Shouse. “The Behavior of an Ultra-Compact Combustor (UCC) Based on Centrifugally-Enhanced Turbulent Burning Rates”. *AIAA*, (2004-3541), 2004.

REPORT DOCUMENTATION PAGE

Form Approved
OMB No. 0704–0188

1. REPORT DATE *(DD–MM–YYYY)*	2. REPORT TYPE	3. DATES COVERED *(From — To)*
27–03–2013	Master's Thesis	Oct 2011–Mar 2013

4. TITLE AND SUBTITLE

Film Cooling in Fuel Rich Environments

5a. CONTRACT NUMBER

5b. GRANT NUMBER

5c. PROGRAM ELEMENT NUMBER

6. AUTHOR(S)

Robertson, Jacob J., Second Lieutenant, USAF

5d. PROJECT NUMBER

5e. TASK NUMBER

5f. WORK UNIT NUMBER

7. PERFORMING ORGANIZATION NAME(S) AND ADDRESS(ES)

Air Force Institute of Technology
Graduate School of Engineering and Management (AFIT/EN)
2950 Hobson Way
WPAFB, OH 45433-7765

8. PERFORMING ORGANIZATION REPORT NUMBER

AFIT-ENY-13-M-27

9. SPONSORING / MONITORING AGENCY NAME(S) AND ADDRESS(ES)

Dr. David Blunck
1790 Loop Road
Building 490
WPAFB,OH 45433

10. SPONSOR/MONITOR'S ACRONYM(S)

AFRL / RCTZ

11. SPONSOR/MONITOR'S REPORT NUMBER(S)

12. DISTRIBUTION / AVAILABILITY STATEMENT

DISTRIBUTION STATEMENT A:
APPROVED FOR PUBLIC RELEASE; DISTRIBUTION UNLIMITED

13. SUPPLEMENTARY NOTES

14. ABSTRACT

The ultra compact combustor is a high performance gas turbine design concept that portends reduced weight for future weapons platforms. A natural outcome of the design is the continual presence of fuel-rich air in the turbine component of the engine. Because modern cooling schemes for hot section turbine blades involve injecting cool, oxygen-rich air adjacent to the surface, the potential arises for reaction with the unconsumed radicals in the mainstream flow and augmented heat transfer to the blade. This outcome is contrary to the purpose of film cooling, and can lead to early life-cycle turbine failure. This study examined the effects of multiple cooling hole geometries on downstream heat transfer. It demonstrated schemes that allow reactions to take place at a standoff distance from the wall being cooled and provide effective downstream cooling. Additionally, the research characterized the time scales involved in the reactions through temperature measurements and imaging.

15. SUBJECT TERMS

Ultra Compact Combustor, Combustion, Film Cooling

16. SECURITY CLASSIFICATION OF:			17. LIMITATION OF ABSTRACT	18. NUMBER OF PAGES	19a. NAME OF RESPONSIBLE PERSON
a. REPORT	b. ABSTRACT	c. THIS PAGE			Dr. Marc D. Polanka (ENY)
U	U	U	UU	147	19b. TELEPHONE NUMBER *(include area code)* (937) 255-3636 ext. 4714